?

TEL AVIV UNIVERSITY אוניברסיטת תל-אביב

RAYMOND AND BEVERLY SACKLER
FACULTY OF EXACT SCIENCES
SCHOOL OF PHYSICS & ASTRONOMY

הפקולטה למדעים מדויקים
ע"ש ריימונד ובברלי סאקלר
בית הספר לפיסיקה ואסטרונומיה

Research Thesis for a Degree of "Doctor of Philosophy

Search for New Physics Beyond the Standard Model in Dijet Events at the LHC

Submitted to the Senate of Tel Aviv University by
Adi Ashkenazi

The research was carried out under the supervision of
Dr. **Gideon Bella** and Prof. **Erez Etzion.**

April 2017
adi.ashkenazi@cern.ch

To my mother, Hana Ashkenazi.

Contents

Abstract

Searches for new phenomena in LHC proton-proton collisions with the ATLAS detector, using events with at least two high transverse momentum jets were preformed measuring the invariant mass and the angular distribution of the two leading jets. All results are consistent with the predictions of the Standard Model. The angular analysis was performed at a centre-of-mass energy of $\sqrt{s} = 8$ TeV using an integrated luminosity of 17.3 fb^{-1}. In a benchmark model of quark contact interactions, a compositeness scale below 8.1 TeV in a destructive interference scenario and 12.0 TeV in a constructive interference scenario was excluded at 95% confidence level. A mass resonance search was done for the first time at ATLAS using a trigger level analysis at a center-of-mass energy of $\sqrt{s} = 13$ TeV with an integrated luminosity of 3.4 fb^{-1}. No resonance was found and limits were set on generic Gaussian resonances and on a simplified model of a leptophobic axial-vector boson mediator to a dark sector, Z'. In addition, this thesis summarises a theoretical-experimental effort to advocate the use of simplified dark matter models as benchmark models for analyses searching for new physics and the performance of quality tests for the TGC detectors towards their use as part of ATLAS experiment.

Acknowledgement

First and foremost I would like to express my gratitude to both my supervisors, Dr. Gideon Bella, and Prof. Erez Etzion. Thank you for the guidance and patience, for all the insights, advice, support and the set of tools which I'm sure is going to serve me in the future.
To my off-shore adviser, whom I'm also very proud to call my friend: Dr. Caterina Doglioni and the entire dijet working group for great cooperation.
A special thank you is sent to Prof. Eilam Gross, and Dr. Ohad Silbert for giving me my first opportunity in the field of particle physics.
Thank you to my colleagues at the high energy lab, the legendary ztrif: Meni Ben Moshe, Yan Benhammou, Guy Koren, Merlin Davies, Nimrod Taiblum, Rotem Gorodetzky, Hadar Cohen, Ibtisam Jikhleb, Itamar Levy. To the management staff of the School of physics and astronomy in Tel Aviv University and especially Mrs. Yakira Navaty and Mrs. Galia Netzer-Erlichman.
To the wolf, Oren Slone, and the Italian crew, to Shenkar 308, to Elya and her entourage, and to my great friends especially Tal, Tooly, Efrat, Adi, Moran.
This work is dedicated to my mother, Hana, who has managed to redefine motherhood in the past few years, and does not seem to stop her unconditionally love, giving, and encouragement. You, your life and accomplishments are inspiring my way. Also, thank you for my two brothers, Eyal, and Shay and their loving families.

Chapter 1

Introduction

Since its first operation on 2010, the Large Hadron Collider (LHC) [1], located at CERN, on the border between Switzerland and France, has been pushing the frontiers of experimental high energy physics. It is the highest energy particle collider ever constructed and it is expected to further increase its centre of mass energy in the future. The LHC is widely accepted as the largest and most complex experiment in the world, including the largest computing grid ever used for saving and analysing data from its various detectors. ATLAS is the largest detector ever built at CERN, and in July 2012, along with the CMS collaboration, the ATLAS collaboration published the discovery of a particle which is consistent with the Standard Model (SM) Higgs boson [2,3], and by that completed a line of historic discoveries of all particles in this model. There is great hope that the ATLAS detector will continue to shed light on New Physics (NP) beyond the SM and supply further major discoveries in the future.

The work summarised in this thesis was all done as part of the ATLAS experiment. Working as part of such great experiment, one has many opportunities to touch a variety of research topics. In addition to the main research topic of this work which is a search for NP in dijet events, I have taken part in a joint task force consisting of experimentalists from ATLAS and theoreticians, advocating the use of simplified dark matter models instead of effective field theories as benchmark models for analyses searching for NP such as the various dijet analyses. This work was published in [4,5]. Following the introduction with a brief description of the SM to follow, chapter 2 will summarise the part of this effort I have participated in. Chapter 3 describes the experimental environment of the accelerator and detector used in the analysis. The major part of this work is summarised in chapter 4 and describes a search for new phenomena in mass and angular distribution of jet pairs (dijets) produced in the LHC proton proton (pp) collisions, using data collected with the ATLAS detector. This work was all published in a series of articles and conference notes [6–10].

Particularly the mass resonance search [9] was performed for the first time in ATLAS using a Trigger Level Analysis (TLA). Since no new evidence for NP were found, the dijet signature was used to constrain several NP models including one simplified model. Another joint effort of Tel Aviv University (TAU) and the Technion was to preform quality tests of the Thin Gap Chamber (TGC) detectors constructed at the Weizmann Institute (WIS), toward their use as part of the ATLAS muon trigger system. I have had the opportunity to be part of the quality test team and to design the offline analysis environment for the tests, and this will be the topic of the last part of this work, chapter 5.

The author's contribution

Experimental Collaborations in particle physics rely on the work of many individual researchers and technicians. Especially in the ATLAS collaboration, which is known to be the largest of them all, there are more than 3,000 physicists, and their contributions are invaluable for each and every publication. Therefore, the authors list of any ATLAS public document includes all members of the collaboration, in alphabetical order. In order to become an ATLAS member, one should participate in the detector operational shifts onsite, and complete a qualification task, which is a dedicated work done for the collaboration's greater good. My qualification task was to perform the quality tests for the TGC detectors which are described in chapter 5. For this purpose I have designed and built the offline testing environment, and operated it along with the lab technicians, whom were given a simple tool which can be also used for future measurements and tests.

All publications mentioned in this thesis are those to which I have contributed in the following ways: For the 8 TeV dijet mass resonance search [6] I have calculated the trigger efficiency as described in section 4.1.3. I was the co-author of the 8 TeV dijet angular analysis [8], and specifically I have set the tune for the chosen MC used, applied correction to its background prediction, simulated the signal used for the limit setting, and applied its corrections, calculated various systematics uncertainties and the overall uncertainties and was a part of the team producing the final results. I was also the co-author for the first TLA analysis to be conducted in ATLAS [9], which I have helped designing, from providing a proof of concept for its first approval, through performing sensitivity studies, choosing the best trigger to be used, deciding on the data format to be saved on disk considering the analysis needs and ATLAS computational limitations and more. Then I was in charge for the jet cleaning and jet calibration procedures. I was writing the chapter on trigger jet calibration in the ATLAS internal note about the readiness of trigger jets for run II, and I have provided most of the above services also to the 13 TeV mass resonance and angular analysis paper [10].

Finally in the theoretical-experimental joint effort to promote the use of simplified models in the interpretation of experimental results [4,5], I co-authored the section regarding simplified models in an s-channel detailed in 2.1, and was in charge of the singal and background simulation for the calculation of the expected sensitivity of an LHC run at 14 TeV for DM searches.

1.1 The standard model

The Standard Model [11,12] is a theory which attempts to describe the fundamental particles and the interactions between them - ElectroMagnetic (EM), weak and strong interaction. Gravitation is too weak to be included in this framework. The SM states that the elementary particles can be divided into two main groups: fermions, particles with half integer spin, which are the constituents of matter, and bosons, with integer values of spin, which are the carriers of interactions. Fermions are divided into leptons, which are interacting only via EM and weak interactions, and quarks, interacting via all SM interactions (EM, weak and strong). Bosons with spin 1, the gauge bosons, are the force carrier. Photons, for example, are the carriers of the EM interaction, though they have no EM charge. The three carriers of the weak force are the $W^{\pm}$ and the Z bosons. The 8 gluons are the carriers of the strong force and have a strong charge (color). The Higgs, has a zero spin, and is the one who 'gives' all the elementary particles their masses. Figure 1.1 shows the elementary particles and their properties: mass, EM charge, and spin.

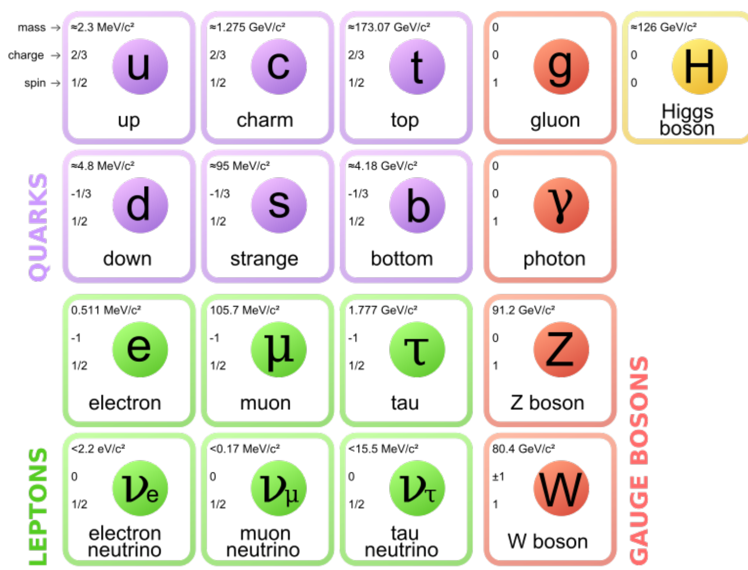

Figure 1.1: Elementary particles in the Standard Model

The electroweak interaction

The electroweak interaction [13] is a unification of the EM and the weak forces. The EM interaction couples to all fermions with their electric charge, q. The weak interaction couples to quarks and leptons, including the electric neutral neutrinos. The weak force carrier can be charged ($W^{\pm}$) or neutral (Z), and the weak interaction mediated by a charged boson can change flavours, for example: a u into a d or a μ into a ν_{μ}. The weak interaction is the only interaction which violates the parity and charge conjugation symmetries.

The unification of the weak and the EM interactions is represented by the $SU(2)_L \times U(1)$ gauge symmetry group. The $SU(2)_L$ interaction is between one of the three W^i bosons, a weak isospin triplet of gauge vector fields, and the weak current J^i involving the left-handed fermions, with a coupling strength g, and the corresponding interaction term $-ig(J^i)^{\mu}W^i_{\mu}$. As $U(1)_{\mathrm{EM}}$ does not have a well defined transformation under $SU(2)_L$, the enlarged group uses a different $U(1)$ group, with the associated charge Y, so called hypercharge, defined by $q = I^3 + \frac{Y}{2}$, where I^3 is the third component of the isospin, yielding the same Y value for all the members of the same isospin multiplet. The corresponding gauge boson B is a neutral vector field, interacting with the hypercharge current, $(J^Y)^{\mu}$ with a coupling strength $g'/2$, and the interaction term $-ig'/2(J^Y)^{\mu}B_{\mu}$

The $SU(2)_L \times U(1)$ symmetry is spontaneously broken by the Higgs mechanism. Consequently, the neutral fields W^3_{μ} and B_{μ} mix into,

$$A_{\mu} = B_{\mu}\cos\theta_W + W^3_{\mu}\sin\theta_W \tag{1.1}$$

$$Z_{\mu} = -B_{\mu}\sin\theta_W + W^3_{\mu}\cos\theta_W, \tag{1.2}$$

where A_{μ} is a massless gauge boson, the photon, interacting with the EM current, and Z_{μ} is a massive gauge boson, interacting with the weak neutral current. The Weinberg mixing angle, θ_W is related to the coupling ratio, $\tan\theta_W = g'/g$. In addition, the weak charged interaction is described as the exchange of: $W^{\pm}_{\mu} = \sqrt{\frac{1}{2}}(W^1_{\mu} \pm W^2_{\mu})$.

The strong interaction

The strong interaction, described by Quantum Chromo Dynamics (QCD), couples to quarks and gluons (partons). The gluons are the gauge bosons carrying the strong interaction, and also carrying the strong charge, known as color [14]. QCD is based on a SU(3) non abelian gauge group. Perturbative calculations of the cross sections of QCD processes can diverge due to ultraviolet gluon emissions, thus in order to get a finite result, a renormalisation procedure has to be applied, introducing a renormalisation scale, μ_{R} into the calculations, which is not well defined but must be around the typical momentum transfer in the interaction. Fortunately, the dependence of the calculated result on this renormalization scale is weak and becomes even weaker with increasing order of the perturbative calculation. . The strength of the interaction depends on the distance between the interacting particles (or on the transfered momentum between them). This property is called the asymptotic freedom, and is described by a running coupling constant, α_s, which decreases with decreasing distance or increasing transferred momentum Q,

$$\alpha_s(Q^2) = \frac{12\pi}{(33 - 2n_{\mathrm{f}})\ln(\frac{Q^2}{\Lambda^2_{\mathrm{QCD}}})}. \tag{1.3}$$

where n_{f} is the number of flavours, Q is the transferred momentum and Λ_{QCD} is the QCD scale, of the order of 100 MeV. In case two colored particles separate, and the energy increases above a threshold, a quark antiquark pair can be created. This is the reason that it is impossible to observe an isolated colored particle, and thus only colorless hadrons can be observed and collide in hadronic colliders.

1.2 Hadron collisions

Ever since the famous Rutherford experiment bombarding a thin gold foil with alpha particles to refute the known atom model, the field of experimental particle physics grew from one colliding experiment to the other, and kept accelerating various particle to higher and higher energies in order to collide them with a fixed target or with one another. According to the parton model [14], a hadron (such as the proton) consists of three valance quarks (uud), giving it its electric charge, and a sea of gluons and pairs of quarks and antiquarks. The total momentum of the hadron is distributed between all of its constituents quarks and gluons according to the Parton Distribution Function (PDF). The PDF is also dependent on the long distance effects on the hadron, parametrised by a factorisation scale, μ_{F}. When hadrons collide, their constituents, the quarks or the gluons are interacting one with the other. In case the two interacting partons own a large fraction of the hadrons momenta, the transferred momentum is large enough resulting a small $\alpha_s(Q^2)$ allowing the QCD perturbative calculations to describe it properly.

1.2.1 Coordinate system

In a circular particle accelerator, the conventional coordinate system is a right handed reference system with the interaction point as its origin, and the beam line as the z axis. The x axis points towards the centre of the accelerator ring, and the y axis upwards. It is possible to describe a point is space using (r, ϕ, z) set of coordinates.

$$r = \sqrt{x^2 + y^2} \qquad ; \quad \phi = \arctan(y/x) \tag{1.4}$$

More often the psaudorapidity η is being used instead of the polar angle θ:

$$\theta = \arccos(\frac{z}{\sqrt{r^2 + z^2}}) \quad ; \quad \eta = -\ln(\tan(\theta/2)) \tag{1.5}$$

For relativistic particles the psaudorapidity is a good approximation for the rapidity of the particle

$$y = \frac{1}{2}\ln(\frac{E + p_z}{E - p_z}) \tag{1.6}$$

This variable is invariant up to a constant to a boost in the z direction. Another variable is ΔR which is used to estimate the angular separation between two objects: $\Delta R = \sqrt{\Delta\phi^2 + \Delta\eta^2}$. A track is defined by p_{T}, the transverse momentum, which is the projection of the momentum vector on the xy plane, η, ϕ and d_0, z_0, where d_0 is the distance between the track and the interaction vertex at the point of closest approach in the x-y plane, and z_0 is the z-coordinate of the track at that point.

Chapter 2

Simplified Models for Dark Matter

The SM, though confirmed by many experiments and though its parameters were measured to a high degree of accuracy, is known to be incomplete. The model might describe well all the known matter, but this matter occupies roughly four percent of the universe, with the other parts being Dark Matter (DM), and dark energy. The available evidences for the existence of dark matter [11] include measurements of the rotational curves of galaxies, galaxies colliding and gravitational lensing, all leading to the assumption about existence of masses which are not observed astronomically. In addition, analysing the angular power spectrum of the Cosmic Microwave Background (CMB) gives us insight on the different components of the universe and the ratio between them. These evidences imply that the DM is only weakly interacting, at least gravitationally with known matter, it does not carry electric charge, it was cold (non-relativistic) during the early period of the universe and it is long lived. The SM does not include particles with these properties, a good description in the language of particle physics for a DM candidate is the Weakly Interacting Massive Particle (WIMP), which is available in many models beyond the SM such as Super Symmetry (SUSY).

There are three common methods for searching for DM [15]: direct detection, indirect detection and collider production. The direct detection aims to search for the products of interactions between DM scattering off an atomic nuclei. The indirect detections aims to search for the products of annihilation of WIMPs. We shall focus on the collider production of WIMPs, which is possible in case the WIMP is lighter than $\sqrt{s}$ of the collider, and as in all detection methods, in case the WIMP is interacting with the SM particles. Unlike most of the SM particles, the WIMPs are expected to pass the detectors without leaving a signature due to their weakly interacting behaviour with matter leading to Missing transverse Energy (MET) signature. At the LHC, with proton-proton collision, an event can end up with either DM particles only, leading to no observed object, or a final state of DM and SM particles, leading to SM signatures and large MET. The observed signatures thus can set limits on the parameters of DM models, such as the WIMP mass.

The most common search for MET focuses on events with a single jet (mono-jet) and MET, where the event is assumed to be of the form of two interacting SM particles (protons, in the case of the LHC) leading to undetected final state and a jet, assumed to originate from Initial State Radiation (ISR). Also common are searches for multi jets recoiling against large MET, as in high energy collision there can be several ISR jets.

The DM interactions can be expressed using an Effective Field Theory (EFT) or via a simplified model, specifying a mediator particle being able to interact with both SM and DM particles. For years it was common to use the EFT to interpret DM searched. In the EFT approach, the heavy mediators are integrated out, leaving only the initial SM and final DM particles. This approach allows a model independent description of the data, but has shortcomings which will be described in the following. The EFT approach uses non re-normalisable operators that couple quarks or leptons to the WIMP, as described in the following interaction term of the lagrangian:

$$\mathcal{L}_{\rm EFT} = \frac{1}{\Lambda^2}(\bar{q}q)(\bar{\chi}\chi) \tag{2.1}$$

where χ is the a fermionic field representing the WIMP. This product of four fermion fields is a six-dimensional operator and thus, the Λ^2 term in the denominator is needed, where Λ is a mass scale. A list of all possible 4-fermion operator is available in Table 1 in [16].

To better illustrate this point, let us give a simple example, and consider a model with a heavy mediator connecting two DM particles to two quarks. The mediator has mass $M_{\rm med}$, the DM particle mass is m_χ and couplings to quarks and DM $g_{\rm q}$ and g_χ, respectively. At low energies, much smaller than $M_{\rm med}$, the heavy mediator can be integrated out from the theory and one is left with the EFT theory without the mediator, where the interactions between DM and quarks are described by a tower of effective operators. The parameters of the ultra-violet (UV) theory including the mediator are connected to the scale Λ associated with the dimentions-6 operators of the low-energy EFT through

$$\Lambda = \frac{M_{\rm med}}{\sqrt{g_{\rm q} g_\chi}} \tag{2.2}$$

The EFT is valid as long as the events producing DM are such that the mediator cannot be directly produced. Therefore, they must occur with a momentum transfer $Q_{\rm tr}$ such that

$$Q_{\rm tr}^2 < M_{\rm med}^2 \tag{2.3}$$

The expansion in terms of a tower of higher-dimensional effective operators can be viewed as the expansion of the propagator of the mediator particle,

$$\frac{1}{Q_{\rm tr}^2 - M_{\rm med}^2} = -\frac{1}{M_{\rm med}^2}(1 + \frac{Q_{\rm tr}^2}{M_{\rm med}^2} + \mathcal{O}(\frac{Q_{\rm tr}^4}{M_{\rm med}^4})) \tag{2.4}$$

Retaining only the leading term $1/M_{\rm med}^2$ corresponds to truncating the expansion to the lowest dimensional operator. This truncation is a good approximation only if

$$Q_{\rm tr}^2 \ll M_{\rm med}^2 \tag{2.5}$$

which satisfies along with the definition of Λ:

$$Q_{\rm tr}^2 \ll g_{\rm q} g_\chi \Lambda^2 \sim \Lambda^2 \tag{2.6}$$

when the couplings $g_{\rm q}, g_\chi$ are at the natural scale of order 1. Therefore, one can characterise the deficiency of the truncation of the full operator tower to the leading term by evaluating the expansion parameter $Q_{\rm tr}/M_{\rm med}$. If one further assumes s-channel mediator exchange, then the kinematics of the process imposes $Q_{\rm tr} > 2m_\chi$ so the conditions (2.2) and (2.3) imply

$$\Lambda > \frac{Q_{\rm tr}}{\sqrt{g_{\rm q} g_\chi}} > 2\frac{m_\chi}{\sqrt{g_{\rm q} g_\chi}} \tag{2.7}$$

which, in the extreme case in which the perturbativity condition on the couplings $g_{\rm q} g_\chi < 4\pi$ is assumed, leads to

$$\Lambda > \frac{m_\chi}{2\pi} \tag{2.8}$$

Addressing quantitatively the question of the validity of the EFT suffers from a dependence on the (unknown) couplings of the UV theory, as shown by the conditions (2.6) and (2.7).

With this caveat in mind, it is nonetheless possible to quantify the error introduced by using effective operators when describing processes at very high $Q_{\rm tr}$. For example, for a given process, one can calculate the fraction of events that pass the condition (2.6). We define this as

$$R_\Lambda^{\rm tot} \equiv \frac{\sigma|_{Q_{\rm tr}<\Lambda}}{\sigma}, \tag{2.9}$$

where σ is the cross section for the process of interest, and $\sigma|_{Q_{\rm tr}<\Lambda}$ is the same cross section truncated such that all events pass the condition $Q_{\rm tr} < \Lambda$. As an example, contours in $R_\Lambda^{\rm tot}$ are shown in figure 2.1 reproduced from reference [17], for the process $q\bar{q} \to \chi\chi + g$ at center of mass energy $\sqrt{s} = 14$ TeV, assuming couplings of order unity. The plots correspond to the D1 ($\bar{q}q\bar{\chi}\chi$) and D5 ($\bar{q}\gamma^\mu q\bar{\chi}\gamma_\mu\chi$) operators in the notation of ref. [16]. The results are qualitatively similar between the different operators and clearly indicate that LHC searches for DM are operating well within the region where the EFT approximation breaks down.

The EFT approach will not suffice in case heavy mediators will directly appear in s-channel processes at the LHC with its design energy. An effort was conducted in the ATLAS experiment with the cooperation of many theorists in the field to start interpreting the same results using simplified models specifying the exact process leading to DM signature. This effort is documented in [4]. My contribution was related to the Simplified Models for $(\bar{q}\Gamma^m q)$ $(\bar{\chi}\Gamma'_m\chi)$ type operators - s-channel model. Simplified models [18, 19] specify the mediators between the SM and DM particles and account for their possible production.

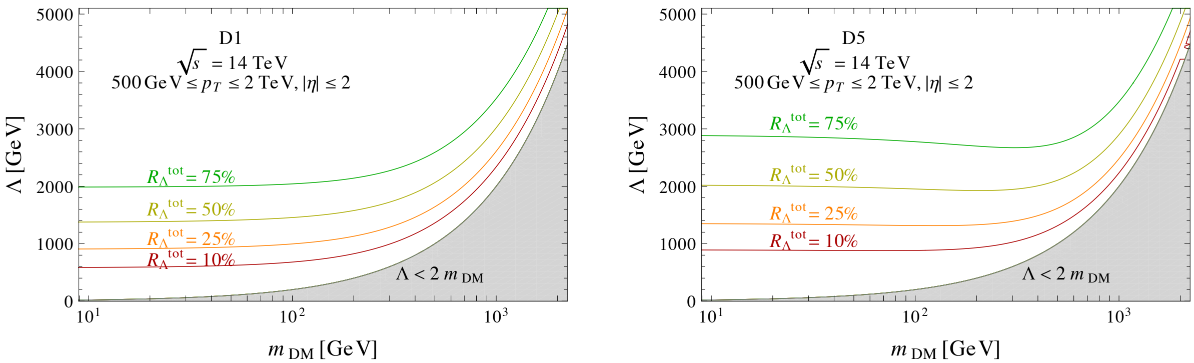

Figure 2.1: Contours of the parameter $R_\Lambda^{\rm tot}$ for the D1 (left) and D5 (right) operators and the process $q\bar{q} \to \chi\chi + g$ at center of mass energy $\sqrt{s} = 14$ TeV. Cuts are chosen to be comparable to those used by the ATLAS and CMS collaborations.

2.1 Simplified models for $(\bar{q}\Gamma^m q)(\bar{\chi}\Gamma'_m\chi)$ type operators in an s-channel model

Modeling the DM particle, χ, as a fermion, we consider the dimension six operators of the form,

$$\mathcal{O}_6 = (\bar{q}\Gamma^m q) \ \ (\bar{\chi}\Gamma'_m\chi) \ . \tag{2.10}$$

These operators are the $D1 - D10$ (and $D1' - D4'$) operators in the notation of Ref. [17]. The simplest way of resolving 4-fermion operators of the form (2.10) is through a color-singlet boson, either a scalar or a vector, as shown in Fig. 2.2. The simplified model we describe contains as a mediator particle a new scalar (pseudo scalar), S (S'), or a new vector (axial vector), V_μ (V'_μ), with interactions,

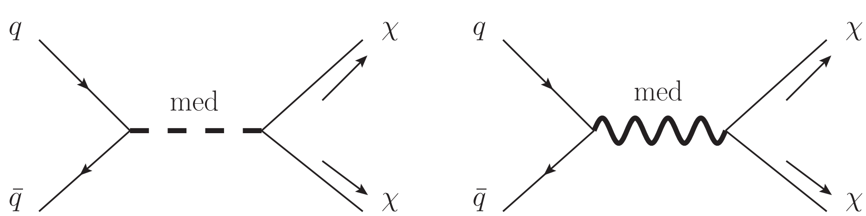

Figure 2.2: Two possible mediators. A massive scalar and/or a massive vector-boson, resolving dimension-6 operators of the form (2.10) through an s-channel exchange.

$$\mathcal{L}_{\rm S} \ \supset \ -\frac{1}{2}M_{\rm med}^2 S^2 - y_\chi S\bar{\chi}\chi - y_q^{ij} S\bar{q}_i q_j + {\rm h.c.}\,,$$

$$\mathcal{L}_{S'} \supset -\frac{1}{2}M_{\rm med}^2 S'^2 - y'_\chi S'\bar{\chi}\gamma_5\chi - y'^{ij}_q S'\bar{q}_i\gamma_5 q_j + \text{h.c.}\,,$$
$$\mathcal{L}_{V} \supset \frac{1}{2}M_{\rm med}^2 V_\mu V^\mu - g_\chi V_\mu\bar{\chi}\gamma^\mu\chi - g^{ij}_q V_\mu\bar{q}_i\gamma^\mu q_j\,,$$
$$\mathcal{L}_{V'} \supset \frac{1}{2}M_{\rm med}^2 V'_\mu V'^\mu - g'_\chi V'_\mu\bar{\chi}\gamma^\mu\gamma_5\chi - g'^{ij}_q V'_\mu\bar{q}_i\gamma^\mu\gamma_5 q_j\,. \tag{2.11}$$

where $q = u, d$ and $i, j = 1, 2, 3$ are flavor indices. These Lagrangian terms generate the effective operators $D1', D4', D5$ and $D8$. Refs. [17, 20] find that the operators $D2', D3'$ and $D6, D7$ have the same partonic level cross section as $D4', D1'$ and $D8, D5$, respectively. Thus we do not include the former in what follows. Note that a UV complete description of scalar theory would require $y_q \simeq m_q/M_{\rm med}$ (resulting in the operators $D1 - D4$), but since the translation between these cases is simple, we find the use of Eqs. (2.11) sufficient for our purposes.

As concerns the mediator couplings to quarks, the existence of off-diagonal coupling is tightly constrained by various limits on Flavour Changing Neutral Current (FCNC) processes [21]. We do not study such couplings, thus taking only $g^{ij}_q = g^i_q\delta^{ij}$. In the following we consider the scenario of flavour blind couplings to all quarks: $g^i_d = g^i_u \equiv g_q$ for $i = 1, 2, 3$. We further assume that the only available decay channels are into quarks and DM particles.

The differential interaction partonic cross sections (with respect to η and $p_{\rm T}$ of the final jet originating from ISR) for the s-channel process $f(p_1) + \bar{f}(p_2) \to \chi(p_3) + \chi(p_4) + g(k)$ are given in Eqs. (2.4)-(2.8) of [17], where

$$\Lambda^4 = \frac{\left(Q_{\rm tr}^2 - M_{\rm med}^2\right)^2 + \Gamma^2 M_{\rm med}^2}{g_q^2 g_\chi^2}\,, \tag{2.12}$$

should be used to resolve the EFT operators, where Γ is the total width of the mediator.

As discussed earlier, the EFT approach, in which the integration out of a heavy mediator generates a tower of higher dimensional operators, is appropriate in processes with low energy transfer:

$$M_{\rm med} \gtrsim Q_{\rm tr} \geq 2m_\chi\,, \tag{2.13}$$

Refs. [17, 20] discuss the limitations of the EFT approach for DM searches for an s-channel mediator exchange, and quantify the dependence of the errors resulting from the EFT approach on mediator and DM masses and couplings. At the partonic level the ratio between the cross sections of the effective theory and the full theory is,

$$\left(\frac{{\rm d}^2\hat{\sigma}}{{\rm d}\eta{\rm d}p_{\rm T}}\right)_{\rm full} \Big/ \left(\frac{{\rm d}^2\hat{\sigma}}{{\rm d}\eta{\rm d}p_{\rm T}}\right)_{\rm EFT} = \frac{M_{\rm med}^4}{\left(Q_{\rm tr}^2 - M_{\rm med}^2\right)^2 + \Gamma^2 M_{\rm med}^2}\,, \tag{2.14}$$

where $\Lambda = M_{\rm med}/\sqrt{g_q g_\chi}$ was used.

The authors of Ref. [17] study the ratio between the EFT resulting cross section and the full theory at 8 TeV center of mass energy. They find that this ratio is smaller than 50% for both scalar and vector interactions if $\Lambda \gtrsim 2-3$ TeV and $m_\chi \lesssim 1$ TeV. In the following we explore the validity of the EFT approach as a function of the final jet p_T at $\sqrt{s} = 14$ TeV. For this high energy, the gluon initiated process is significant and contributes comparably to the quark initiated process, for high p_T jets. We therefore present numerical results based on Monte Carlo simulated events. The events are generated using `MadGraph` 5 [22] imposing a cut of $p_T \geq 200$ GeV and $|\eta| \leq 2.5$ on the final jet originating from ISR. To quantify the differences between the EFT and the simplified model approaches we use the ratio of partonic level cross-sections with a final state single jet in addition to the DM pair. We expect next-to-leading order corrections, showering, hadronization, and detector effects to largely cancel in the ratio, and leave a more detailed analysis to future study.

Fig. 2.3 (2.4) shows the ratio between the interaction cross sections resulting from the simplified model and the effective theory for the scalar (vector) mediated interactions. We present this ratio, first, for the differential cross section (with respect to the jet p_{T}), taking several choices of DM and mediator masses. We then show the ratio between the total cross section as a function of the DM and mediator masses. It can be seen that the two approaches coincide for $M_{\mathrm{med}} \gg 2m_\chi, p_{\mathrm{T}}$. However, if this condition is not fulfilled, differences between the full theory and the EFT approach appear both in the total cross section and in the kinematical distribution of the two. It is thus necessary to look at a wider range of the parameter space.

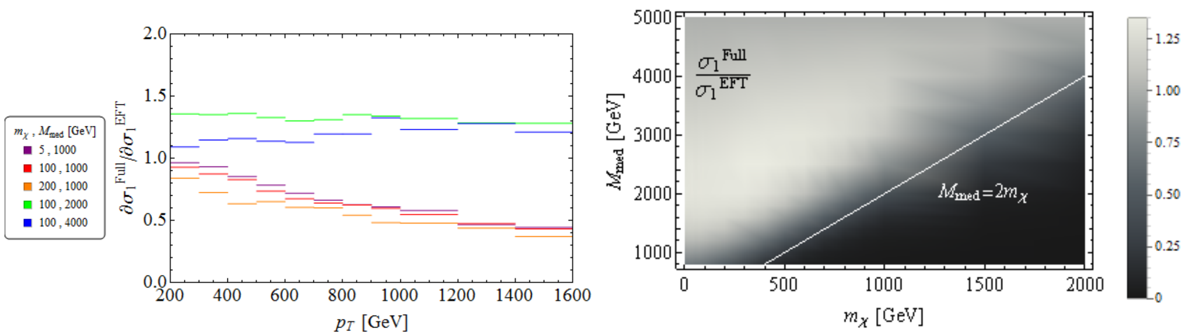

(a) (b)

Figure 2.3: The ratio between the interaction cross section of the full theory and the EFT one in the case of scalar mediator. The left figure shows the differential cross section, integrated over the jet rapidity $-2.5 \leq \eta \leq 2.5$ and the total cross section integrated over the jet transverse momentum $p_{\mathrm{T}} \geq 200$ GeV is plotted in the right figure. The events are generated using `MadGraph` 5.

To find the most convenient and enlightening set of simplified models, one needs to study the sensitivity of the observables to the helicity structure of the mediator couplings. To explore the impact of the different helicity structures we study the ratio between the cross

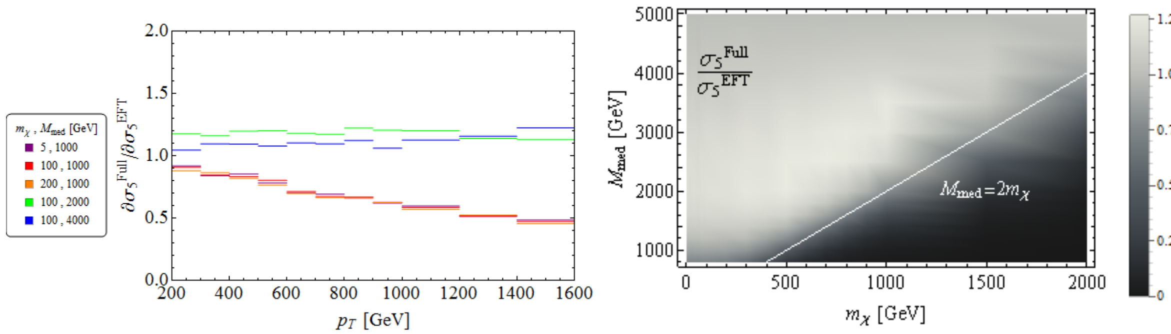

(a) (b)

Figure 2.4: Same as Fig 2.3 but for a vector mediator.

sections arising from scalar (vector) and pseudo scalar (axial vector) mediators. For the scalar and pseudo scalar interactions, Refs. [17, 20] find, at the parton level,

$$\left(\frac{\mathrm{d}^2\hat{\sigma}}{\mathrm{d}\eta \mathrm{d}p_\mathrm{T}}\right)_{D_1'} / \left(\frac{\mathrm{d}^2\hat{\sigma}}{\mathrm{d}\eta \mathrm{d}p_\mathrm{T}}\right)_{D_4'} = \left(1 - \frac{4m_\mathrm{DM}^2}{Q_\mathrm{tr}^2}\right) , \tag{2.15}$$

while in the vector section couplings

$$\left(\frac{\mathrm{d}^2\hat{\sigma}}{\mathrm{d}\eta \mathrm{d}p_\mathrm{T}}\right)_{D_5} / \left(\frac{\mathrm{d}^2\hat{\sigma}}{\mathrm{d}\eta \mathrm{d}p_\mathrm{T}}\right)_{D_8} = \left(\frac{Q_\mathrm{tr}^2 + 2m_\mathrm{DM}^2}{Q_\mathrm{tr}^2 - 4m_\mathrm{DM}^2}\right) . \tag{2.16}$$

In the limit of $Q_\mathrm{tr} \gg 2m_\chi$, the two differential cross sections share the same η and p_T distribution. However, these kinematical regions are highly suppressed by the Parton Distribution Functions (PDFs).

These ratios, based on events generated using `MadGraph` 5, are shown in Figs. 2.5 and 2.6 for the scalar and vector cases, respectively. As above, we present this ratio for the differential cross section first as a function of the jet p_T and as a function of the DM and mediator masses. As expected, we find that the ratios between each pair of cross sections (i.e. scalar vs. pseudo scalar, and vector vs. axial vector) have only small dependance on the final jet p_T. The processes do however have different total cross sections and thus will result in different number of signal events. Furthermore, this ratio has a nontrivial dependance on M_med for heavy DM particles, as a result of the PDFs. Since the scalar and axial vector interactions result in smaller cross-sections it is sufficient, as a first step, to explore the scalar and axial vector mediation resolving the s-channel DM pair-production at the LHC. If a signal is discovered, further analysis of the jet angular distribution could differentiate between the different particles mediating the DM production.

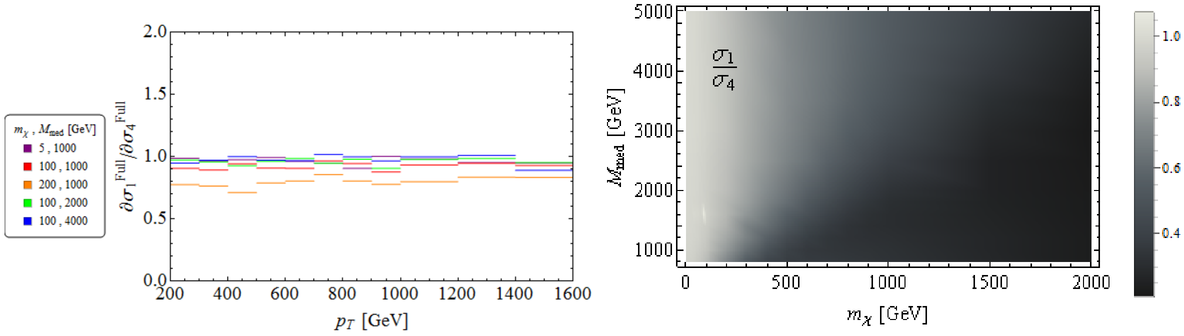

(a) (b)

Figure 2.5: The ratio between the s channel interaction cross section mediated by a scalar and a pseudoscalar mediator. The left figure shows the differential cross section, integrated over the jet rapidity $-2.5 \leq \eta \leq 2.5$ and the total cross section integrated over the jet transverse momentum $p_T \geq 100$ GeV is plotted in the right figure.

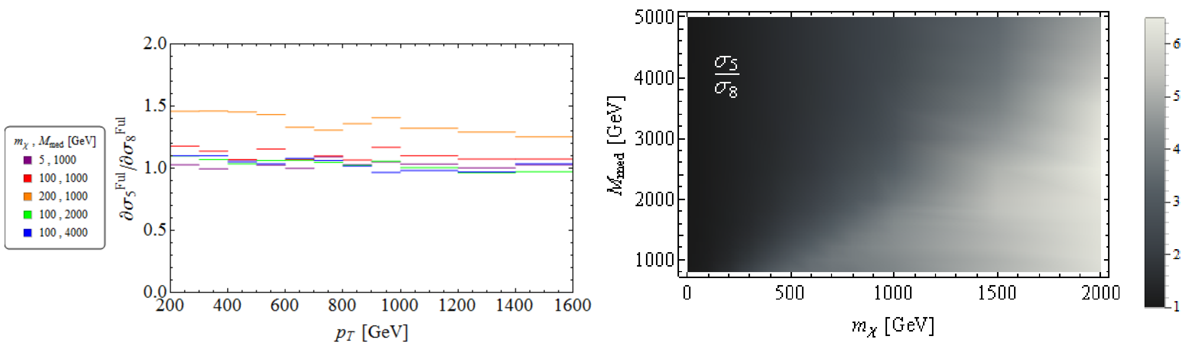

Figure 2.6: Same as Fig 2.5 but for a vector and an axial vector interactions.

2.1.1 Current constraints

Simplified models with s-channel mediator might also leave significant footprints in various experimental searches other than DM production at colliders. These are, for example, direct DM detection experiments and dijet production at the LHC. While it is important to consider these additional searches, this should be done with care since the reinterpretation of a set of constraints is model dependent. For instance, direct detection constraints are weakened if the interaction is spin-dependent. This therefore provides another cogent example of the importance of a comprehensive program of complimentary DM searches.

The dijet narrow resonance searches, [7, 23], are relevant only for $\Gamma_{\rm med}/M_{\rm med} \lesssim 0.15$ in case of Gaussian shape or $\Gamma_{\rm med}/M_{\rm med} \lesssim 0.05$ for the Bright-Wigner (BW) case. In other cases, the mediator will escape the direct searches. Therefore, the maximal couplings that might be probed by the narrow resonance searches for Gaussian shape are

$$y_q < 1.1/\sqrt{N_q}\,, \qquad g_q < 1.4/\sqrt{N_q}\,, \tag{2.17}$$

and for BW

$$y_q < 0.65/\sqrt{N_q}\,, \qquad g_q < 0.79/\sqrt{N_q}\,, \tag{2.18}$$

where N_q is the number of quark flavours. Here we assume that the couplings to N_q quarks are equal to $y_q(g_q)$ for scalar and pseudo-scalar (vector/axial-vector) and both phase space effects and the coupling to the DM candidate are neglected.

The CMS dijet angular distribution [24] and the ratio between the central and forward dijet cross-sections given by ATLAS [25] can be used to constrain models which can escapes the narrow width searches. We note that the sensitivity of the angular distribution for relatively light mediators, $M_{\rm med} \lesssim 1$ TeV, is limited because of the large contribution from gluon fusion. In that case, it may be that Tevatron data can be used to better constrain the relevant parameter space, as discussed in ref [26] for example.

2.1.2 Expected sensitivity for monojet search at 14 TeV

We present the expected sensitivity of the search for DM candidates in events with a single jet and MET for the $\sqrt{s} = 14$ TeV run of the LHC using simplified models with a scalar / axial vector mediator. Similar results are expected for a pseudo scalar and vector mediator. Using Monte Carlo simulations for both background and signal, we derive prospective limits at 95% Confidence Level (CL) on the product of mediator to DM and mediator to SM couplings, $g_\chi g_q$, for a range of DM and mediator masses. The analysis is done for the 14 TeV run assuming 300 fb^{-1} data. We assume flavour independent couplings to quarks and consider only part of the parameter space where predominantly off shell production of DM occurs, i.e. $M_{med} \lesssim 2m_\chi$. In this regime the cross section is expected to be independent of the mediator width, except for the region where $M_{med} \approx 2m_\chi$. In order to guarantee pertubativity of the models we only probe the parameter space for which,

$$g_q, g_\chi \leq 4\pi \tag{2.19}$$

and

$$\frac{\Gamma_{med}}{M_{med}} \lesssim 0.5. \tag{2.20}$$

In the region where the production cross section depends on $\frac{\Gamma_{med}}{M_{med}}$, we take the pertubative limit, $\frac{\Gamma_{\rm med}}{M_{\rm med}} = 0.5$. In the heavy DM mass region, ($m_\chi \gtrsim 800$ GeV), where $y_\chi y_q \gtrsim 10.5$ for the scalar mediator and $g_\chi g_q \gtrsim 13$ for the axial vector mediator (which is outside our parameter space), one finds no sensitivity in the pertubative regime unless the mediator couples only to light quarks, thereby suppressing $\frac{\Gamma_{med}}{M_{med}}$.

The main background processes are $Z \to \nu\bar{\nu} + jets$, $W \to \ell\nu + jets$, where $\ell = e, \mu, \tau$, and single boson production (Z, W) with the jet coming from Initial State Radiation (ISR). We consider these in the leading order approximation. Other background processes, such as di-boson and $t\bar{t}+$ single top were not taken into consideration, as their contribution to the background is smaller by orders of magnitude [27].

The background and signal events were generated using `MadGraph` 5 [22] (with `MSTW2008` PDF [28]) for the hard process, and `Pythia` 6 [29], for showering and hadronization. For both signal and background we match the one and two jet samples. After the event generation, the interaction of the generated particles with the detector material and the detector response were simulated with `Delphes` 3.1.2 [30] and `ROOT` 5.3.4 [31], customised with the ATLAS detector geometry. Various signals with different $M_{\rm med}$ and m_χ were generated using the same machinery. All events were required to have $\not{E}_T > 120$ GeV, at least one jet with $p_{\rm T} > 130$ GeV and $|\eta| < 2.0$. Events with more than two jets and events with a muon or an electron with $p_{\rm T} > 30\,$GeV and $|\eta| < 2.0$ were rejected. For signal and background events, the leading jet $p_{\rm T}$ distribution was drawn using the same binning as in the ATLAS monojet analysis [27]. The limit on the product of the coupling constants, $y_\chi y_q$ and $g_\chi g_q$, was calculated by requiring that the probability to find the background plus signal $p_{\rm T}$ distribution assuming the background only hypothesis is less than 5%, or as we say, gives a p-value of 0.05, using Poisson statistics. The results are plotted in Fig. 2.7, allowing a first glimpse for the LHC sensitivity to the presented simplified models.

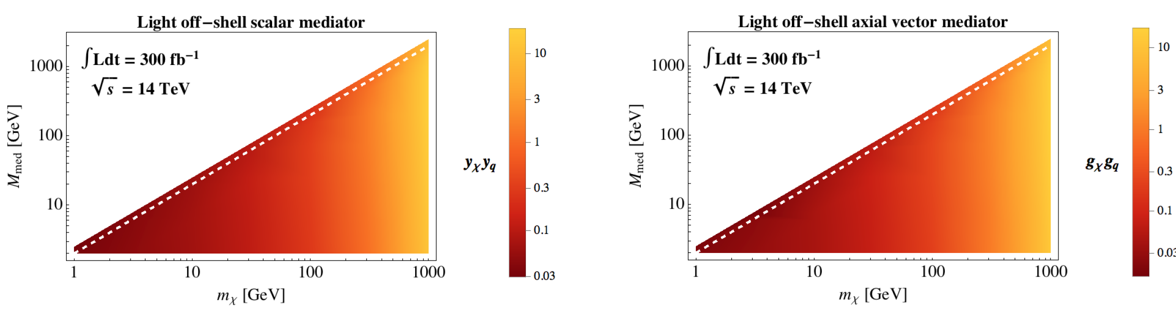

Figure 2.7: Expected sensitivity at 95% CL to the product of mediator coupling to DM and SM in the off-shell regime. The limits are derived for the expected operation of the LHC at 14 TeV with 300 fb^{-1} of data, assuming a scalar (left) and an axial vector (right) mediator. The dashed white line indicates the boundary where $M_{med} = 2m_\chi$.

Chapter 3

LHC and the ATLAS Detector

3.1 LHC

The Large Hadron Collider (the LHC) is a proton proton collider located at CERN, on the border between Switzerland and France. It is a ring collider, 27 km long in perimeter, inside a tunnel, dug originally for Large Electron Positron collider (LEP) in a depth which varies from 50 to 175 meters underneath the ground. As described in the schematic figure 3.1, the process of accelerating protons starts with hydrogen atoms, stripped out of electrons, leaving only protons. These protons then go through a series of accelerators, from each of which they leave with more energy. First is a linear accelerator, LINAC2 where they achieve energy of about 50 MeV, then they are injected into Proton Synchrotron Booster (PSB), and accelerated to the energy of 1.4 GeV, then into Proton Synchrotron (PS), to the energy of 26 GeV, then to Super Proton Synchrotron (SPS), to energy of 450 GeV and finally, they are injected as bunches to the main ring. The design beam energy of the LHC is 7 TeV. The proton bunches are injected to the main ring in opposite directions, there is a tube for protons in each direction, as they require opposite magnetic fields. There are four sites in which these tubes cross and the bunches of protons running in opposite directions can interact. Around each interaction point a detector was built in order to detect the outcomes of these interaction. The four main experiments are: LHCb, ALICE, CMS and ATLAS.

The LHC is designed to collide protons in the future with centre of mass energy of $\sqrt{s} = 14$ TeV, but throughout the time this thesis was written it was providing centre of mass energy of $\sqrt{s} = 8$ TeV during 2012 data taking period which is referred to as run-1, and later raised to $\sqrt{s} = 13$ TeV during 2015 data taking period, referred to run-2.

As in any scattering experiment, the rate of a specific process occurring is dependent on

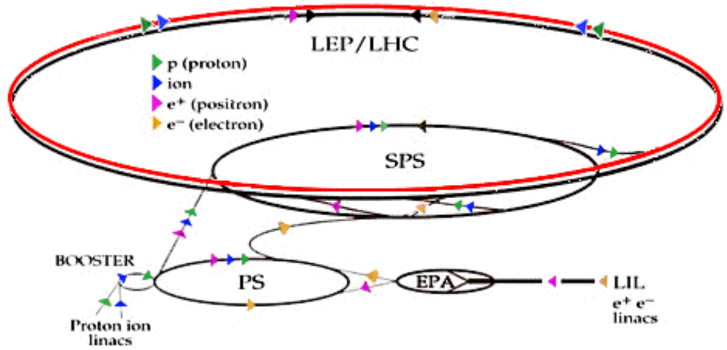

Figure 3.1: Schematic layout of the accelerator complex at CERN.

both the cross section of the process, σ, and the accelerator luminosity, $\mathcal{L}$:

$$R = \frac{dN}{dt} = \sigma \times \mathcal{L} \tag{3.1}$$

The luminosity is the flux of incoming particles in units of collisions per time per area, dependent only on the incoming beam parameters such as its frequency, size, number of proton within it etc. The luminosity is calculated as an average in each Luminosity-Block (LB), a period of approximately two minutes in which the luminosity is expected to be roughly constant. The cross section of the process is defined by the relation above and is also calculable by the amplitude of the process.

Since the LHC is on a mission to find NP which is expected to become apparent in rare events, it is aimed to produce many collision out of which those with interest will be kept by a dedicated trigger system as will be detailed in section 3.2.5. The beams carry bunches of approximately $1.15 \cdot 10^{11}$ protons, with bunch separation of either 50 or 25 nsec depending on the period of running. This mode of operation causes multiple interactions in each bunch crossing, and the detectors are bound to record in each bunch crossing multiple interactions. This phenomenon is referred to as pileup. One can distinguish between two types of pileup: the in-time pileup, which is the number of interactions in the same bunch crossing and the out-of-time pileup which is the pileup due also to interactions from a previous or later bunch crossing which can still affect the measured event quantities due to the short time between bunches. The in-time pileup can be characterised by the number of vertices reconstructed from the event tracks inside the volume where the two colliding bunches overlap, known as the Number of Primary Vertices (NPV). The total pileup is estimated by the average number of pileup interactions, $\langle\mu\rangle$, calculated from the average instantaneous luminosity:

$$\mathcal{L} = \frac{R_{\text{inel}}}{\sigma_{\text{inel}}} = \frac{\langle\mu\rangle n_{\text{b}} f_{\text{r}}}{\sigma_{\text{inel}}} \tag{3.2}$$

where, R_{inel} is the rate of inelastic proton proton collisions per revolution, n_{b} is the number of bunch crosses, f_{r} is the revolution frequency of the collider, and σ_{inel} is the cross section for inelastic proton proton interactions. Since the instantaneous luminosity is the average luminosity over a LB, $\langle\mu\rangle$ is also an average. The average is done for all bunch crossings in a LB, and not for each the particular bunch crossing associated with the process being studied. This way it corresponds to both averaged in-time and out-of-time pileup.

3.2 ATLAS

ATLAS, A Toroidal LHC ApparatuS, is a typical collider detector shaped as a symmetric cylinder, with its centre located in one of the LHC interacting point. The detector is built out of layers, each one consists of a barrel and two endcaps. The detector is divided into four main parts, two of which - the Inner Detector (ID) and the Muon Spectrometer (MS), are tracking detector, and the other two - electromagnetic calorimeter and hadronic calorimeter, located between the ID and MS are used to measure the energy of particles. A schematic layout of the ATLAS detector is shown in figure 3.2

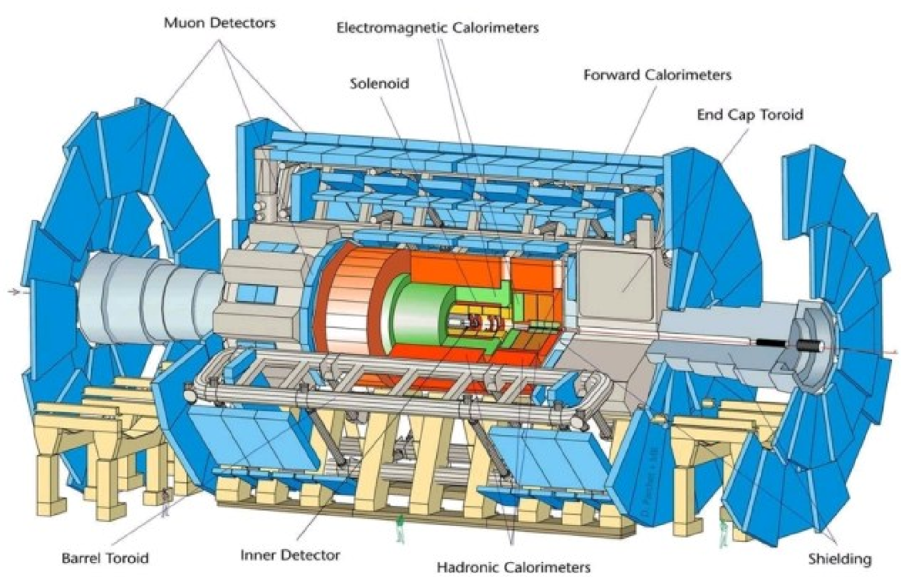

Figure 3.2: Schematic layout of the ATLAS detector

3.2.1 Magnets

There are several magnets within ATLAS. Each one is designed to create a magnetic field for a different region of the detector. When a charged particles will go through a region with a known magnetic field, from its curved track its momentum can be calculated. A central solenoid provides a magnetic field 2 T in magnitude parallel to the beam pipe, for the inner detector. A barrel toroid provides a toroidal magnetic field of 0.5 T to the barrel part of the muon spectrometer. The endcap toroids provides a toroidal magnetic field of 1.0 T to the endcaps of the muon spectrometer. Both toroids are air-core superconducting electromagnets. The air core design was made in order to minimise multiple scattering in the muon spectrometer.

3.2.2 Inner detector

The inner detector is the closest subdetector to the interaction point. It is designed to find the track and the momentum of a charged particle to a high resolution. The ID covers the range of $|\eta| < 2.5$ and all ϕ range. It is in a magnetic field of 2T, generated by the superconductive solenoid surrounding it. The ID consists out of three major parts, one inside the other, the pixel detector, surrounded by the SCT, which is surrounded by the TRT, as shown in figure 3.3.

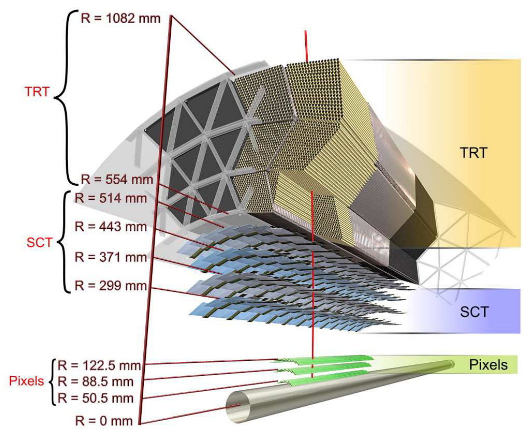

Figure 3.3: Schematic layout of the inner detector at ATLAS experiment

The pixel detector is built out of modules: a silicon sheet, with a grid of pn-junctions, each of which rests on a conductive sphere. When a charged particle goes through the silicon sheet, it can hand its energy to one of the electron in the full valence band, passing it to the conduction band leaving a hole behind. The free electron will pass through the sphere beneath it and will be measured. The pixels are arranged in the barrel in concentric cylinders arround the beam line, and in the endcaps, on disks perpendicular to the beam line. The size of each pixel is 50 μm in the $r\phi$ direction, and 300 μm away in the z direction. The pixel detector is also used to reconstruct the primary and secondary vertices.

The SemiConductor Tracker (SCT) is built out of silicon microstrips. It works similarly to the pixel detector, only with strips instead of pixels.

The Transition Radiation Tracker (TRT) is a drift tube tracking detector. It consists of straws, 4 mm in diameter filled with a gas mixture of Xe, CO_2, and O_2. Each straw contains a gold plated tungsten wire with a potential difference between the straw and the wire. A charged particle passing through a straw ionises the gas, causing a current signal through the wire. The time it takes for the charge to be measured is proportional to the 'drift radius' - the closest approach of the track to the wire. The resolution of the drift radius is 170 μm. The amount of charges collected by the straws is being used to distinguish between types of particles - especially between electrons and hadrons. Electrons passing through the gas are accompanied by more photons due to transition radiation, generated as the particle is passing through the different straws. The number of photons produced is proportional to $\gamma = E/m$. The more photons, the more ionized gas atoms, leading to a larger current.

Towards the increase of the centre of mass energy and the luminosity in the second running period of the LHC at 2015, the radiation damage to the innermost layers of the detector was expected to increase respectively. The insertable B-layer, a new pixel detector layer which is more resistant to the radiation was inserted around the beam pipe after its diameter was reduced.

3.2.3 Calorimeters

Calorimeters are the part of the detector made to measure the energy of particles and their direction. The particles passing through the calorimeter can interact electromagnetically or strongly with the material in its volume. An energy deposited in the calorimeter can be measured by the amount of light, charge and or heat produced in it. ATLAS calorimeters are sampling calorimeters. They are made of passive material, and in between, there are layers of active material. The passive material is a high density material, where the particle interact. In case a particle has high energy it can produce a shower of particles. The active material is where the energy of all particles is being measured. In a sampling calorimeter, part of the energy is absorbed in the passive material and not being measured, so the total energy is only an estimation. There are two main parts of the calorimeter, the ElectroMagnetic (EM) calorimeter and the surrounding hadronic calorimeter. There is an endcap cryostat, containing the electromagnetic and the hadronic wheels.

This analysis is mainly based on the calorimeter measurements, as jets are defined via the energy deposition of electromagnetic and hadronic showers in the two calorimeters.

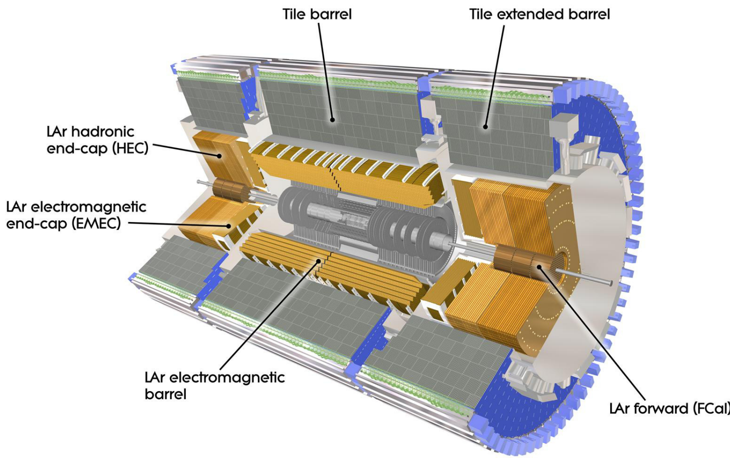

Figure 3.4: Schematic layout of the ATLAS' calorimeters

The electromagnetic calorimeter

The EM calorimeter is designed to trigger and give precision measurements mainly of electrons, photons, jets and indirectly MET. Electrons and positrons lose energy due to ionisation and bremsstrahlung, and high energy photons interact via pair production. These process will occur again and again, each time doubling the number of particles and creating a *shower*. Showers of muons (via bremsstrahlung) are negligible up to muon energy of about 500 GeV. The passive material is lead, and the active is Liquid Argon (LAr). It has accordion shaped electrodes in order to minimize the gaps by creating azimuthal uniformity, without cracks. The barrel part of the EM calorimeter is built out of two half-barrels with a gap of few mm between them. It is 6.8 m long, inner radius of 1.15 m and outer radius of 2.25 m and covers $|\eta| < 1.475$. The endcaps covers $1.375 < |\eta| < 3.2$ with two wheels on each side with an outer radius of 2 m. In the inner part of the EM calorimeter, where $|\eta| < 1.8$, there is a presampler, composed out of an active LAr layer with electrodes, which measures the deposited energy by the track. This is used to correct the energy of the particle in case it interacts with the detector dead material before reaching the calorimeter. There is no presampler in the area where $|\eta| > 1.8$, because there is less dead material, and the particles going in this direction have relatively higher energy. In the region between the barrel and the endcaps, $\eta = 1.4$, there is a scintillator layer between the two cryostats to recover mainly jet energies. There are three layers of samplings. The thickness of the passive material in radiation length is 6 in the inner part, 16 in the middle part, and 2-12 in the outer part. The resolution of the EM calorimeter can be parameterized as: $\frac{\sigma(E)}{E} = \sqrt{(\frac{a}{\sqrt{E}})^2 + (\frac{b}{E})^2 + c^2}$, where the first term is a stochastic term, the second term is due to electronic noise, and the third originates from local non-uniformities in the response of the calorimeter. For ATLAS $a = 0.1$, $b = 0.005$ and $c = 0.007$.

The hadronic calorimeter

Surrounding the EM calorimeter, the hadronic calorimeter is designed to measure the energy of hadrons, in particular the neutral ones which do not leave any track in the inner detector. The hadronic calorimeter also prevents any hadron to penetrate it and arrive to the muon spectrometer. This calorimeter is divided into the hadronic tile calorimeter, the Hadronic EndCap (HEC) calorimeter and the hadronic forward calorimeter.

The hadronic tile calorimeter is built out of steel as the passive material and plastic scintillators as the active material. It consists of one central barrel 5.8 m long, covering $|\eta| < 0.8$ and on each side, an extended barrel, 2.6 m long covering $0.8 < |\eta| < 1.7$. All the barrels have an inner radius of 2.28 m and an outer radius of 4.25 m.

The hadronic endcap calorimeter is built out of copper as passive material and LAr as active material. It is located inside the hadronic tile calorimeter extended barrels, and covers $1.5 < |\eta| < 3.2$. On each side there are two identical wheels with an outer radius of 2.03 m.

The hadronic forward calorimeter has to cope with high level of radiation. Its active material is liquid argon. It is located inside the endcap cryostat, inside the hadronic endcap calorimeter, and covers the region of $3.1 < |\eta| < 4.9$. It consists of three sections, in the first one, the passive material is copper, and in the other two, it is tungsten. In each section the calorimeter consists of a metal matrix with regularly spaced longitudinal channels filled with concentric anode rods inside tubes. The rods are at positive high voltage while the matrix is grounded.

Additional coverage is needed in order to compensate the 60 cm gap between the barrel and the extended barrel, needed for the ID and LAr services; The gap scintillators are installed between the tile barrel and extended barrel at $1.0 < |\eta| < 1.2$, and crack scintillators are installed in front of the LAr endcap at $1.2 < |\eta| < 1.6$.

3.2.4 Muon spectrometer

The MS is the outer subdetector in ATLAS, designed to measure the tracks of muons, and to trigger on them. It is located in a region with a magnetic field created by the air-core toroid magnetic system. The MS covers the region of $|\eta| < 2.7$ with holes around $|\eta| = 0$ and $|\eta| = 1.2$. The barrel part consists out of 3 layers at 5, 7.5 and 10 m from the beam line, and divided into 16 azimuthal sections. The two endcaps are built out of three wheels on each side at 7.4 m, 14 m and 21.5 m from the interaction point. It is possible that a very low momentum (few GeVs) muon will not penetrate through the outer layers of the detector and thus will not be identified properly by the MS. The MS has four subsystems, two of which are used for triggering: Thin Gap Chambers (TGC) and Resistive Plate Chambers (RPC). The other two are used for precsision measurement of the muon track: Monitored Drift Tubes (MDT) and Cathode Strip Chambers (CSC).

The TGC provides triggering in the endcaps region, where $1.05 < |\eta| < 2.7$. The TGC forms four parallel wheels on each side of the detectors. Each wheel consists of either a doublet or a triplet of multi-wire proportional chambers, each filled with a gas mixture of CO_2 and nC_5H_{12}. Inside each chamber there are anode wires, made of gold plated tungsten, and cathode strips which are perpendicular to the wires. When a charged particle will pass through the gas, it will ionize it and create a negative (positive) signal in the wires (strips) which is measured. More details on the TGC units and their validation tests will be given in chapter 5.

The RPC provides triggers in the barrel region, where $|\eta| < 1.05$. RPC chambers, arranged in towers of three concentric barrels, composed of units filled with a gas mixture of $C_2H_2F_4$, isoC_4H_{10} and SF_6. The plates are coated from the inside with graphite and connected to the high voltage system.

The MDT, provides precision measurements in the barrel region $|\eta| < 2.7$. It is made of aluminium tubes 30 mm in diameter, filled with 93% Ar and 7% CO_2 gas mixture at a pressure of 3 bar. Inside each tube, there is a gold plated tungsten wire. There is a high voltage difference of 3040 V between the wire and the tube. The MDT works in the same way as the TRT in the inner detector. A single MDT has a resolution of 80 μm but a chamber with few layers of tubes reaches a resolution of 35 μm.

The CSC provides precision measurements in the endcaps region $2.0 < |\eta| < 2.7$. The CSC is a multi-wire proportional chamber, composed out of radial anode wires, and cathode strips perpendicular to the wires. The CSCs have a precision of 40 μm in the bending plane and 5 mm in the non-bending plane.

3.2.5 Triggers- online selection

Due to the large amount of events and the size of data representing each event, ATLAS reads and stores only events with higher chance of being interesting. These events are selected online by the trigger system. In the first period of data taking, there were three trigger levels [32]. The first, a Level one trigger (L1), is an hardware based trigger which uses limited information from the MS trigger chambers and the calorimeter. It triggers on events with high p_{T} muons, electrons, photons, jets, taus and missing E_{T}, and defines Regions of Interest (RoIs) in the detector, to be further checked by the higher trigger levels. Level two trigger (L2) is software based, seeded by the RoIs defined in L1. It reconstructs physics objects using information from all the subdetectors. The third level is the Event Filter (EF) which is software based, and uses the full reconstruction of the event, with algorithms and object definitions similar to those being used offline.

Towards the second data taking period, run-2, ATLAS trigger system has been modified and nowadays consists of two main levels [33]: L1, as before, and the High Level Trigger (HLT). The HLT is software based and reconstructs physics objects using information from all the subdetectors giving a full reconstruction of the event. As in the case of the EF, this trigger uses algorithms and object definitions very similar to those being used offline. The run-2 trigger system is the one relevant for the trigger level analysis described in section 4.3.

Several additional trigger levels were considered as additions to the trigger system during the years. L1Topo was one of the promising options, but still not in common use in physics analyses [34]. This is a topological processor applied on L1 RoIs and it was aimed to filter events using a topological selection consisting of logical combination between several cuts on kinematic variables, for example selecting an event with at least two jets with defined p_{T} and m_{jj} cuts. The L1.5 option is an alternative to the old L2 trigger algorithm. The L1.5 uses data produced by the L1 calorimeter trigger to reconstruct jets across the entire detector (and not only in RoIs) [35].

The trigger selection can be insufficient in some cases to reduce the rate of events directed to storage, forcing the application of a prescale factor, p, on some triggers, such that only a fraction, $1/p$, of events passing a trigger will be kept and recorded. The prescale factor can vary in time during the run.

3.2.6 Offline analysis environment

Athena is the ATLAS software framework. It provides a software skeleton and was designed to handle data and simulation in the same way. The byte stream from ATLAS is converted to Raw Data Objects (RDOs) containing for each event the hits in the various ATLAS subdetectors, as well as the trigger and general event information. These hits are reconstructed by Athena into tracks in the tracking chambers and energy clusters in the calorimeters, identifying particles such as hadrons, electrons, photons, muons and taus decaying into hadrons. The data is finally written in an Analysis Object Data (AOD) format, which was modified to an xAOD in the second data taking period, containing all the event information, and objects such as four vector of particles. The analysis environment is based on `ROOT` [31], and the AOD or xAODs are skimmed to obtain files with reduced size containing only the information required for a specific analysis.

3.2.7 MC simulation

A Monte Carlo program is responsible for generation of a physics process. After the event generation, the interaction of the generated particles with the detector material and the detector response are simulated, with an algorithm based on the `Geant4` software [36], and customised with the ATLAS geometry, `G4atlas`. The simulated hits in the various parts of the detector, are transformed into RDOs, treated in the same way as data RDOs.

In order for the simulated events to be comparable to events from the data, the accelerators operation conditions in the MC generator has to match those of the LHC. In a high luminosity proton collider one of the important characteristics is the amount of pileup. Since the MC generation takes a long computation time, it has started before the data taking period, long before the luminosity and pileup conditions were known. The events were simulated with a flat $\langle \mu \rangle$ distribution. Since the data for each analysis was taken during a long periods, in which the luminosity has changed, and since the analysis is based on energy measured in the calorimeter, it is crucial to apply different weights for each simulated event, so that the simulated $\langle \mu \rangle$ distribution will match the one from data.

Both data and simulated events were reconstructed and analyzed via the same software.

Chapter 4

Dijets

4.1 Introduction

Since 2010, when the first proton beams were collided at the LHC, the data obtained is saved and being analyzed. So far, all the results of the analyses based on LHC data, showed remarkable compliance with the known SM. With the expected increase of energy and luminosity of the LHC in the 2015 run, a new window of opportunity has been opened for searches for NP beyond the SM. The searches focus on deviations from the SM. Among the high p_{T} production processes expected at the LHC, the two jet (dijet) production has the largest cross section. One of the most promising signature of new particles interacting with quarks and gluons at the LHC is a narrow resonance emerging in the distribution of m_{jj}, the invariant mass of the two leading jets in the event. Specifically in a proton proton collider such as the LHC, any new particle is produced by the interaction between two partons, and therefore. it has to decay into two partons, among all other decay channels, and the two partons will be seen at the detector as two jets. This is not the case for other final states such as di-leptons. The dijet mass resonance search is a well-established search [10, 37], that is sensitive to local excesses from new resonances. The QCD background is estimated from data using a fit function that is unable to accommodate narrow fluctuations. The search for new resonances is performed using the `BumpHunter` algorithm [38]: a new particle would appear as a narrow excess in the data above the expectation [39]. According to QCD, the largest contribution to dijet production in QCD comes from the t-channel exchange, whereas the contribution from new phenomena is usually expected to come from s-channel processes. These processes differ in the distribution of the scattering angle in the dijet centre of mass frame.

The dijet mass resonance search is known to be one of the first published searches in any new run of the LHC, enabling so far to set limits on models with resonances in higher masses. At the LHC this search was not efficient in lower regions of the invariant mass spectrum (below 1 TeV) due to the high rate of QCD background events, far beyond the acceptable detection rate due to trigger and data storage limitation. The new Trigger Level Analysis (TLA) which will be described in section 4.3 is enabling this search for the first time. A different approach to search for new phenomena is to study the angular distribution of the two jets as will be described in section 4.2. In case no NP will be discovered, the purpose of the analysis is aimed at setting exclusion bounds on some suggested models extending the SM, which will be described in section 4.1.1.

Previous studies have used data from 2011 with $\sqrt{s} = 7$ TeV, with integrated luminosities of 4.8 fb^{-1} by ATLAS [40] and 2.9 fb^{-1} by CMS [41]. In these studies, no excesses have been spotted in the dijet invariant mass distribution, and the angular distributions [24, 42] were consistent with the SM predictions.

4.1.1 Theoretical background

The dominant background to NP in dijet events are QCD processes. Two incoming partons, one from each proton with 4-momenta p_1 and p_2, will interact and produce two outgoing partons with 4-momenta p_3 and p_4. Outgoing partons with large enough transverse momenta will be observed in the detectors as jets. The cross section for this process is:

$$\frac{d^6\sigma}{d^3p_3 d^3p_4} = \frac{1}{E_3 E_4}\frac{1}{2\hat{s}}\frac{1}{16\pi^2}\bar{\sum}|\mathcal{M}|^2\delta^4(p_1 + p_2 - p_3 - p_4) \tag{4.1}$$

where $\bar{\sum}$ is the sum (avarage) over the final (initial) state spins and colors, $\mathcal{M}$ is the matrix element which is dependent on the types of partons in the process and $\hat{s}$ is the Mandelstam variable: $\hat{s} = (p_1 + p_2)^2$. Some of the lowest order processes contributing to the production of the dijet signature are shown in figure 4.1.

Two main models have been considered in the analysis for the limit setting phase. The first model is the EFT of Contact Interaction (CI) or four-fermion interaction which can describe a new physics interaction mediated by a particle which is too heavy to be directly observed at LHC. In case the known quarks are composed out of several constituents, CI could also describe the interaction between these constituents. This new interaction, if exists, is expected to be suppressed by a scale factor Λ. This factor can also be referred to as the substructure scale, which is the mass scale of the mediator between the constituents. The effective Lagrangian for such an interaction would look as [43–45]:

$$\mathcal{L}_{qqqq}(\Lambda) = \frac{g^2}{2\Lambda^2}(\eta_{\mathrm{LL}}\bar{f}_{\mathrm{L}}\gamma^\mu f_{\mathrm{L}}\bar{f}_{\mathrm{L}}\gamma_\mu f_{\mathrm{L}} + \eta_{\mathrm{RR}}\bar{f}_{\mathrm{R}}\gamma^\mu f_{\mathrm{R}}\bar{f}_{\mathrm{R}}\gamma_\mu f_{\mathrm{R}} + \eta_{\mathrm{LR}}\bar{f}_{\mathrm{L}}\gamma^\mu f_{\mathrm{L}}\bar{f}_{\mathrm{R}}\gamma_\mu f_{\mathrm{R}}) \tag{4.2}$$

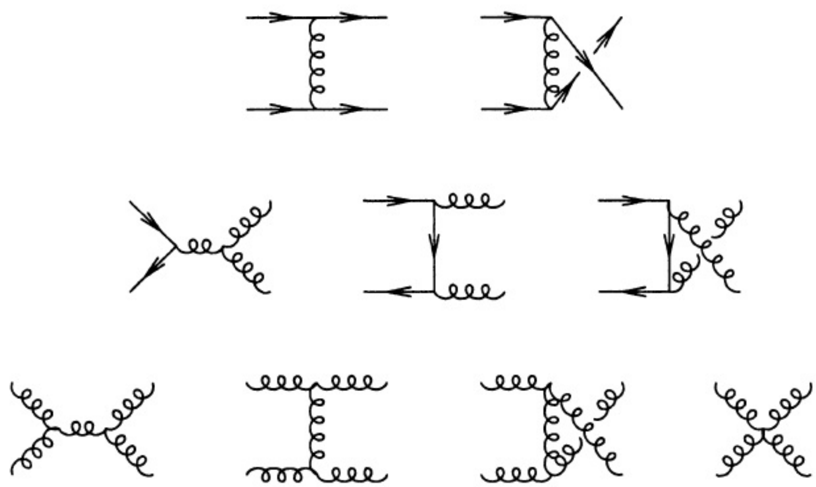

Figure 4.1: Some Feynman diagrams of dijet production processes.

where g is the coupling constant, chosen such that $\frac{g^2}{4\pi} = 1$, f_{L} (f_{R}) are left-handed (right-handed) fermion fields and each of the η coefficients can be set to ± 1 or 0, according to the particular model which is being considered, $+1$ for destructive and -1 for constructive interference with the SM amplitude. In this analysis only the first term, representing the left left interaction is considered.

As described in chapter 2, there is an advantage to choose a simplified model, so the second model chosen is a production of an axial vector, named Z', which can act as a mediator between SM quarks and a dark sector, and has a decay channel to a $q\bar{q}$ pair.

4.1.2 Jet reconstruction

As quarks and gluons cannot be observed in a detector due to their color and the phenomenon of confinement, they will fragment into collimated jets of hadrons. In the detector, the hadrons will show up as topological clusters in the calorimeter. The energy and momentum of each hadron is taken from the measured energy and position of the topological cluster assuming zero mass. These hadrons are combined with a clustering algorithm, to form a jet within a defined cone in the $\eta - \phi$ plane with size R, with the estimated jet energy, mass and momentum obtained by the vector sum of all the associated hadron momenta [46].

The basic entity which is used to define a jet is a topological cluster (topocluster) of different cells in the calorimeter. To reconstruct the topoclusters, the energy deposition in each calorimeter cell is compared with the noise level, σ, which is a quadrature sum of the electronic and pileup noise. The seed of a topocluster is defined as a calorimeter cell where the ratio between the energy deposition and the noise level is at least four. A topocluster will be defined as the seed, its surrounding cells for which this ratio is at least two and further layer of surrounding cells.

A family of jet reconstruction algorithms is introduced, using the following distance parameters:

1. d_{ij} is the distance between two entities, i and j. These entities can be single topoclusters or pseudo-jets (see below), and the distance is defined as $d_{ij} = \min(\mathrm{k}_{\mathrm{Ti}}^{2\eta}, \mathrm{k}_{\mathrm{Tj}}^{2\eta})\frac{\Delta_{\mathrm{ij}}^2}{\mathrm{R}^2}$, where k_{Ti} is the transverse momentum of entity i, R is the chosen cone size, Δ_{ij} is the ΔR between the two entities, and η is a parameter of the algorithm (see below).
2. d_{iB} is the distance between entity i and the beam (B), and is defined as $d_{iB} = k_{\mathrm{Ti}}^{2\eta}$

The clustering procedure identifies the smallest of all distances. In case this is d_{ij}, it combines entities i and j into a new entity, a pseudo-jet, and it will be used in the next iteration. In case this is d_{iB}, it will be defined as a jet, and will be removed from the list of entities considered for the next iteration. This procedure is being repeated until there are no entities left. Different values for the parameter η will change the effect of the entity transverse momentum on the clustering. The Cambridge/Aachen algorithms ignores the transverse momentum by setting η to be zero, the inclusive k_{T} (anti-k_{T}) algorithms set η to be 1 (-1) and thus, starts each jet clustering procedure with the low (high) transverse momentum entities. Figure 4.2, for example, shows the performance of the anti-k_{T} algorithm to cluster in different jets simulated energy depositions of simulated particles in the $\phi - y$ plane. The anti-k_{T} algorithm, produces relatively round jets and their shape is more resilient to the effects of soft radiation.

In the dijet analyses the clustering algorithm used is anti-k_{T} [47] and the cone size considered are either $R = 0.6$ or $R = 0.4$, referred to as anti-$\mathrm{k_T}$6 and anti-$\mathrm{k_T}$4 respectively. The choice of R was recently studied for the dijet mass resonance analysis [7]. The argument for using a larger cone size is as follows: The final size of an anti-$\mathrm{k_T}$ jet is strongly dependent on the jet radius, so when choosing the larger radius, one would expect to find larger jets, that are able to catch more final state radiation. For searches it is important that the sensitivity to new physics signals is increased. In Ref [7], the dependence of the sensitivity to a simulated narrow resonance signal on the distance parameter is examined, comparing $R = 0.4$ and $R = 0.6$. It is found that the choice of distance parameter has only a minor effect on the sensitivity to the signal, and thus it is preferred to be consistent with previous analyses and use $R = 0.6$ for offline reconstructed jets.

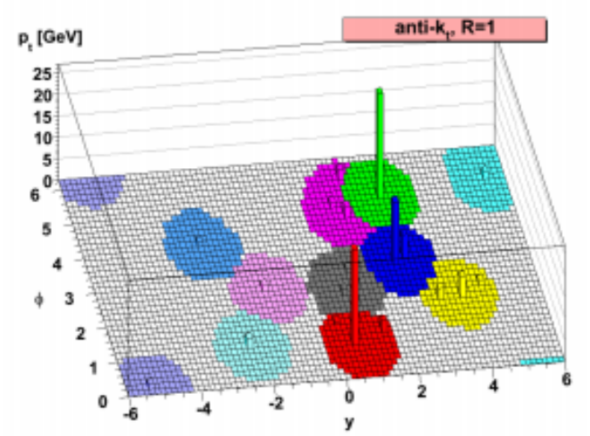

Figure 4.2: An anti-k_T clustering performance as done on a sample of parton-level simulated event, taken from [47]. Each reconstructed jet is marked with a different color.

4.1.3 Jet triggers

Jet triggers are aimed to select events which have jets passing some cuts. Specifically the single jet triggers are triggers aimed to select events containing at least one jet passing a transverse energy (E_T) threshold. As all other triggers, also jet triggers are designed as a chain of an `L1` jet trigger seeding for an `HLT` jet trigger.

The `L1` trigger jet [48] is getting as input the energy deposition in each trigger tower, defined as the sum of energy deposited in all the cells in a specific region of $\Delta\eta\times\Delta\phi = 0.1\times0.1$ in each calorimeter in the range of $|\eta| < 3.2$. A jet ROI is defined as a 2×2 trigger tower configuration, in which the sum of E_T is greater compared to all neighbouring 2×2 trigger towers. A jet trigger candidate is usually bigger (either 3×3 or 4×4 trigger towers) and it is chosen using a sliding window of its size moving over the ROIs. The window with the greatest sum of E_T is considered as a jet trigger candidate. `L1` jet triggers are available for various E_T threshold and window sizes.

The `HLT` for jets is a software based and so aims to cluster jets as close as possible to the offline jets. Since jets along with their E_T and direction, are defined by their clustering algorithms, and since these jet kinematic variables are highly affected by the choice of calibration, there are several `HLT` triggers, for each clustering algorithm and calibration. Topoclustering [49] is run within the `HLT` software using the same parameters as offline jet clustering, taking the input cells from the entire calorimeter. There are various possibilities for the calibration of these trigger jets, for example jets with or without pileup suppression, jets in the EM scale, or jets after calibration to the hadronic scale (as will be described in details in section 4.1.5). The dijet analyses are making use of trigger jets reconstructed with anti-k_T4 or anti-k_T6.

The single-jet trigger rates are many orders of magnitude higher than the other high-p_{T} triggers, and the data sample would be dominated by low-p_{T} events. To offset this effect, in order to collect significant samples of high-p_{T} events, the rate of each low-p_{T} trigger is reduced by a prescale factor, p_i, where i stands for the ith trigger. The data stream resulting from all such `HLT` triggers, and recorded for prompt processing, is called the *normal* stream. In addition, at a rate of approximately 200 Hz, ATLAS stores events for later reconstruction. This is called the *delayed* stream. Often, the content of this stream is derived from a different set of triggers.

Each analysis has a trigger strategy, choosing the most appropriate set of triggers with the purpose of achieving maximum sensitivity without causing any bias. Given the several jet triggers available for jet analyses in ATLAS, a specific jet is potentially triggered by more than one jet trigger, and an event with more than one jet is potentially triggered by more than one jet. Since each of these jet triggers has a different prescale, a strategy is needed in order to apply the correct weight to each event. For each jet, the chosen trigger out of all the jet triggered which have fired, will be the trigger with the highest threshold and thus, with the lowest prescale, provided that it has a satisfactory efficiency for the specific jet E_{T} of above 99.5%. In case of an analysis which aims for the lowest kinematic range available, such as the TLA, only the lowest available unprescaled `L1` trigger is chosen, without concerning the jet E_{T} in the event, and the event selection is modified to accommodate the kinematic range in which the trigger is fully efficient. The following sections describe a study of an unambiguous definitions for trigger efficiency and its error used for all the dijet analyses, and the strategy for applying weights to data events, which is used in both dijet angular analysis and the regular (non-TLA) mass resonance search.

Trigger efficiency

The trigger efficiency is calculated using all events triggered by a lower threshold reference trigger and passing the event selection (see below, not including the m_{jj} and p_{T} cuts). The trigger efficiency is defined as:

$$\epsilon = \frac{K}{N} \tag{4.3}$$

where K is the number of events passing the tested trigger, and N is the number of events passing a reference trigger with the lower E_{T} threshold. In case N and K are large enough, their error can be regarded as a Poisson error, $\sqrt{N}$ and $\sqrt{K}$ respectively.

Several ways to calculate the efficiency uncertainty were tested [50]:

1. The Poisson Error: assuming K and N are independent, each of which has a Poisson

distribution and error, as mentioned above. The efficiency uncertainty is then:

$$\Delta\epsilon = \frac{K}{N}\sqrt{\left(\frac{\Delta K}{K}\right)^2 + \left(\frac{\Delta N}{N}\right)^2}$$

This assumption of independent K and N should be corrected with taking into account the correlation between the two. This correlation can be neglected only in case N is much larger than K. This method cannot be used for the case where N and K are too small and the Poisson error assumption fails nor for weighted events.

2. The Binomial Error: assuming the efficiency is the probability of passing the cut, and has a binomial distribution, its error will be:

$$\Delta\epsilon = \sqrt{\frac{\epsilon(1-\epsilon)}{N}}$$

Not knowing the true value of the efficiency, it is possible to use the estimate measured value of N/K giving the efficiency uncertainty of:

$$\Delta\epsilon = \frac{1}{N}\sqrt{K\left(1 - \frac{K}{N}\right)}$$

This method is valid only when K is not too close to 0 or to N, and when the number of events passing the cut is a subset of the total number of events. It cannot be used with weighted events.

3. The Poisson Error using Weights: Here N is the sum of weights of all events and K is the sum of weights of all events passing the trigger. Therefore, K and $N - K$ can be considered as independent random variables and the efficiency uncertainty is:

$$\begin{aligned}\Delta\epsilon &= \sqrt{\left(\frac{\partial\epsilon}{\partial K}\right)^2 (\Delta K)^2 + \left(\frac{\partial\epsilon}{\partial(N-K)}\right)^2 (\Delta(N-K))^2} \\ &= \sqrt{\frac{N^2 - 2KN}{N^4}(\Delta K)^2 + \frac{K^2}{N^4}(\Delta N)^2} \qquad (4.4)\end{aligned}$$

where ΔK and $\Delta(N-K)$ are calculated as the square root of the sum of all squared weights of the events considered in each one of them, and $(\Delta N)^2 = (\Delta(N-K))^2 + (\Delta K)^2$. Note that in case there are no weights applied, $\Delta K = \sqrt{K}$ and $\Delta N = \sqrt{N}$ and we get the binomial error. This method is valid if $K > 0$ and if the events passing the cut are a subset of all the events.

4. Error calculation based on Bayes theorem: if the Binomial probability to get a certain K, given ϵ and N is:

$$P(K|\epsilon, N) = \frac{N!}{K!(N-K)!}\epsilon^K(1-\epsilon)^{N-K} \qquad (4.5)$$

then the probability to get ϵ given K and N is:

$$P(\epsilon|K,N) = \frac{P(K|\epsilon,N)P(\epsilon|N)}{Z} = \frac{\Gamma(N+2)}{\Gamma(K+1)\Gamma(N-K+1)}\epsilon^K(1-\epsilon)^{N-K} \tag{4.6}$$

where Z in a normalization factor. This function will have a peak at the measured efficiency: $\epsilon = \frac{K}{N}$, and we can calculate the boundaries of its error as the values of ϵ, between which the integral of the function equals to 68.3%. This method is valid anywhere, and works also with weighted events, where N and K are taken as the sum of weights.

A validation of the four different methods was made by generating several samples of events, each with different N ($N = 10^3, 10^5, 10^7$). For each sample, K was calculated for different true efficiencies (using a random binomial variable), and the efficiency with its different errors was calculated. Figure 4.3 shows the different errors which were calculated using the four different methods for a sample of 1000 events with no weights. The error calculation based on Bayes theorem was chosen, as it is valid anywhere. Since no weights were applied, the binomial and weighted binomial method of calculation of the efficiency uncertainties give the same values.

In order to choose the triggers for the analysis, all trigger efficiencies were tested in bins of p_{T}, as shown, for example, in figure 4.28.

Event weight

When choosing only the events passing the trigger on the jet with the highest p_{T} (leading jet) in the event, we lose a non-negligible number of events in each m_{jj} bin. This is because an event might be triggered by its subleading jet, and not by the leading one, due to the randomness of the prescale procedure. Therefore, an inclusive method [51] is used, considering both the leading and subleading jets in an event. The analysis takes into consideration events passing at least one out of the two triggers relevant to the leading and subleading jet p_{T}. Such an event will be given a weight with consideration of both triggers prescales:

$$w = \frac{1}{\frac{1}{p_1} + \frac{1}{p_2} - \frac{1}{p_1 p_2}} \tag{4.7}$$

where p_i is the prescale factor of trigger i.

The prescale factor of the relevant triggers have strongly varied in different LB of data taking. In order to avoid spikes in the analysed distribution caused by single events with

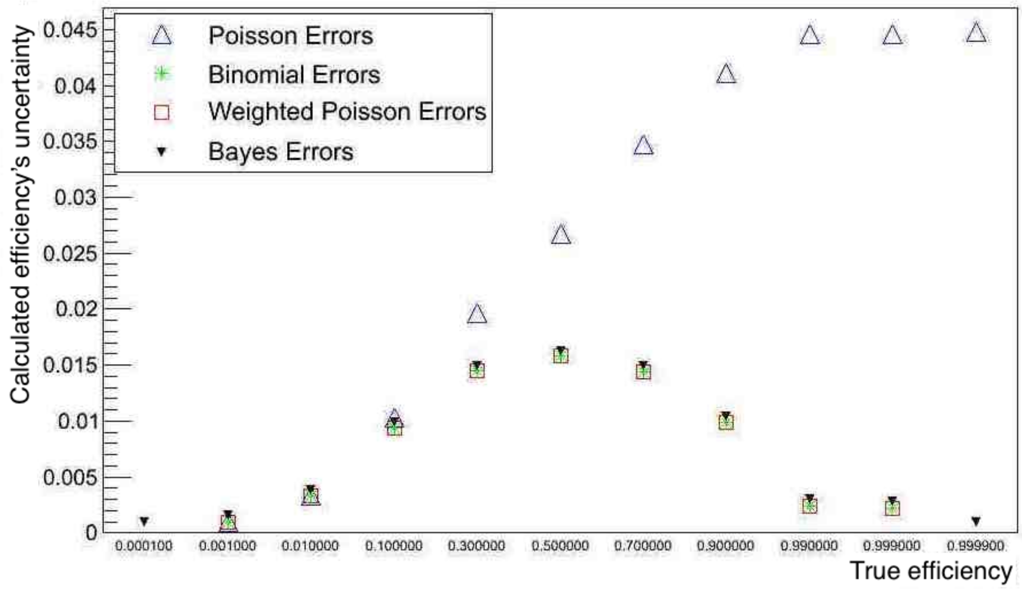

Figure 4.3: The calculated efficiency uncertainty using the four methods described in section 4.1.3 vs. the true efficiency of a generated sample of 1000 unweighted events. Zero efficiency is not shown in the plot.

high weights due to high prescale, we choose to use the average prescale for each trigger. Ignoring the trigger efficiency, the average inverse prescale, $\langle p \rangle$, is given by:

$$\langle \frac{1}{p} \rangle = \frac{\sum_{i=1}^{N} \mathcal{L}_i \cdot \frac{1}{p_i}}{\sum_{i=1}^{N} \mathcal{L}_i} \tag{4.8}$$

where i runs over all LBs, each one with luminosity $\mathcal{L}_i$ and prescale factor p_i.

4.1.4 Jet cleaning

As in all jet analyses, a cleaning procedure is needed to avoid using jets coming from sporadic noise bursts, beam induced background or cosmic showers. A great advantage of the dijet analysis is that its topology of two central jets with a small rapidity separation is already effective in rejecting events with these features, since they usually give rise to single-jet events. The following variables have been found to be effective in discriminating between jets coming from the reasons mentioned above, referred to as *fake* jets, and those coming from quarks and gluons, referred to as *real*:

1. $f_{\mathrm{HEC(EM)}}$ - fraction of energy in HEC (EM) calorimeter out of the entire jet energy
2. $Q_{\mathrm{cell}}^{\mathrm{LAr}}$ - quadratic difference between measured and predicted pulse shapes computed using four samples of pulse shapes, and is defined as: $Q_{\mathrm{cell}}^{\mathrm{LAr}} = \sum_{j=1}^{4}(s_j - A(g_j - \tau g'_j))^2$, where A is the measured amplitude of the signal, τ is the measured time of the signal, s_j is the amplitude of sample j, and g_j, g'_j are the normalised predicted shape and its time derivative.
3. $\langle Q \rangle$ - energy squared weighted average of the pulse quality of the LAr calorimeter cells ($Q_{\mathrm{cell}}^{\mathrm{LAr}}$) in the jet, normalised such that $0 < \langle Q \rangle < 1$.
4. $f_{\mathrm{Q}}^{\mathrm{HEC(LAr)}}$ - fraction of the energy in the HEC (LAr) calorimeter cells of a jet with poor signal shape quality defined as $Q_{\mathrm{cell}}^{\mathrm{LAr}} > 4000$.
5. E_{neg} - energy sum of all cells with negative E (due to electronic and pileup noise)
6. f_{ch} - ratio of the scalar sum of the p_{T} of the tracks coming from the primary vertex associated to the jet divided by the jet p_{T}
7. f_{max} - maximum energy fraction in any single calorimeter layer.

The cleaning procedure used for fully reconstructed and calibrated jets is based on a study of these variable distributions for real and fake jets from data and simulated dijet events. A *looser* criterion is chosen as it has a negligible inefficiency and the remaining fake rate after cuts at high jet p_{T} has been shown to be small. A jet will not pass the cleaning procedure if it satisfies one of the following conditions [52]:

1. $f_{\mathrm{HEC}} > 0.5$ and $\left|f_{\mathrm{Q}}^{\mathrm{HEC}}\right| > 0.5$ and $\langle Q \rangle > 0.8$
2. $|E_{\mathrm{neg}}| > 60$ GeV
3. $f_{\mathrm{EM}} > 0.95$ and $f_{\mathrm{Q}}^{\mathrm{LAR}} > 0.8$ and $\langle Q \rangle > 0.8$ and $|\eta| < 2.8$
4. $f_{\mathrm{max}} > 0.99$ and $|\eta| < 2$
5. $f_{\mathrm{EM}} < 0.05$ and $f_{\mathrm{ch}} < 0.05$ and $|\eta| < 2$
6. $f_{\mathrm{EM}} < 0.05$ and $|\eta| \geq 2$

A variable that is not used in the looser cuts and that can be used to validate the quality of the jets entering the analysis is the jet *timing*. This is the energy square-weighted average of the recorded time of all cells inside the jets with respect to the central detector timing, synchronised with the LHC clock and corrected by an expected offset from the time of flight. If a jet comes from beam background or a noisy cell, it is not expected to be in time with the collision. Therefore, this variable can be used as a rough check for the effectiveness of cleaning cuts. Real jets are characterised by timing which falls inside a 5 nsec window.

4.1.5 Jet calibration

While reconstruction, the jet four-momentum can be affected by several reasons, such as energy losses due to dead regions in the detector or regions in which the detector does not have good coverage. Other reasons are some cells in which the energy of particles was deposited but they are left out of the reconstructed cone, and the reading in some cells can be smaller than the noise thresholds and thus will not be accounted for. Also, hadrons in jets deposit only part of their energy in the detector, and so the energy should be corrected. To account for all these effects the jet four-momentum is calibrated [53, 54]. Using as an input the reconstructed jet which is at first at the EM energy scale, the calibration is done in six major steps, which will be detailed hereby:

Pileup corrections: Out of time pileup affect the `HLT` trigger jets, and is dependent on the position of the bunch from which the event has occurred inside the bunch train, and thus on the duration of the bunch train. This effect can be corrected by applying energy offset correction to the LAr cells depending on the location of the bunch in the bunch train and on $\langle\mu\rangle$. In-time pileup is causing additional energy deposition which can be accounted for using the following additional corrections:

1. Subtraction of the pileup energy on an event-by-event basis, based on the product of the jet area and the pileup energy density in the specific event. The jet area is calculated during reconstruction, where many artificial particles with very small p_{T}, called *ghost* particles are uniformly added to the event before the jets are reclustered. The active jet area of a jet is the area in the $\phi-\eta$ plane, in which ghosts added are clustered into the jet. A jet area four momentum of a jet, A, is the sum over all four momenta of the ghost particles divided by the transverse momentum density of the ghosts. The pileup energy density is calculated in a full calorimeter scan while clustering all possible jets using the soft radiation sensitive $\mathrm{k_T}$ clustering algorithm, as the median of $p_{\mathrm{T}}^{\mathrm{jet}}/A^{\mathrm{jet}}$ of all jets with $|\eta| < 2$ in an event [55].
2. Residual pileup correction [56], based on MC simulation, is a function of $\langle\mu\rangle$ and

NPV. In a given pseudo-rapidity region, a truth jet energy taken from simulation is compared to its associated reconstructed energy. The difference between the two energies is investigated concerning its dependence on $\langle\mu\rangle$ for a given value of NPV, and its dependence on NPV for a given range in $\langle\mu\rangle$. Both dependencies are fitted to a linear functions. Using these functions, a correction is then applied to jets from data, depending on $\langle\mu\rangle$, NPV and pseudo-rapidity of the jet.

Origin correction: Based on the location of the primary vertex, the origin correction changes the jet coordinates to point to the primary vertex rather than to the centre of the detector. This correction changes only the jet direction and not its energy.

Jet Energy Scale (JES): Usually referred to as EM+JES calibration scheme, it is a MC based calibration aimed to calibrate the jet energy and get it into the hadronic energy scale. The energy response is defined as $E^{\mathrm{reco}}_{\mathrm{jet}}/E^{\mathrm{truth}}_{\mathrm{jet}}$, where $E^{\mathrm{reco}}_{\mathrm{jet}}$ is the reconstructed jet energy and $E^{\mathrm{truth}}_{\mathrm{jet}}$ is the truth jet energy. In each bin of energy and pseudo-rapidity, the response distribution is fitted to a Gaussian. The means of all the gaussians in specific pseudo-rapidity regions is drawn against the energy in the centre of the bin. A calibration curve is then established for each pseudo-rapidity region using a fitted function. This curve is then used to obtain a value, $\mathcal{F}_{\mathrm{calib}}(E^{\mathrm{reco}}_{\mathrm{jet}}, \eta^{\mathrm{reco}}_{\mathrm{jet}})$ to multiply each measured jet's energy.

Global Sequential Calibration (GSC): This is a MC based calibration additional to the EM+JES calibration using the following additional variables from the calorimeter, inner detector and muon spectrometer [57]:

- Fraction of energies deposited in various layers of the calorimeters. Large fractions in specific layer indicate a jet falling in a coverage hole in the detector.
- Number of tracks with $p_{\mathrm{T}} > 1$ GeV, and the tracking jet width, which is the p_{T}-weighted mean of the tracks ΔR to the jet axis as measured in the calorimeter. The track based variables have shown to reduce the difference in response between light quark and gluon jets.
- Number of muon segments behind the jet in the muon chambers. This accounts for the energy leakage beyond the hadronic calorimeter efffect.

As in the EM+JES, the mean of the distribution of the response between the reconstructed jet energy and the associated truth jet energy in bins of p_{T} and η is parametrised. In the GSC the parametrisation is done as a function of one of the variables from the list above. A correction is then applied to the jet energy by the variable providing the largest improvement in each bin. This procedure is then repeated for all other variables.

η-intercalibration: The calorimeter response differences in data and Monte Carlo simulation are corrected by using a dijet balance technique. The jet response in the forward region relative to central jets can be studied as a function of jet pseudorapidity and transverse momentum. The relative response is compared in data and Monte Carlo simulation. The data/MC response ratio is used to correct the jet energy scale in data, so that it accounts for effects not initially included in the MC used to derive the JES calibration. The technique and the analysis code employed for trigger jets are described in [58].

Residual in-situ calibration: The next step is based on additional corrections obtained from events containing just one jet and a Z boson decaying to a lepton pair or a photon. These corrections are used for the central region. Similar corrections based on events with dijet are used for the forward region and events with multijets are used for higher p_{T}. This data driven calibration aims to correct the jet energy scale in data for residual effects not treated properly by the MC based EM+JES calibration [59]. Relying on the fact that the response of leptons, photons and even jets in some parts of the detector is well understood, they can be taken as reference and from p_{T} conservation, it is possible to study the response of the recoiling probe jet using the asymmetry parameter defined as:

$$\mathcal{A} = \frac{p_{\mathrm{T}}^{\mathrm{probe}} - p_{\mathrm{T}}^{\mathrm{ref}}}{p_{\mathrm{T}}^{\mathrm{avg}}} \tag{4.9}$$

Here $p_{\mathrm{T}}^{\mathrm{ref}}$ refers to the reference object (Z, photon or jet in a well-calibrated region), $p_{\mathrm{T}}^{\mathrm{probe}}$ refers to a jet in need of additional calibration, and $p_{\mathrm{T}}^{\mathrm{avg}}$ is their average. Due to the dijets events topology, this asymmetry is expected to arise only from the difference in response in the calorimeter regions. For any given bin of $p_{\mathrm{T}}^{\mathrm{avg}}$ and η, the response can be thus defined as

$$\frac{1}{c} = \frac{p_{\mathrm{T}}^{\mathrm{probe}}}{p_{\mathrm{T}}^{\mathrm{ref}}} = \frac{2 + \langle \mathcal{A} \rangle}{2 - \langle \mathcal{A} \rangle} \tag{4.10}$$

where $\langle \mathcal{A} \rangle$ is the average of the asymmetry in that bin. The reference regions were chosen across the detector, and the response of a given region is mesured with respect to all these reference regions. The calorimeter response to the central region, where $|\eta| < 0.8$ is then calculated by solving a set of linear equations. The resolution of the asymmetry can be calculated as:

$$\sigma(\mathcal{A}) = \frac{\sqrt{\sigma(p_{\mathrm{T}}^{\mathrm{ref}})^2 + \sigma(p_{\mathrm{T}}^{\mathrm{probe}})^2}}{p_{\mathrm{T}}^{\mathrm{avg}}} \tag{4.11}$$

Statistical uncertainties are calculated using pseudo-experients. In events where the leading jet is back to back with many lower-p_{T} jets, which can be named together as a recoil system, the multi-jet balance is defined as: $R_{\mathrm{MJB}} = p_{\mathrm{T}}^{\mathrm{leading}}/p_{\mathrm{T}}^{\mathrm{recoil}}$, where $p_{\mathrm{T}}^{\mathrm{recoil}}$ is the magnitude of the vector sum of all $\vec{p}_{\mathrm{T}}$ of the jets in the recoil system. This method is able to extend the range of the jet calibration beyond the limit of the boson+jet which is around 800 GeV.

JES uncertainty The JES uncertainty is determined for jets with $p_{\mathrm{T}} > 15$ GeV and $|\eta| < 4.5$. JES uncertainties are described by 58 nuisance parameters[1], as well as uncertainties due to pileup, jet flavour, and jet topology that add five additional nuisance parameters [60]. For high p_{T} dijet measurements, the 58 nuisance parameters can be reduced to only a few, depending on the specific analysis, as seen for example in section 8.4 of Ref [60].

4.1.6 Event preselection

Jets are reconstructed using the anti-k_{T} clustering algorithm [47] with a distance parameter of $R = 0.6$, starting from topological energy clusters in the calorimeters [49]. Jets are calibrated following the procedure described in section 4.1.5. This is the case for both the offline jets used for the regular analyses and for the trigger jets used in the TLA.

Whether using the invariant mass or the angular distribution, each dijet analysis is aiming to use only events with at least two high transverse energy (E_{T}) jets which are representing a quark or a gluon coming from the main vertex of a pp interaction. Each search approach will have a finer selection to suite its purpose and will be describe in the relevant sections below. The preselection cuts on the events considered for the analyses consists of:

1. The event had to be triggered by a chosen trigger. The specific trigger chain which is used in each approach will be mentioned in the relevant section.
2. The event had to be taken while the calorimeters were performing well. This requirement is considered satisfied when the event is coming from a run listed in the Good Run List (GRL), meaning that it was taken during a period with an LHC stable beam operation mode, and the detector was operating properly including all the subdetectors and triggers relevant to the analysis.
3. The event had to be taken during a period in which there were no LAr noise bursts, the data taken was not found to be corrupted, there was no missing data from unmasked cells and no missing readout in significant number of channels.

[1] free parameters that are not of direct interest for the analysis.

4.2 Dijet Angular Analysis

4.2.1 Introduction

The angular distribution of the outgoing two leading jets can help in a potential discovery of NP, complementary to to the mass resonance search. In case of a discovery in the invariant mass spectra the angular distribution can help in understanding its properties. Since the QCD background to the mass resonance search in not well modelled and a data driven background estimation is used, where the data distribution is fitted to a smooth function, a very wide excess or a an excess at the tail of the distribution will be fitted along with the background and thus the `BumpHunter` algorithm will not be able to discover it.

The key idea of the angular analysis is that in the QCD background, the dominant jet production is through t-channel processes, which will result in small scattering angles and thus an enhancement of forward jets. In case of the production of a new particle [61, 62], or entering the energetic realm where a new force of nature becomes manifested [63, 64], most models predict that the dijet production will be more isotropic.

The angular behaviour of the two leading jets can be described by the angle between them, represented by the variable:

$$\chi = e^{2|y^*|} \tag{4.12}$$

where $y^* = \frac{1}{2}(y_1 - y_2)$, and y_1, y_2 are the rapidities of the leading and subleading jets in p_{T}. As described in sec 1.2.1, the difference between the two rapidities and so also y^* and χ are invariant under a boost along the z direction. These variables are also relevant to the rest frame of a the mediator particle, and thus sensitive to its spin. In case the sum of the dijet p_{T} equals to zero, the two jets rapidities can be written as $y_{1/2} = \pm y^* + y_B$, where $y_B = \frac{1}{2}(y_1 + y_2)$. In the centre of mass frame the jets are back to back, and so their rapidities should be equal to $\pm y^*$ and y_B is then the rapidity boost of the dijet system with respect to the pp collision frame of reference. A schematic representation of the rapidities of the two jets in shown in figure 4.4.

At leading order, the QCD $2 \to 2$ scattering process is dominated by the t-channel. One can calculate the differential cross section with respect to the variable χ. In first principle, the differential cross section $d\sigma/d\Omega \propto d\sigma/d\cos\theta$ is proportional to the squared amplitude of the process, and the amplitude behaves like the mediator propagator which is $1/q^2$ where q^2 is the transferred momentum by the mediator. For a t-channel process $q^2 = t = (p_i - p_f)^2 \cong -2p^2(1-\cos\theta^*)$, where, $p_{i(f)}$ are the initial (final) 4-momenta of one of the interacting partons and $p(\theta^*)$ is the magnitude of the 3-momentum (scattering angle) of the partons in the di-parton rest-frame. Since the outgoing partons cannot be distinguished, we take $\cos\theta^* \geq 0$.

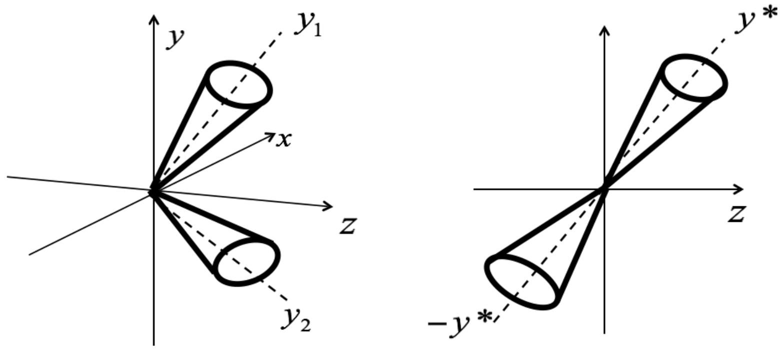

Figure 4.4: The left (right) plot shows a schematic layout of two jet configuration and their rapidities in the lab (the centre of mass of the dijet system) reference frame.

The variable χ can be expressed using θ^* by the relation:

$$\chi = \exp(2|y^*|) = \frac{1+\cos\theta^*}{1-\cos\theta^*} \tag{4.13}$$

leading to the relation:

$$\frac{d\sigma}{d\chi} = \frac{d\sigma}{d\cos\theta^*}\frac{1}{\frac{d\chi}{d\cos\theta^*}} \propto \frac{1}{(1-\cos\theta^*)^2}\frac{(1-\cos\theta^*)^2}{2} \propto \text{const} \tag{4.14}$$

In contrary to this background, a NP signal will often be characterised by peak at low values of χ. The analysis relies on the ability to discern such deviations from the QCD prediction. The sensitivity is increased with a combination of rapidity cuts, where the first option is to enhance isotropic (and suppress t-channel) production by setting a maximum limit on $|y^*|$. Since the distributions of interest are binned in χ which has a one-to-one correspondence with this variable, this cut plays a minor role. The option of a maximum limit on $|y_B|$, on the other hand, reduces the range of the Parton Distribution Function (PDF) probed, and thus enhances the sensitivity to the partonic cross section. To identify the appearance of new phenomena in the angular distributions, data are compared to the SM expectation as modelled by MC of QCD events. The analysis strategy and selection cuts are verified using MC and a partial data set corresponding to a randomised selection of a quarter of the available collision data. This study, and its results published in [8] are based on pp collisions at a center-of-mass energy of $\sqrt{s} = 8$ TeV, recorded during 2012 with integrated luminosity of 17.3 fb^{-1}. In addition, the analysis was "blinded" by not constructing the distributions in data for the region $m_{\text{jj}} > 2$ TeV while the search strategy was being optimised. This is motivated by the assumption that no deviations from the SM are expected below this dijet invariant mass value, which is inferred from previously published limits on a variety of processes beyond the Standard Model [7]. Using only a quarter of the data set ensures that we are not superseding the amount of data used for the previous search using dijet angular distributions, corresponding to 4.8 fb^{-1} at $\sqrt{s} = 7$ TeV [40].

Previous analyses [42] showed that the low range of χ, $\chi < 3.32$, corresponding to $|y^*| < 0.6$ is expected to be most sensitive to new physics. This leads to the introduction of a new variable F_χ [25] in order to measure the centrality of events. This variable is the fraction of events with dijet produced centrally and the total number of dijet event for a certain m_{jj} region:

$$F_\chi(m_{\mathrm{jj}}) = \frac{N_{\mathrm{events}}(|y^*| < 0.6)}{N_{\mathrm{events}}(|y^*| < 1.7)} \tag{4.15}$$

For a given amount of data, the F_χ variable can be binned more finely in m_{jj}, given an added value to the χ distribution when looking for a specific model. As the QCD background to the NP signal can be estimated only using MC with large theoretical uncertainties, using the F_χ variable has another advantage, as these uncertainties in the numerator and denominator will be substantially reduced. In case any hints for deviation from the SM are seen in the χ distribution, it can be most useful to look also at the F_χ distribution to better locate the region of deviation in m_{jj}.

Previous dijet angular analyses at the LHC at centre-of-mass energy $\sqrt{s} = 7$ TeV [24,40], as well as the recently public analysis at $\sqrt{s} = 8$ TeV from CMS [65], have all been in agreement with the Standard Model. This study [8] builds from the dijet mass resonance search [7] published by ATLAS, with only a few selection cuts differing. It will be detailed in the following. The datasets and MC samples used in the analysis and the event selection applied for them will be detailed in sections 4.2.2 and 4.2.3, respectively. A validation study for the MC samples is given in section 4.2.4, and the correction for the QCD predictions are detailed in section 4.2.5. The simulation and corrections needed for signal model are described in section 4.2.6. Section 4.2.7 shows the systematic uncertainties and finally section 4.2.8 gives the analysis results.

After the analysis was finalised, it was repeated for the 13 TeV run, and results were published along with the resonance search in [10]. As my contribution for this analysis was mostly repeating the work I have done for the 8 TeV analysis, and the main focus of my work has moved to the TLA, I shall only quote the 13 TeV results without getting into details in section 4.2.8.

4.2.2 Datasets and MC samples

The data used in the analysis correspond to a total integrated luminosity of 17.3 fb^{-1}.

To predict the background, MC simulations of QCD dijet processes were used. These are generated using the event generator `Pythia8.160` [66] with the `AU2` underlying event tune [67] and the `CT10` PDF [68]. The simulated events are propagated through the ATLAS detector simulation using `Geant4` [36], and the same jet finding algorithm, calibration and event selection procedure is applied to MC as to data. The pertubative hard scattering process in `Pythia8` is calculated to Leading Order (LO). To take corrections from higher order perturbative calculations into account, Next to Leading Order (NLO) hard scatter processes are generated using `NLOJET++` [69, 70]. From the comparison of the m_{jj} distributions of the events generated by the different generators at both LO and NLO, k-factors are obtained, which are bin-by-bin scale factors that can be applied to the full `Pythia` prediction and bring it (closer) to NLO accuracy. The procedure is further described in section 4.2.5. Finally, electroweak Sudakov corrections [71] are applied to the MC prediction, as further described in Sec. 4.2.5.

For evaluation of the systematic uncertainty due to the choice of generator, and for the validation of the k-factors, samples produced using the NLO matrix element generator `Powheg` [72, 73] and showered with either `Pythia` or `Herwig+Jimmy` [74–78] are used.

The benchmark signal considered in this analysis is a quark contact interaction, described in section 4.1.1. It is characterised by a compositeness scale Λ and its interference mode with the QCD process $q\bar{q} \to q\bar{q}$. Signal and QCD are simultaneously modelled in `Pythia`, taking interference into account, using the same tune and PDF set as for QCD MC. All details on the signal generation can be found in Sec. 4.2.6.

4.2.3 Event selection

Following the preselection described in section 4.1.6 an event is required to have at least one vertex associated with more than one track. This cut is aimed to eliminate events coming from cosmic radiation rather then a pp interaction.

The trigger selection for the angular analysis uses a collection of single jet triggers. The lowest unprescaled single jet trigger in p_{T} used in the collection of the 2012 data sample was the `HLT` trigger `j220`, requiring the event to have one $R = 1.0$ jet with $E_{\mathrm{T}} > 220$ GeV. When producing a trigger turn-on curve as a function of the leading offline reconstructed $R = 0.6$ jet in the event, as used in this analysis, this thresholds corresponds to accepting events with a leading jet p_T above 333 GeV corresponding to a trigger efficiency above 99.5%. From kinematical constraints, this p_{T} cut restricts the events to dijet masses greater than 1.8 TeV. To access lower masses, single-jet triggers with lower jet p_{T} thresholds must be used. Since these triggers have large rates during data taking, they have been prescaled. To further increase the number of events the *delayed stream* was used. The addition of those data yields a significant increase in statistics for dijet masses between 600 and 1000 GeV.

Due to the steeply falling p_{T} spectra in QCD, and in order to cover this large range in single-jet p_{T} needed for the current analysis, during event reconstruction each trigger is applied in a p_{T} range beginning at the point at which it is efficient, up to the corresponding p_{T} for the next higher trigger. Thus, triggers are applied individually within non-overlapping ranges of jet p_{T}. The association of each trigger within a given range of p_{T} is called the "trigger map". Since this procedure uses the p_{T} of the reconstructed leading jet in each event, it assures that each trigger is fully efficient within its range, using the p_{T} scale employed in full event analysis. Each single-jet trigger must be efficient over the p_{T} range associated with its portion of the trigger map. The efficiency of each trigger, and the p_{T} range in which it is fully efficient is calculated as explained in section 4.1.3. Table 4.1 shows the list of triggers used in the analysis.

Jet Trigger	Effective prescale	Luminosity [fb^{-1}]	99.5% p_{T} efficient [GeV]
EF_j220_a10tcem_delayed	1.0	17.32	333
EF_j180_a4tchad	192.3	9.01E-02	273
EF_j145_a4tchad	565.4	3.06E-02	241
EF_j110_a4tchad	2156.5	8.03E-03	185
EF_j80_a4tchad	9549.7	1.81E-03	135
EF_j55_a4tchad	53840.0	3.22E-04	99
EF_j35_a4tchad	462145.9	3.75E-05	59
EF_j25_a4tchad	2335358.9	7.42E-06	47

Table 4.1: Effective prescales, integrated luminosity and lower bounds of the p_{T} range in which the trigger is 99.5% efficient for each used jet trigger.

The influence of the average number of interactions $\langle\mu\rangle$ on the trigger efficiency has been studied. The sample to estimate the trigger efficiency has been divided into four subsamples, covering the whole range in $\langle\mu\rangle$. Though the trigger turn-on has a small dependence on pileup as can be seen in figures 4.5, the chosen lowest p_{T} cut gives in all subsamples trigger efficiency greater than 99.5%.

To summarise, following the preselection, the vertex and the trigger cuts, an event is accepted if it fulfils the following requirements:

1. The event consists of two jets with transverse momentum $p_{\mathrm{T}} > 50$ GeV.
2. The two leading jets are required to pass the cleaning selection criteria as described in section 4.1.4.
3. The two leading jets are required to fall within $|y| < 2.8$.
4. $|y^*| < 1.7$.
5. $|y_B| < 1.1$.

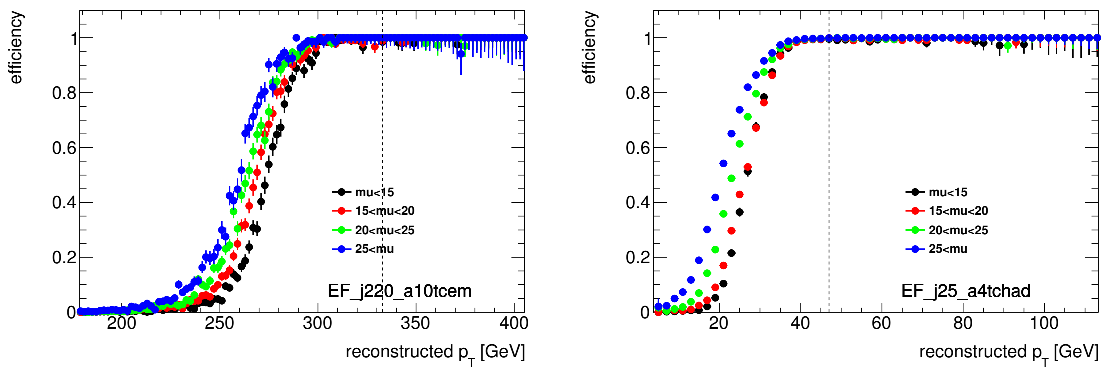

Figure 4.5: Trigger efficiencies for the single jet transverse momentum triggers for different average number of interactions . The dotted line gives the lower limit of the used p_{T} range per trigger.

6. The dijet invariant mass, m_{jj} has to be greater than 600 GeV.

The last three cuts where chosen to make sure that the event selection is unbiased due to the p_{T} and $|y|$ selection described in the first and third cuts.

Since the χ distributions are studied in various m_{jj} bins (see below), we have to avoid any bias on the m_{jj} distribution. Therefore, the efficiency with respect to m_{jj} was calculated using a similar approach as for the efficiencies in p_{T}, to show that the triggers used are fully efficient in the entire spectrum except for small inefficiency which is the impact of the lowest p_{T}-trigger, not affecting events passing the event selection. When comparing the estimated number of events lost by the use of this strategy with the statistical error in these bins, the inefficiency is found to be smaller than the statistical error by at least a factor of 10. Therefore, no systematic error has been assigned due to the trigger combination and the 99.5% efficiency points.

Binning

The binning in χ were chosen to obtain the most detailed description of the distribution while minimising bin migration effects. As described in section 3.2.3 the calorimeter granularity in y is defined by the cell widths, approximated as 0.1. To avoid bin migration due this granularity, bin boundaries of any rapidity distribution should be an integer multiple of 0.1 and bin boundaries of the χ distribution should be an exponent of that integer multiple of 0.1. A study conducted in [79] has shown that bin boundaries choice of $\chi_n = e^{(0.3\times n)}$ minimises the bin migration to a negligible effect. The angular range $|y^*| < 1.7$, corresponds to $\chi < 30$, and so this interval is divided into 11 bins with the last bin extended to $\chi = 30$.

The data is further binned coarsely in m_{jj} (0.6, 0.8, 1.2, 1.6, 2.0, 2.6, 3.2, 8.0 TeV) with the expectation that low-mjj bins are dominated by QCD processes and that signals associated with new physics would be found in higher dijet invariant mass bins. The m_{jj} bin boundaries are chosen to optimise the expected sensitivity to the model of contact interactions. The highest dijet mass observed is 5.5 TeV.

4.2.4 Validation of the QCD prediction

While in the mass resonance search, the background estimation is obtained through a fit of the data to a smooth function, the angular distribution analysis requires a full MC estimation for the QCD background. The background estimation uses a NLO QCD calculation (matrix element only) which needs to be corrected for non-perturbative and detector effects, in order to be compared to data. To study the validity of the LO QCD calculations, different versions of the `Pythia` LO + parton shower MC generators have been used. In the previous analyses [25] events were generated using `Pythia6.421` [29], which was in reasonable agreement with ATLAS data [80]. In the present analysis [6, 81], we use `Pythia8.170` [66].

There is a difference between the kinematic distributions generated by the two `Pythia` versions. The difference exists already at parton level, but gets significantly larger at small p_{T} values, when adding hadronization, ISR, final state radiation and multiple partonic interaction etc.

In order to understand the differences between the two generator versions, we have generated different QCD samples with centre of mass energy, $\sqrt{s} = 8$ TeV. The samples were generated in different slices of the outgoing parton transverse momentum, p_T, (JX slicing) to account for the rapidly falling jet p_{T} spectrum and obtain enough statistics for all the p_{T} range. Each slice consists of 1M events. Events from each slice were assigned with a weight due to the average cross-section of the slice and its generated number of events, and normalized to a luminosity of 1 nb^{-1}. We have used `Pythia6.423` with the `AUET2B` [82] tune and the `CT10` PDF, and `Pythia8.170` with the `AU2` tune and the `CT10` PDF.

The strong coupling constant definition follows the LO evolution as in equation 1.3, setting n_{f} to five, and the transferred momentum calculated as $Q^2 = p_{\text{T}}^2 + \frac{m_3^2+m_4^2}{2}$, where m_3 and m_4 are the masses of the outgoing partons. These definitions holds for both versions. Note that, in order to compare distributions with similar values of the strong coupling constant one can set the value of Λ_{QCD} in `Pythia6`, whereas in `Pythia8` one can only set the value of Q^2 and the default value is set to $\alpha_s(M_Z) = 0.1265$, meaning $\Lambda_{\text{QCD}} = 0.14$ GeV. A comparison between the `Pythia` versions: `8.160` and `8.170` showed that they are in good agreement.

A Rivet [83] code was used to analyze all samples, in which events with $p_{\text{T1}}, p_{\text{T2}} > 25$

GeV, $|\eta_1|, |\eta_2| < 2.8$ and $|y^*| < 1.7$, were chosen. Jets reconstructed with anti-k_T6 [46, 47] were used, and only the two leading p_{T} jets in an event were taken into account.

As a first step, the kinematic distributions of the $2 \to 2$ process at the parton level generated by the two versions of `Pythia`, were compared. This comparison has shown a constant relative difference at the p_{T} distribution of about 5% in favor of `Pythia8`, implying that the `Pythia8` generated events have larger cross-section in all p_{T} slices, than those of `Pythia6`. When looking at the m_{jj} distribution this difference is mainly for $m_{\mathrm{jj}} < 1$ TeV. When specifying the value of Λ_{QCD} to be 0.08772 GeV in `Pythia6`, there is not much difference, and when specifying the value of $\alpha_s(M_Z)$ in `Pythia8` to be 0.11798 corresponding to that Λ_{QCD} value, its cross-section becomes significantly smaller (by 20%). Figure 4.6 shows the invariant mass, transverse momentum and rapidity distributions of the two leading jets for generated events using `Pythia6` and `Pythia8` at the parton level with and without modifying the value of the strong coupling constant.

We have tried to look for reasons for this difference at the parton level - different PDFs, turning off central diffraction, but to no avail, none of these made any difference. As can be seen in figure 4.6, there is almost no difference between the `Pythia6` distributions with and without setting a value for α_s, and the difference between `Pythia6` and `Pythia8` without setting a value to α_s, at $p_{\mathrm{T}} < 1$ TeV, is roughly constant and is in the order of 5%. We did not yet find an explanation for the smaller cross-section of the samples generated with `Pythia8` when setting the value for α_s.

As a second step, we have looked at the different kinematic distributions of samples generated by both `Pythia` versions using the same `CT10` PDF, and different tunes. Table 4.2 summarises the various generator options, and figure 4.7 shows the comparison between their kinematic variables distributions. Note, that since the analysis is making use of a normalised χ distribution, a constant shift alone in such distribution will not affect it. The choice of generator, tune and shower is leading to a systematic uncertainty which will be described in section 4.2.7.

4.2.5 Corrections for the QCD predictions

Study of k-factors on χ distributions

`Pythia` is a complete event generator calculating hard scattering processes to LO only. Some of the missing higher order processes are partially made up for in the showering and other non-perturbative processes. As NLO perturbative calculations are more precise, the cross section can be corrected to NLO by applying bin-wise k-factors, which account for NLO

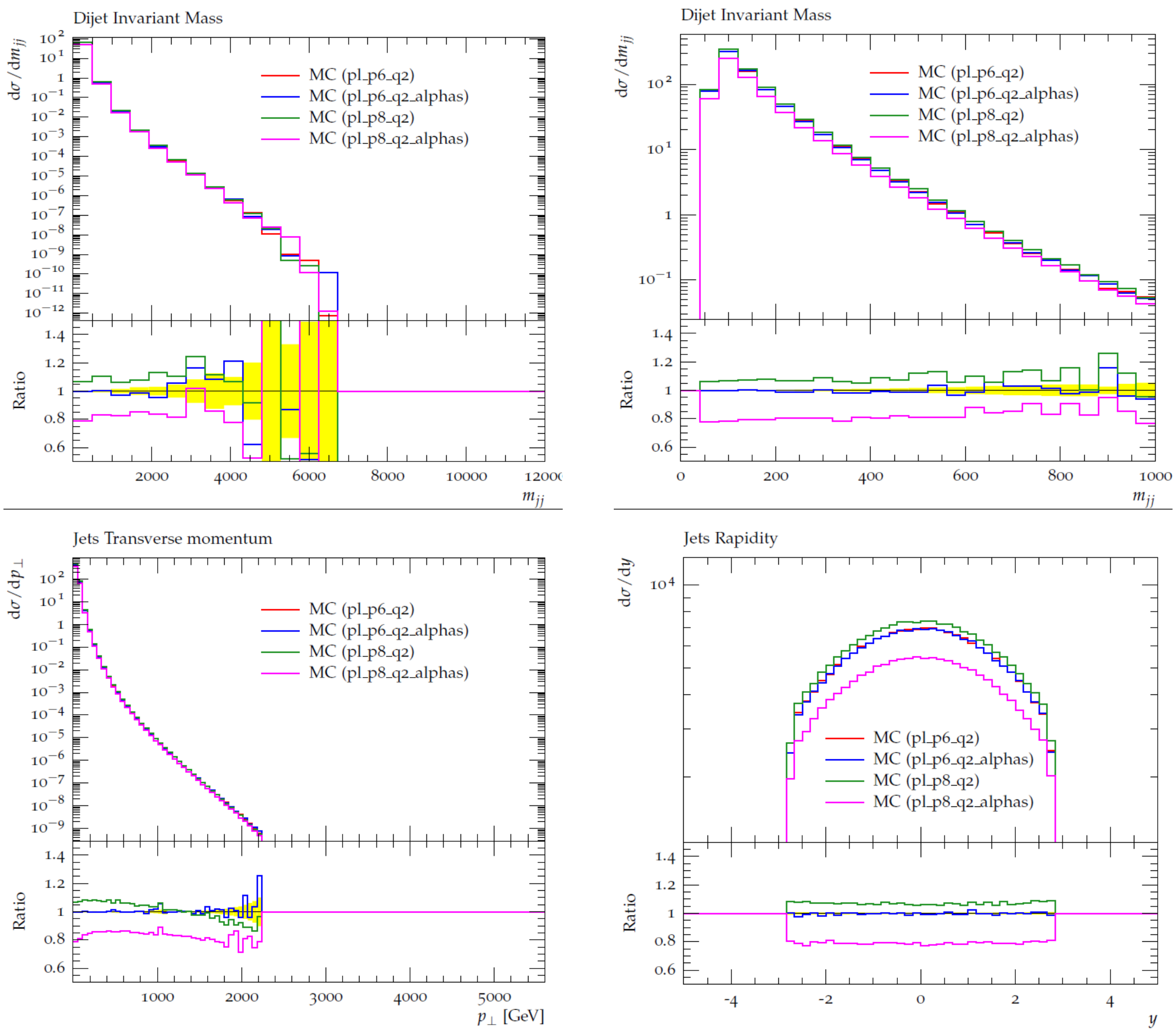

Figure 4.6: Comparison between the Pythia6 (denoted as p6) and Pythia8 (denoted as p8) at the parton level with and without modifying the value of the strong coupling constant (denoted as alphas when modified). The invariant mass is shown at the top left, and at the top right only for lower m_{jj} values. The transverse momentum and rapidities of the two leading jets, are at the bottom. The bottom panel in each plot shows the ratio between each histogram and the distribution as obtained from Pythia6 as used in previous analyses.

corrections. These corrections are derived using NLOJET, which is not a complete generator as it only calculates hard processes[2]. Since Pythia's parton showering process partially compensates for the lack of higher-order corrections, the correction can be considered as a "partial" NLO correction k_{part} which is already included in the Pythia simulation. Therefore,

[2]The settings for the NLOJET++ calculations are: PDF set 0 from CT10, $\alpha_s(M_Z) = 0.118$ with NLO precision in the running of α_s, and the renormalisation and factorisation scales, μ_R and μ_F, are both set to $p_T^{avg} = (p_T^{lead} + p_T^{sublead})/2$.

Generator option	Label
`Pythia6` `AUET2B` tune	p6_q2
`Pythia6` `AUET2B` tune, with $\alpha_s = 0.11798$ set at the hard interaction, space-like showers, time-like showers, and time-like showers from a resonance decay	p6_lambda
`Pythia6` `Perguia2011` tune	p6_Perugia2011_q2
`Pythia8` `AU2` tune	p8_q2
`Pythia8` `AU2` tune, with shower dump and spaceshower:α_s set to be the same value as in `Pythia6` following the procedure described in [84]	p8_showerDamp_q2
`Pythia8` default tune	p8_q2_defaultTune_q2
`Pythia8` `AU2` tune, with $\alpha_s = 0.11798$ set at the hard interaction, space-like showers, time-like showers, and multi-parton interaction	p8_allAlphaS_q2

Table 4.2: Various samples generated by using different versions and option of the `Pythia` generator, and their labels.

in the procedure to apply NLO corrections, care must be taken to handle the non-perturbative contributions in `Pythia` correctly. For this a dedicated `Pythia` sample with only hard process and parton showering turned on, $\mathrm{LO}_{\mathrm{show}}^{\mathtt{Pythia}}$, is used. One can then derive a correction as

$$\mathtt{Pythia}_{\mathrm{corr}} = \frac{(\mathrm{NLO}/\mathrm{LO})^{\mathtt{NLOJET}}}{(\mathrm{LO}_{\mathrm{show}}/\mathrm{LO})^{\mathtt{Pythia}}} \cdot \mathtt{Pythia}_{\mathrm{reco}}, \tag{4.16}$$

where we identify $k_{\mathrm{part}} = (\mathrm{LO}_{\mathrm{show}}/\mathrm{LO})^{\mathtt{Pythia}}$ where $\mathrm{LO}^{\mathtt{Pythia}}$ corresponds to the `Pythia` LO calculation without showering and hadronization, and it is supposed to be the same as $\mathrm{LO}^{\mathtt{NLOJET}}$. Therefore, they cancel out in the ratio and we are left with:

$$\mathtt{Pythia}_{\mathrm{corr}} = \frac{\mathrm{NLO}^{\mathtt{NLOJET}}}{\mathrm{LO}_{\mathrm{show}}^{\mathtt{Pythia}}} \cdot \mathtt{Pythia}_{\mathrm{reco}} \equiv k \cdot \mathtt{Pythia}_{\mathrm{reco}} \tag{4.17}$$

The assumption that the two LO predictions are equal relies on recognising that these are the pure QCD matrix element predictions. The renormalization and factorization scales were set to be the same, thus the only thing which can introduce a difference between them might be the use of a different PDF set and α_s value in the calculations. Since both `NLOJET` and `Pythia` use the `CT10` PDF, the only difference remaining is the choice for α_s. This is indeed

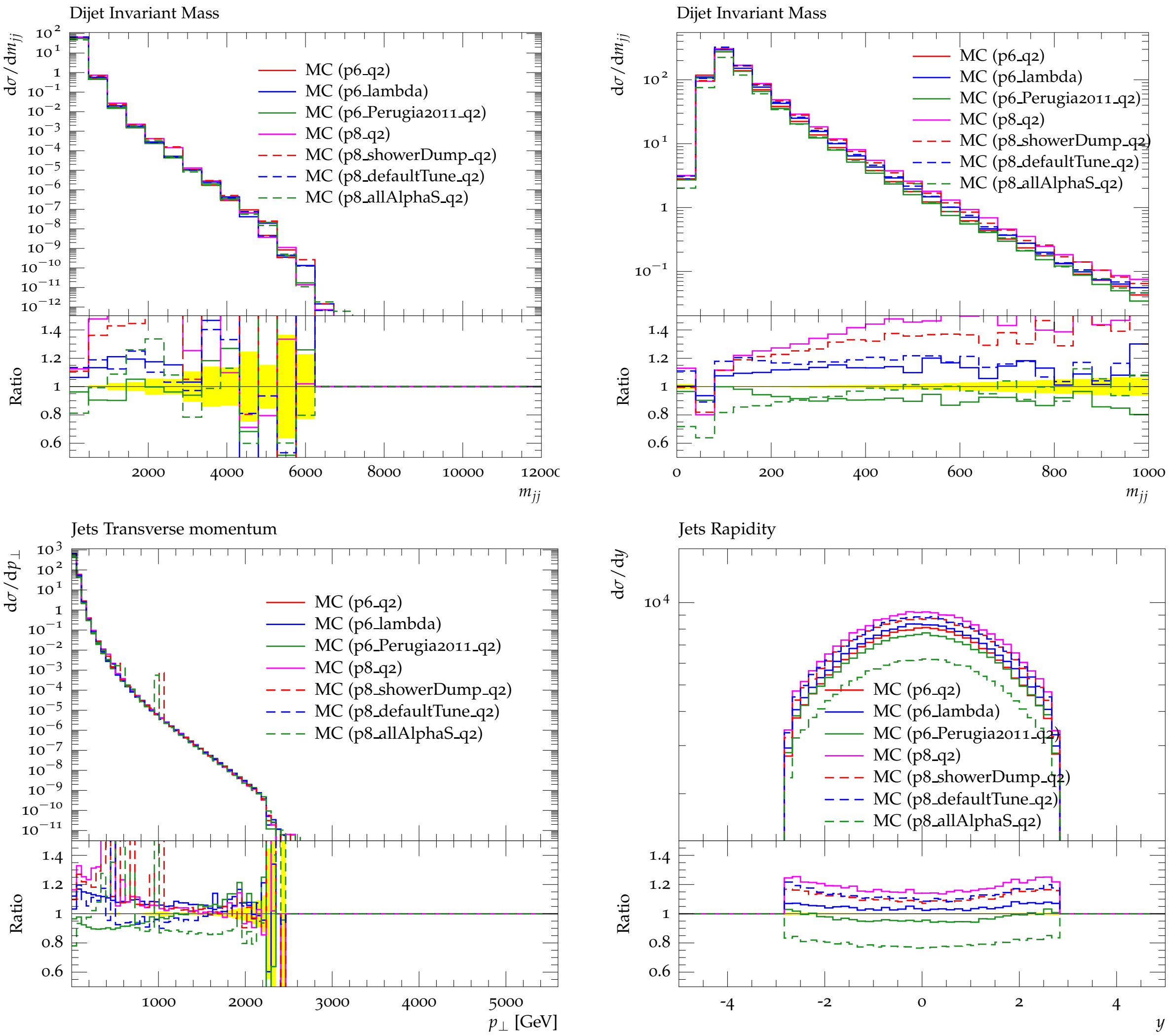

Figure 4.7: Comparison between the different tunes of `Pythia6` and `Pythia8` (see in table 4.2). The invariant mass, is shown at the top left, and at the top right only for lower m_{jj} values. The transverse momentum and pseudo-rapidities of the two leading jets, are at the bottom.

set differently in the calculations of the two generators, as they use the evolution of α_s at different order and $\alpha_s^{\texttt{NLOJET}}(M_Z) = 0.118$ whereas $\alpha_s^{\texttt{Pythia}}(M_Z) = 0.135$.

To investigate the effect introduced by the difference in α_s, all components needed to obtain the correction factor in Eq. 4.16 were generated. Figure 4.8 shows the differential cross section $d\sigma/d\chi$ in the dijet mass bin $2000 \leq m_{\rm jj} < 2600$ GeV, as predicted from the LO matrix element calculations of both generators, as well as the NLO prediction from `NLOJET` and the `Pythia` prediction where non-perturbative effects are turned off. On the right panel of that figure, the `Pythia` LO prediction has been rescaled by the square of the ratio of the two values of α_s, taken at $Q = p_{\rm T}^{\rm avg} = 350$ GeV, which is the minimum $p_{\rm T}$ required for a dijet mass in this range. The running of α_s follows equation 1.3, where the number of light flavours, n_f, is taken to be 5. The value of $\Lambda_{\rm QCD}$ is 0.2262 in NLOJET and is left floating in the Pythia case to fit the value of $\alpha_s^{\tt Pythia}(M_Z)$. The values obtained by this evolution are in agreement with those given in [85] for different values of Q.

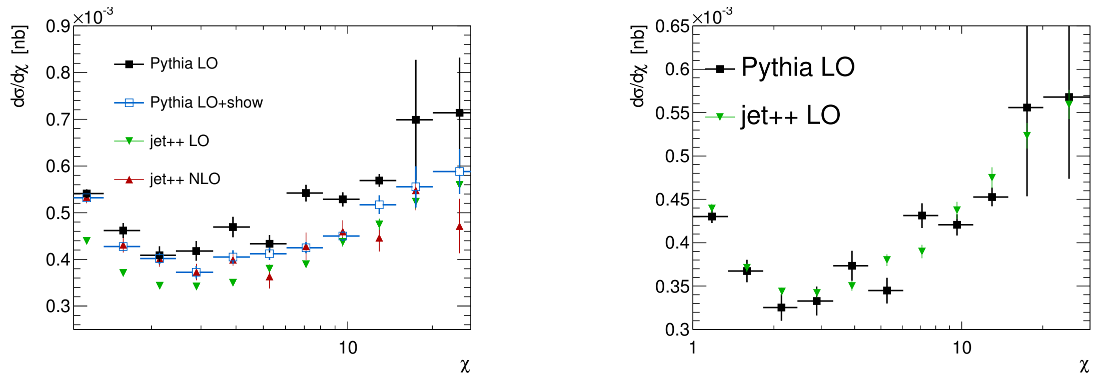

Figure 4.8: Predicted differential cross section $d\sigma/d\chi$ in the dijet mass bin $2000 \leq m_{\rm jj} < 2600$ GeV, using different α_s on the left and rescaling the Pythia prediction to match the α_s value used in NLOJET on the right.

It is clear from figure 4.8 that the difference between the two LO predictions is introduced solely from the difference in α_s, as it vanishes once the rescaling of Pythia LO is done. It is also clear, that this difference merely introduces a shift in the normalisation between the two predictions. As this analysis uses distributions normalised to unit area, the difference introduced by the different default α_s values vanishes, and one can safely ignore the LO predictions in the k-factor expression and use equation 4.18 for the k-factor at each χ value.

$$k(\chi, m_{\rm jj}) = \frac{{\rm NLO}^{\tt NLOJET}(\chi, {\rm m_{jj}})}{{\rm LO}^{\tt Pythia}_{\rm show}(\chi, {\rm m_{jj}})} \tag{4.18}$$

It is also evident in figure 4.8 that the parton showering process in Pythia affects the shape of the χ distribution in a similar way as the addition of higher orders, but does not give the full effect. Comparing the shapes, we can expect k-factors with only a small dependence on χ. Figure 4.9 shows the χ dependence of the k-factors for all dijet mass bins, with statistical errors included. The statistical fluctuations of the k-factors have been reduced by a smoothing procedure[3] which brings outliers closer to the overall trend using medians of sequences. The edge points and error bars are unaffected. The shift of points introduced by the smoothing is well within the statistical uncertainty for all points, but indeed results in a smoother behaviour. The k-factor statistical uncertainty is taken as a

[3]The ROOT method `TH1::Smooth()` is used, which employs the 353QH smoothing algorithm, using the repeated median of intervals (3, 5, 3 bins wide) and also includes the smoothed residuals [86].

systematic uncertainty for the analysis and is included in plots 4.9. The k-factors are applied to the default LO `Pythia` sample with hard process, parton showering, multiple interactions, and nonperturbative effects turned on. Both `Pythia` samples use the `CT10` PDF and `AU2` tune. The result is a NLO parton sample that has been corrected with non-perturbative effects. These k-factors are applied to each bin in the χ distributions before normalisation.

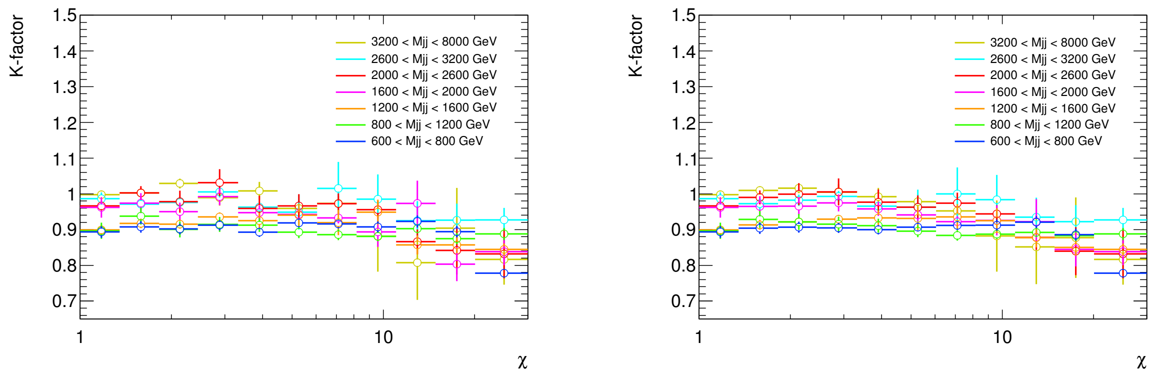

Figure 4.9: The left (right) plot show the k-factors dependence on χ for all dijet mass bins before (after) smoothing.

Finally, the prediction from `Pythia` with k-factors applied is compared to a `Powheg` prediction of the angular distributions of QCD, with the `A14 NNPDFLO` tune and the `CT10` PDF set. `Powheg` generates the three leading partons to NLO accuracy and is then interfaced to `Pythia` for showering. The `Powheg` sample serves only as a reference of what the NLO prediction would be and not used as the default QCD prediction for two reasons. First, the signal prediction is obtained with `Pythia`, and this signal has interference with QCD, which means having the same QCD prediction in both background and signal modelling is benificial (see section 4.2.6 for more details). Second, the `Powheg` sample is smaller which introduces large statistical fluctuations, particularly at high m_{jj}. Figure 4.10 shows the comparison of the `Powheg` and `Pythia` $\times$ k-factors predictions at reconstructed level, for two example bins in m_{jj}. The ratio of the two is consistent with 1 within errors for all bins. The normalisation is somewhat driven by the last bin in χ, which is the widest, sometimes introducing large shifts between the predictions even though the general shape agrees. The χ distributions obtained with `Pythia` and corrected using the k-factors were found to be consistent with those obtained by `Powheg` within errors. The differences between the two generators were taken as one of the theoretical uncertainties as will be described in section 4.2.7.

Electroweak corrections on χ distributions

As the transferred momentum scale Q in the scattering increases, the relative contribution from diagrams including (massive) weak gauge bosons gets larger (at leading order the en-

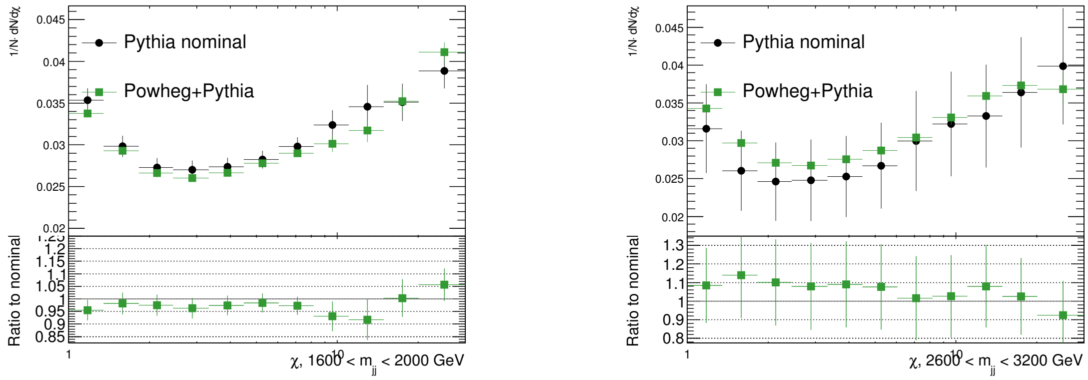

Figure 4.10: Comparison of the differential cross section $d\sigma/d\chi$ (normalised to unit area) predicted by `Powheg` to `Pythia` with k-factors, in the dijet mass bin $1600 \leq m_{\mathrm{jj}} < 2000$ GeV on the left and $2600 \leq m_{\mathrm{jj}} < 3200$ GeV on the right

hancement goes like $\alpha_{\mathrm{w}} \cdot \ln(Q^2/M_W^2))$. These processes are not present in the NLO QCD calculation. To correct for this, we use correction factors $\kappa(\chi, m_{\mathrm{jj}})$ provided by the authors of Ref. [71]. They consist of both tree level, $\mathcal{O}(\alpha_s\alpha, \alpha^2)$, and weak loop, $\mathcal{O}(\alpha_s^2\alpha)$, calculations. These are shown in figure 4.11. The effect is most pronounced at high m_{jj} and low χ, and the correction factors range from unity at low m_{jj} to $0.98 - 1.12$ in the highest m_{jj} bin. Statistical uncertainties have been made negligible by running a sufficiently large sample for the MC integration. The uncertainties due to the choice of PDFs and renormalisation/factorisation scales are negligibly small, due to the cancellation occurring in the ratio giving the correction factor.

The fully corrected QCD prediction is thus given by

$$\texttt{Pythia}_{\mathrm{corr}}(\chi, m_{\mathrm{jj}}) = k(\chi, m_{\mathrm{jj}}) \cdot \kappa(\chi, m_{\mathrm{jj}}) \cdot \texttt{Pythia}_{\mathrm{reco}}(\chi, m_{\mathrm{jj}}), \qquad (4.19)$$

where both k- and κ-factors are applied before normalisation.

4.2.6 Signal simulation

Signal generation

The benchmark signal model chosen for this analysis is the manifestation of a new Contact Interaction (CI) between quarks, through an effective Fermi operator, as described in section 4.1.1. The CI is characterised by the compositeness scale Λ and the sign of the coefficient $\eta = \pm 1$ which determines the mode of interference with the QCD $q\bar{q} \to q\bar{q}$ process. Limits on constructive interference are expected to be less conservative. `Pythia` is used to generate

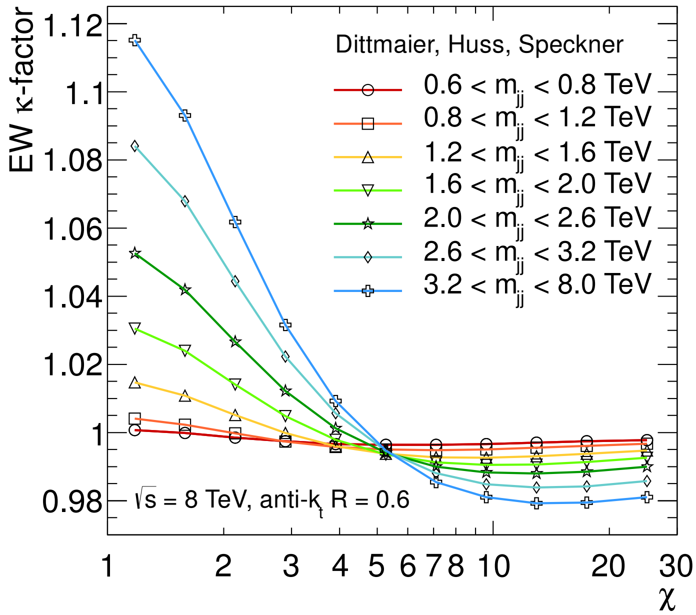

Figure 4.11: Electroweak correction κ-factor (markers) as a function of χ for all $m_{\rm jj}$ bins. Lines are not an interpolation but there to guide the eye.

MC samples with both interference modes, at $\Lambda = 7$ and 10 TeV. The same PDF set and `Pythia` tune (`AU2CT10`) is used for signal (CI) as for background (QCD) modelling. This is important, considering the interference with QCD. The χ distributions of these generated samples are shown in Figure 4.12 for various $m_{\rm jj}$ bins.

These χ distributions are then used as templates to deduce the distributions for any other value of Λ, using the observation that the interference term is proportional to $1/\Lambda^2$, and the pure CI cross section term is proportional to $1/\Lambda^4$. By adding the resulting histograms from the two interference modes at a given Λ, the interference terms cancel, and only $2\times$(QCD+CI) terms remain. Since the QCD term is known from the default MC, the CI term can be isolated. Similarly, by subtraction of the two samples, the interference term is isolated. The obtained χ distributions of CI and interference terms for $\Lambda = 7$ TeV are shown for the dijet invariant mass bin $m_{\rm jj} = [3.2, 8.0]$ TeV in Figure 4.13.

Using the dependence on Λ for the two terms respectively, full rescaling of the simulated samples can be achieved for any value of Λ. The validity of this rescaling has been tested by comparing the $\Lambda = 10$ TeV distributions obtained from the rescaled $\Lambda = 7$ TeV samples, to those from the generated $\Lambda = 10$ TeV sample. The two versions agree within their statistical errors, as shown in Figure 4.14.

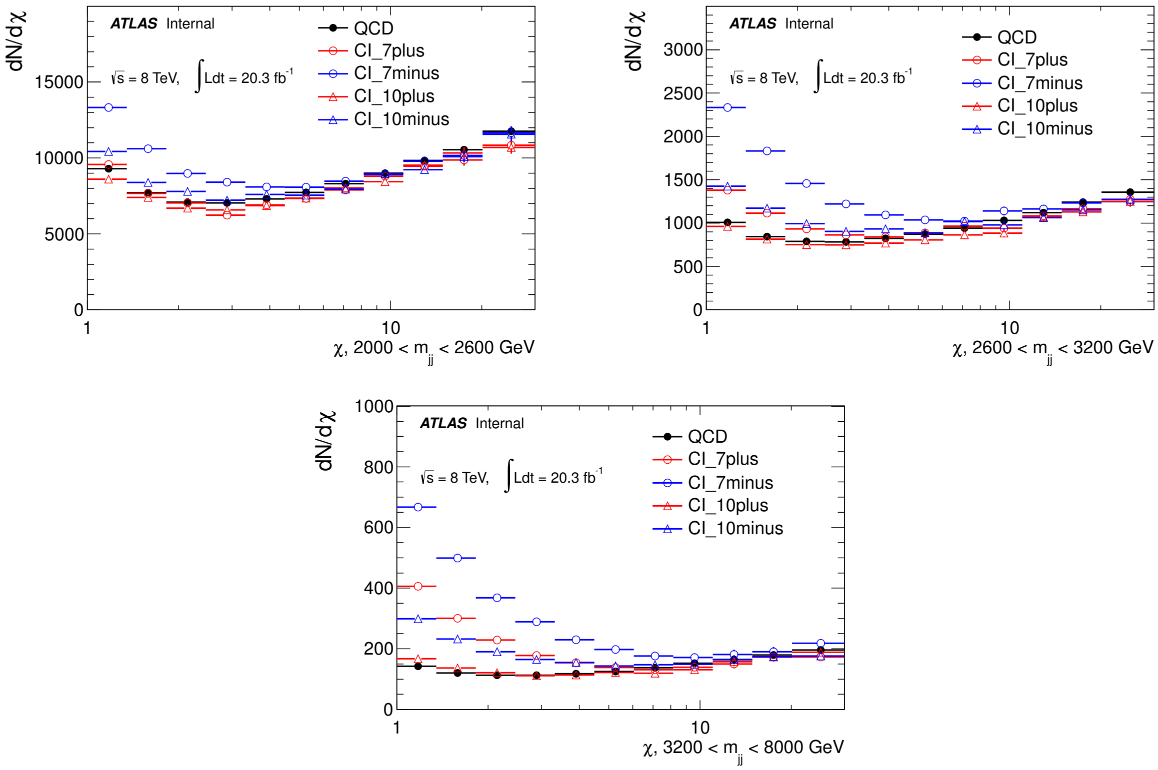

Figure 4.12: χ distributions of signal and QCD background for different dijet invariant mass ranges. The CI signals differ in the compositeness scale, $\Lambda = 7(10)$ GeV and the sign of the coefficient η: plus (minus) for destructive (instructive) interference.

Signal k-factors

As for the QCD prediction, the CI simulation is done with `Pythia`, which incorporates simulation of the interference with QCD. As `Pythia` is a LO generator, the signal as well needs k-factors to be brought to NLO precision. The LO and NLO cross section for each χ and F_χ bin are derived using the CIJET package for any value of Λ and for both interference modes [87]. Also, for the NLO correction, the interference term in the cross-section is proportional to $1/\Lambda^2$ whereas the pure CI term is proportional to $1/\Lambda^4$. By adding and subtracting the LO (NLO) interferences, one can obtain the LO (NLO) contribution of the CI term and the interference term separately for each bin. Dividing the NLO CI (interference) term by the corresponding LO contribution will give the k-factors for each bin, seperately for the pure CI and the interference terms, as shown in Figure 4.15. After applying these k-factors, we obtain the final signal contributions at various Λ scales, shown in Figure 4.16. There are no EW corrections for signal corresponding to those available for QCD.

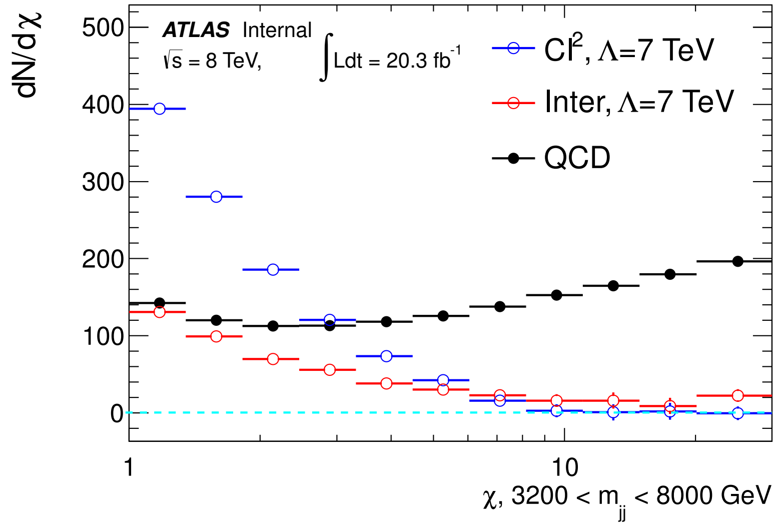

Figure 4.13: χ distributions of the signal CI and the absolute value of the interference terms for $\Lambda = 7$ TeV and $3.2 < m_{\rm jj} < 8.0$ TeV.

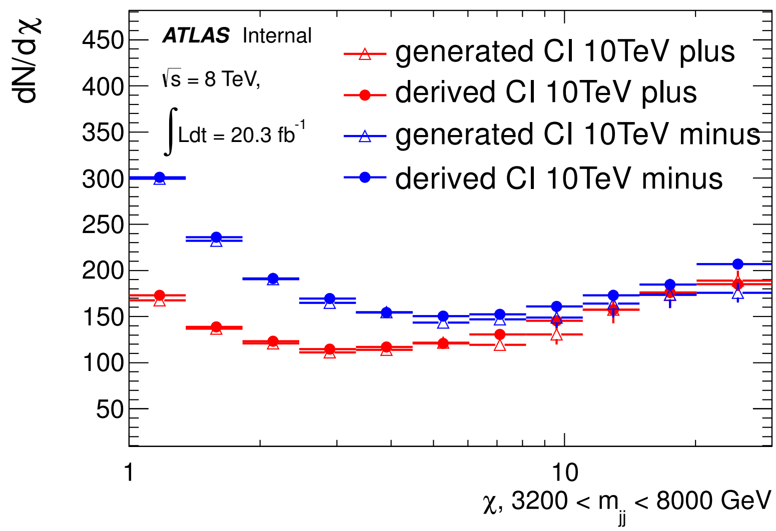

Figure 4.14: Comparison between generated and derived signal distributions for $\Lambda = 10$ TeV.

4.2.7 Systematic uncertainties

Since the χ distribution is normalized, many uncertainties cancel. The main remaining experimental uncertainties expected in this measurement are the Jet Energy Scale (JES) and the uncertainties on the beam energy. The main theoretical uncertainty comes from the generator and the factorisation and renormalisation scale uncertainties.

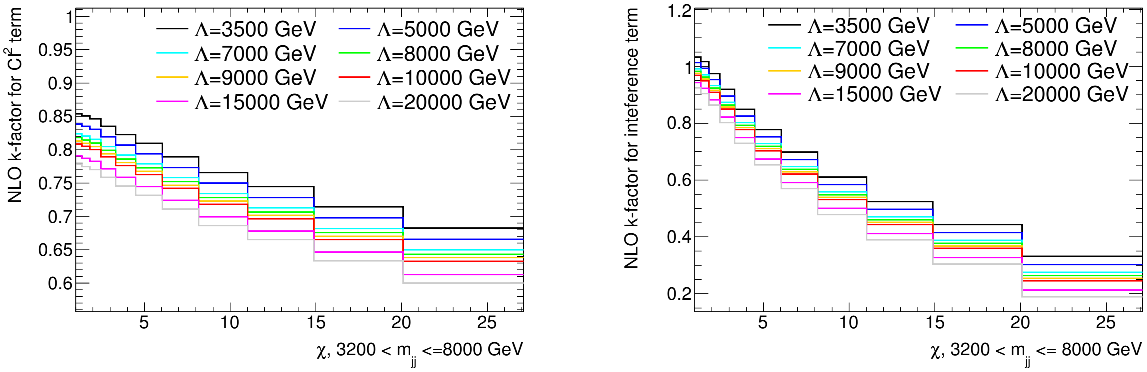

Figure 4.15: The left (right) plot shows the NLO k-factor for CI (interference) terms in $3.2 < m_{\rm jj} < 8.0$ TeV.

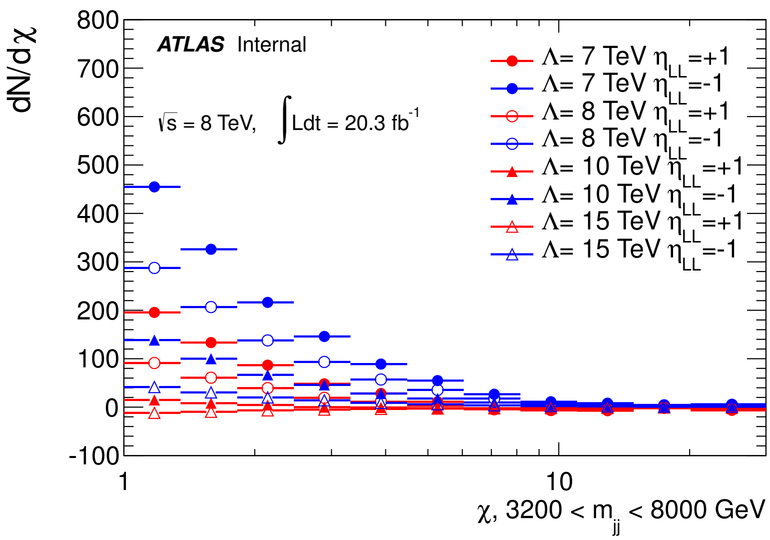

Figure 4.16: χ distributions of signal with NLO k-factor applied for various Λ scales.

Experimental uncertainties

JES uncertainty: As already mentioned in section 4.1.5, there are 58 nuisance parameters describing the JES uncertainties, but they can be reduced to nine, as seen in section 8.4 of Ref [60]. Together with the pileup and flavour uncertainties, it leads to a total of 14 nuisance parameters for this analysis. The effect of these nuisance parameters on the angular analysis is calculated using Pseudo Experiments (PEs). These nuisance parameters are varied independently for each PE, and the χ distribution is reconstructed at $\pm\sigma$ of the systematic uncertainty in question. This gives rise to an ensemble of PE distributions located around the nominal χ distribution. The 1σ uncertainty is then obtained from the envelope determined by the area that contains 68% of the PEs around the nominal distribution.

The total JES uncertainty affects mostly the unnormalised χ distributions, but because the total JES uncertainty is a quadratic sum of all nuisance parameters, the shape information for JES is lost when these distributions are normalized by their cross section. To solve this, we take the shape uncertainty from the nuisance parameters that has the greatest contribution. In this case, the highest contribution to the uncertainty originates from the EtaIntercalibration modelling.

Beam energy uncertainty: The uncertainty on the beam energy is also investigated when determining the total uncertainty, although we find this has no contribution on the normalised χ distribution. The rescaling factor on the beam energy is defined as the ratio of varied to nominal $\sqrt{s}$, which, given the nominal beam energy of 3988 ± 26 GeV, leads to a rescaling factor of the Bjorken x of 0.9935 for the (-1σ) uncertainty band and 1.0065 for the $(+1\sigma)$ uncertainty band. This leads to symmetric uncertainty bands around the nominal value, but they vanish when the angular distribution is normalised to unit area.

Theoretical uncertainties

PDF uncertainties: The PDF uncertainty is calculated using `NLOJET++` connected to `APPLgrid` [88]. Three PDFs are considered: `CT10`, `MSTW2008`, and `NNPDF23`. The error members of each PDF are used to calculate that PDF uncertainty through the envelope method [89] in equation 4.20, where $X[q^{(i)}]$ is the cross section evaluated at the member set i.

$$\sigma^{\texttt{CT10, MSTW}}(\mathrm{PDF}, \pm) = \mathrm{f} \cdot \sqrt{\sum_{\mathrm{i}=1}^{\mathrm{N}/2} (\max(\pm \mathrm{X}[\mathrm{q}^{(2\mathrm{i}-1)}] \mp \mathrm{X}[\mathrm{q}^{(0)}]), (\pm \mathrm{X}[\mathrm{q}^{(2\mathrm{i})}] \mp \mathrm{X}[\mathrm{q}^{(0)}]), 0)^2}$$

$$\sigma^{\texttt{NNPDF}}(\mathrm{PDF}, \pm) = \sqrt{\frac{1}{\mathrm{N}-1} \sum_{\mathrm{i}=1}^{\mathrm{N}} (\mathrm{X}[\mathrm{q}^{(\mathrm{i})}] - \mathrm{X}[\mathrm{q}^{(0)}])^2}, \tag{4.20}$$

where N corresponds to different sizes of member sets for the different PDF sets. For `CT10`, a rescaling factor of $f = \frac{1}{1.64485}$ is included to scale the `CT10` uncertainty from 90% to 68% CL. `MSTW` PDF has no need for rescaling ($f = 1$). The uncertainties of all three PDFs are then combined through Eqs 4.21 - 4.23, where j is the PDF set (j = `CT10`, `MSTW`, `NNPDF`). The final uncertainties are given by $\delta(\pm)$.

$$U = \max\{X^j[q^{(0)}] + \sigma^j(PDF, +)\} \tag{4.21}$$

$$L = \min\{X^j[q^{(0)}] - \sigma^j(PDF, -)\} \tag{4.22}$$

$$M = \frac{U+L}{2}; \quad \delta(+) = \frac{U-M}{M}; \quad \delta(-) = \frac{L-M}{M} \tag{4.23}$$

The PDF choice mainly affects the total cross section, and so, due to the noramlization, the PDF uncertainty nearly vanishes.

The renormalisation and factorisation scale uncertainties: The renormalisation scale, μ_{R}, and factorisation scale, μ_{F}, are varied independently by a factor of 2, where once again this is done with `NLOJET++` connected to `APPLgrid` with the nominal `CT10` PDF. Figure 4.17 shows all eight scale variations for one dijet mass bin. From these, an uncertainty is calculated from the Root Mean Square Error (RMSE) of the variations. The RMSE is calculated for each χ bin, with respect to the nominal value $\mu_{\mathrm{R}} = \mu_{\mathrm{F}} = 1$ prediction y as

$$\mathrm{RMSE}(\chi) = \sqrt{\frac{\sum_i^n (y_i(\chi) - y(\chi))^2}{n(\chi)}}, \tag{4.24}$$

where y_i is the prediction for $1/N \cdot dN/d\chi$ from variation i, and n is the number of variations leading to a higher (lower) $1/N \cdot dN/d\chi$, used for the $+1(-1)\sigma$ calculation.

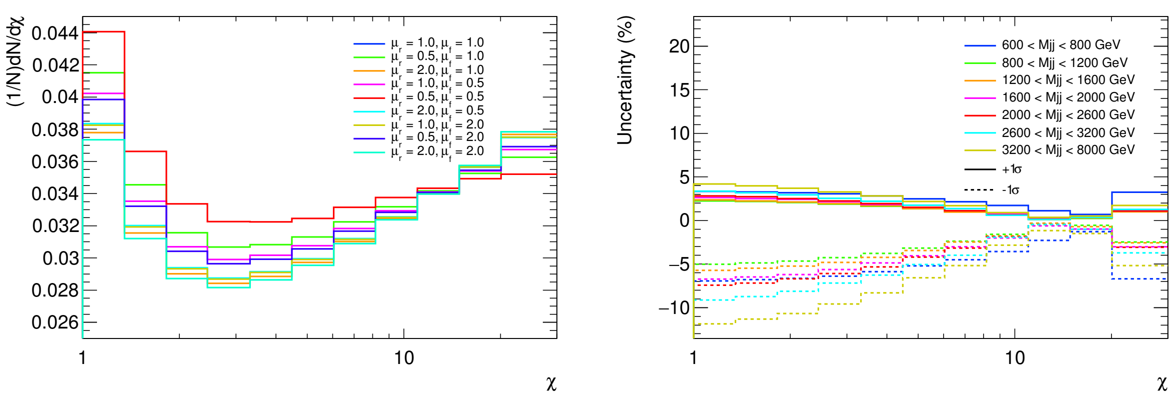

Figure 4.17: Scale variation uncertainty. Example showing scale variations in χ distribution for $2000 \leq m_{\mathrm{jj}} < 2600$ GeV is shown on the left. Relative scale uncertainties as a function of χ for all m_{jj} bins are shown on the right.

Event and showering generator uncertainties: Following the study on various MC samples described in section 4.2.4, the uncertainties related to the choice of generator have also been included in the total systematic uncertainty, comparing the predictions from the NLO generator `Powheg`, where `Pythia` has been used for final showering and hadronization, to those of Pythia after the k-factor corrections. Similarly, a showering uncertainty is evaluated by comparing this Powheg prediction to the one obtained when Herwig+Jimmy is used for showering and hadronization. The relative uncertainties due to generator choice and showering are shown in Fig 4.18.

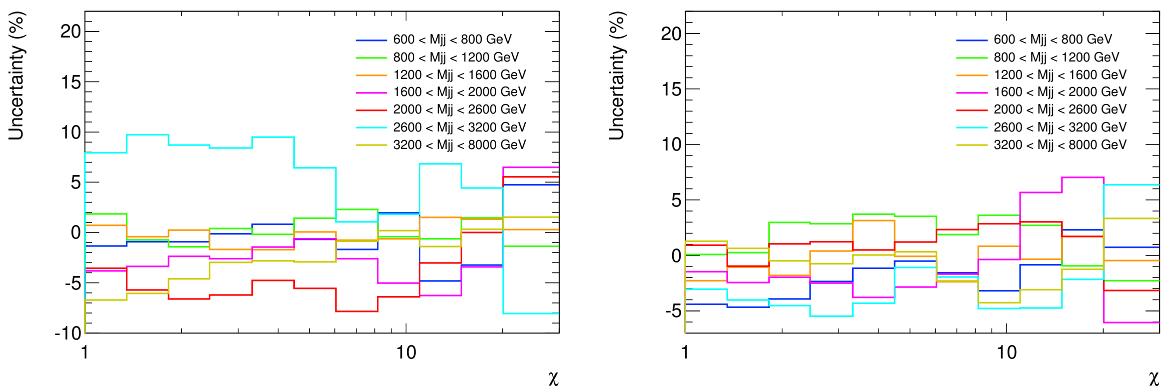

Figure 4.18: The left (right) plot shows the generator (showering) relative uncertainties as a function of χ for all m_{jj} bins.

Uncertainties due to the NLO k-factors: We take a constant 1% uncertainty, which is the uncertainty evaluated directly from NLOJET in the highest m_{jj} bin, as the statistical uncertainty on the k-factors.

In summary, the main sources of theoretical uncertainty are our choice of MC generator, PDF, and showering and hadronization tune. These uncertainties affect the limit setting on some of the models, thus each limit can be calculated using various generators, PDFs and tunes, in order to estimate the effect of the theoretical uncertainties on the value of the limits.

Total uncertainties

The total uncertainty is the combination in quadrature of all the uncertainties, theoretical and experimental, on the χ distributions for each m_{jj} bin. Figure 4.19 shows the total uncertainty for the highest m_{jj} bin. As expected, the biggest uncertainties come from the JES and the scale variations, and the total uncertainty is comparable to the one in previous analyses.

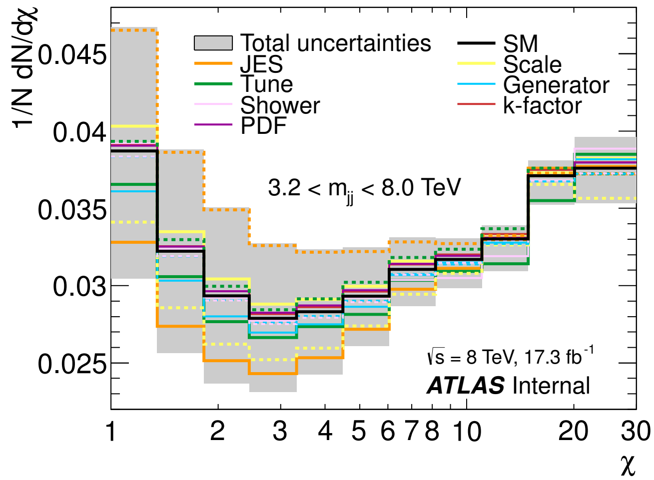

Figure 4.19: Total uncertainty (shaded band) and component-wise breakdown (lines) for the highest m_{jj} region. Dashed and solid lines represent upward and downward 1σ variations, respectively.

4.2.8 Results

Figure 4.20 shows the χ distribution normalised to unity in the different m_{jj} bins for data events, along with the MC prediction. The data distribution without the EW correction is also shown, and is in less agreement with the data for high m_{jj} bins. The SM predictions in this plot and the followings are all estimated using the `Pythia8.160` event generator with the `AU2` tune and the `CT10` PDF, using `GEANT4` detector simulation and all corrections specified in section 4.2.5.

While looking at the various m_{jj} bins one can see the similarity between the χ distributions in each one of them. This similarity is a good insentive for a data-driven background estimation. Figures 4.21 shows the same normalised χ distributions in the various m_{jj} bins. For each bin this distribution is compared to the average of the χ distribution in all m_{jj} bins excluding this specific bin and the highest one. Figure 4.22 shows the same for simulated data. When using the data-driven background only the statistical uncertainties on the data are shown, as the rest are of no interest.

The p-value for the SM hypothesis is (0.25) 0.30 for the (second) highest m_{jj} bin. The data is well described by QCD predictions at NLO. In the absence of significant deviations from the SM prediction, the F_χ variable was not investigated, and new limits were set using the χ distributions. The observed limits on CI obtained from the m_{jj} = [3.2, 8.0) TeV region are 8.1 and 12.0 TeV for destructive and constructive interference, respectively. These are lower than the expected limits, which is explained by the upward fluctuations in three consecutive bins at low χ seen in data. The fluctuations are well within the 1σ total uncertainty band of the QCD prediction. For comparison, the CMS collaboration has presented similar results, with limits extending to 9.0 TeV and 11.7 TeV for destructive and constructive interference respectively [65].

The observed limits are shown along with the expected limits as a function of Λ in Fig. 4.23. Destructive and constructive interference mode limits are shown separately. The markers show the actual Λ scan points, and the lines are an interpolation. As can be seen in the figure, the observed limit is within the 2σ uncertainty band of the expected limit for constructive interference, while for destructive interference, the observed limit is more than 2σ away from the expected limit. This tension is explained by a combination of factors. Firstly, the upward fluctuations in the three first bins of χ in this $m_{\rm jj}$ region are very signal-like. Secondly, there are also downward fluctuations at intermediate χ – in particular, there is one in the fourth bin. Thirdly, the region of low χ has the largest systematic uncertainties on the SM prediction. In the fit of signal and SM to data, these three effects jointly favour a best fit where the SM prediction is lowered slightly (to a lower value still allowed by the uncertainty band), which allows more signal to fill the increased gap between SM and data points. Since the SM prediction is substantially moved downwards, its location is very different from the expected limit one. This explains why the observed limit is more than 2σ away from the expected.

The different shapes for the two interference modes of signal also play a role, as can be understood from the different magnitude of the tension between observed and expected limit in the two cases. Since the signal shape resulting from destructive interference with QCD is steeper, a fit of signal and SM prediction to the data more easily accommodates the fluctuations in the first four χ bins (three upward and then one downward) than a combination of the flatter constructive interference signal and SM prediction does – here the intermediate and high χ regions both constrain the possibility to shift the SM prediction downwards.

The following analysis using ATLAS data with centre of mass energy of $\sqrt{s}$ =13 TeV and total luminosity of 3.6 fb^{-1} has further improved the limits on Λ to 12.0 TeV and 17.5 TeV for destructive and constructive interference respectively [10].

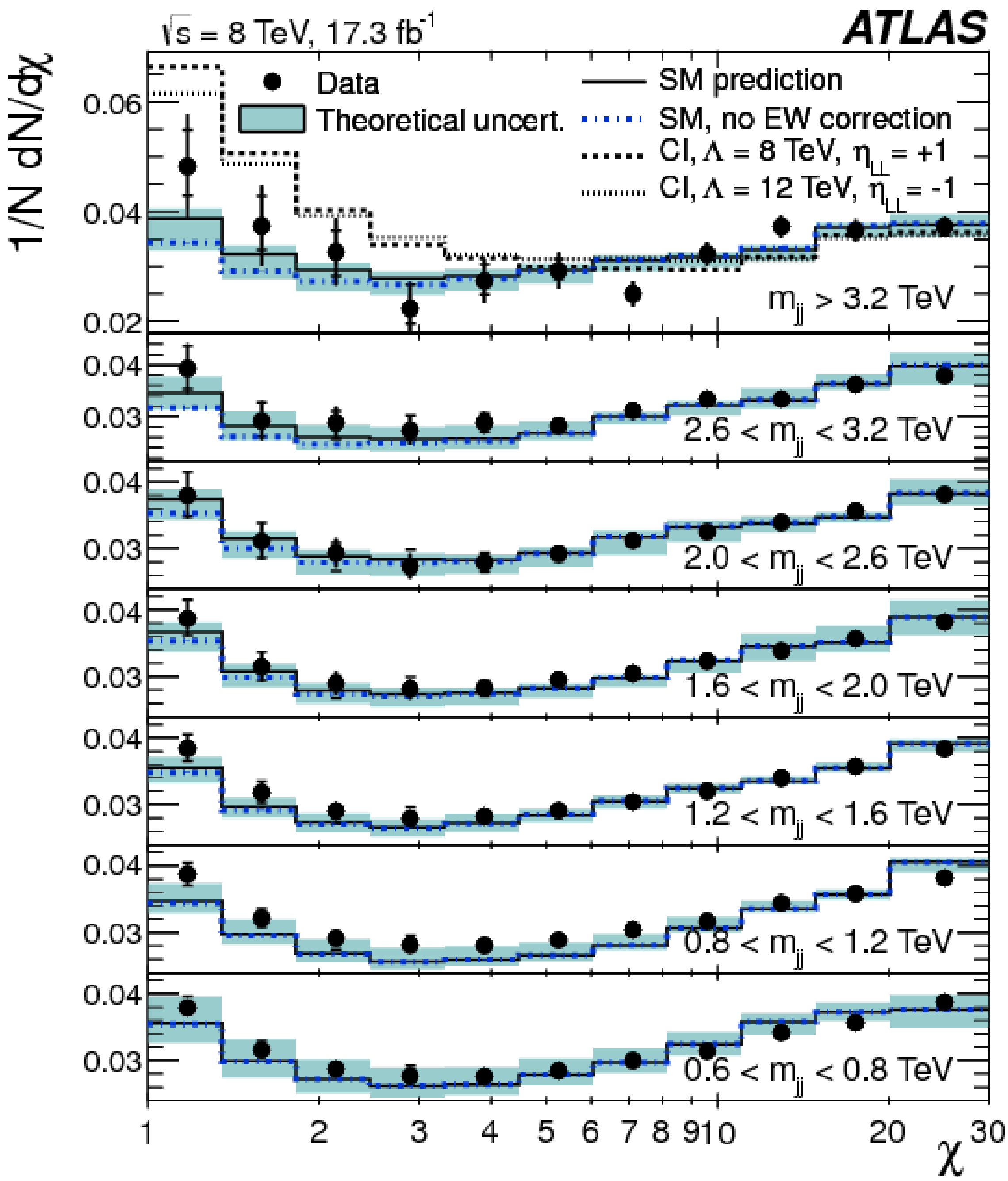

Figure 4.20: Normalised dijet angular distributions in data (dots) and SM prediction (solid line) for the seven dijet mass regions. The SM prediction without including EW corrections is also shown (dash-dotted line). The benchmark model of CI + SM is shown for destructive interference ($\eta_{LL} = +1$) at $\Lambda = 8$ TeV (dashed line), and constructive interference ($\eta_{LL} = -1$) at $\Lambda = 12$ TeV (dotted line). Uncertainties on the SM prediction are shown as a shaded band, while experimental and statistical uncertainties are added in quadrature and shown as data error bars. The tick mark represents experimental uncertainty only.

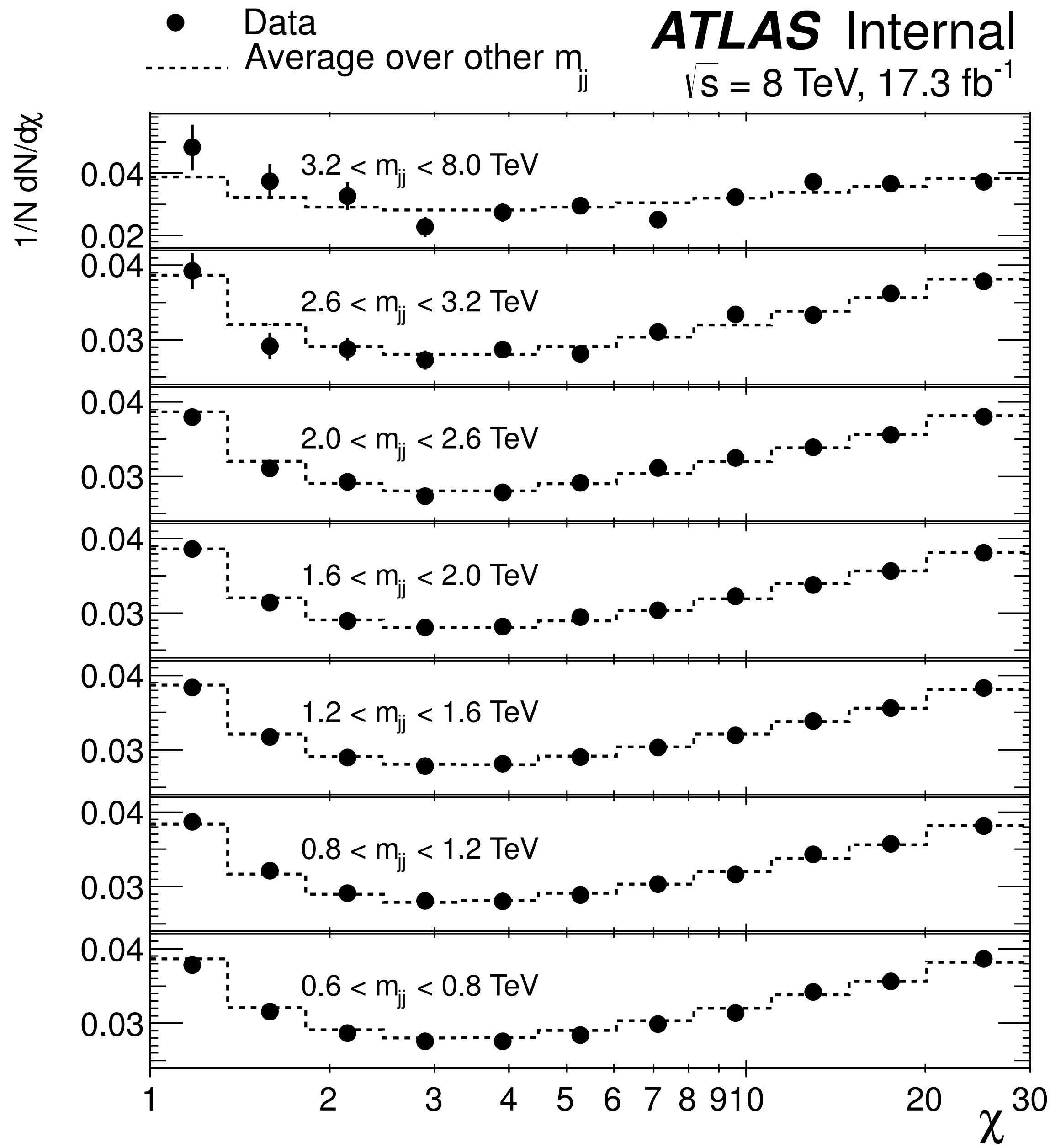

Figure 4.21: Normalised dijet angular distributions in data, shown for seven dijet mass regions with each individual distribution overlaid with the statistically weighted average over the other regions (excluding the highest m_{jj} region). The error bars on data represent statistical uncertainty only.

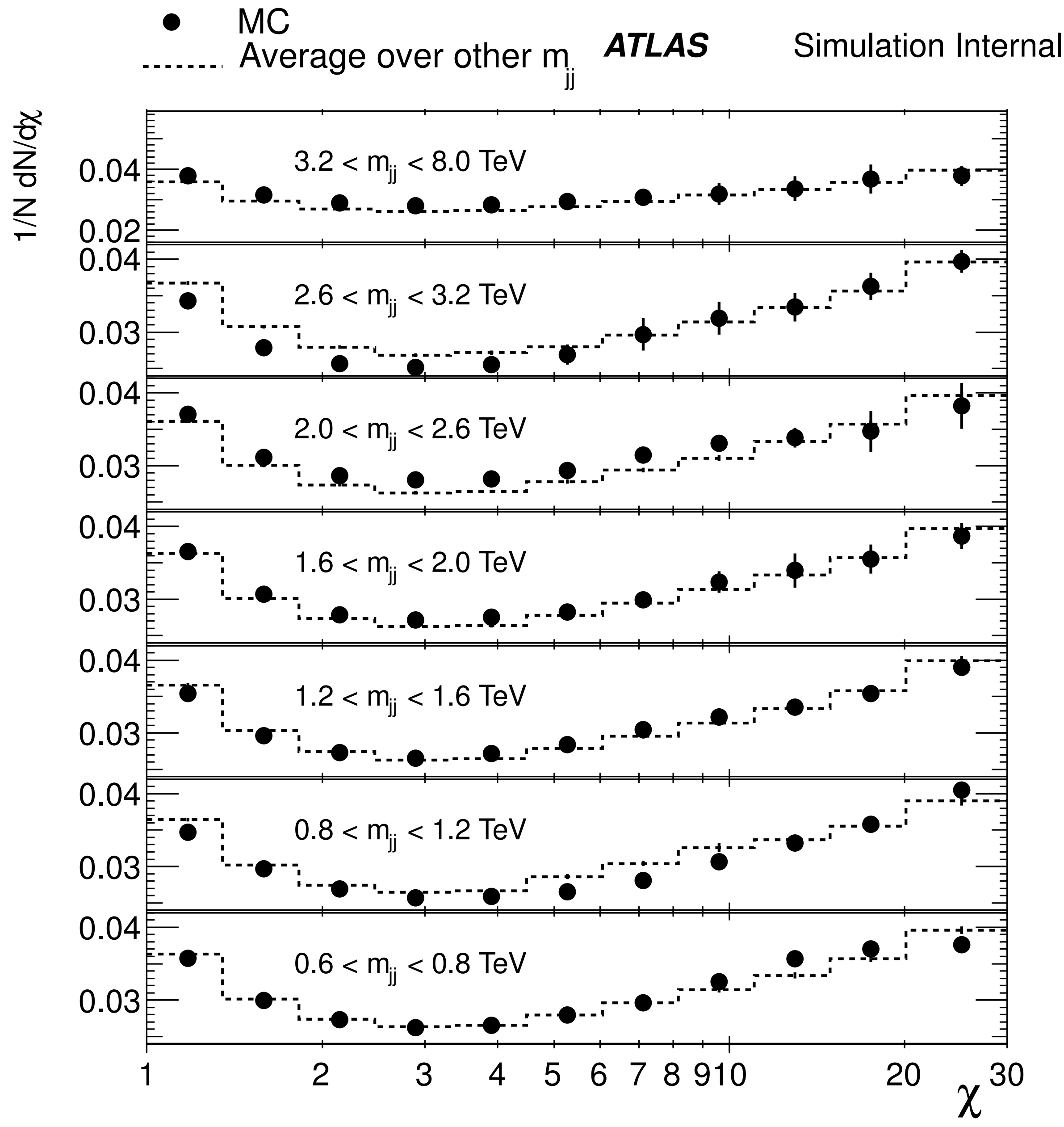

Figure 4.22: SM prediction of normalised dijet angular distributions, shown for seven dijet mass regions with each individual distribution overlaid with the statistically weighted average over the other regions (excluding the highest region). The error bars on MC represent statistical uncertainty only.

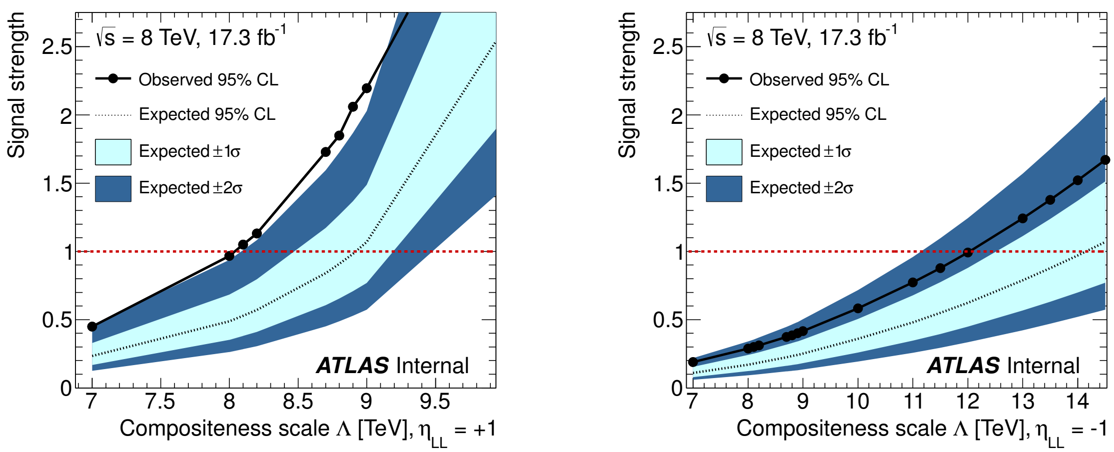

Figure 4.23: Observed and expected 95% CL value of CI signal strength vs. compositeness scale Λ, for destructive (constructive) interference mode with QCD, denoted by $\eta = +1(-1)$ on the left (right). The markers show Λ scan points, and the solid line is an interpolation. The crossing of the observed and expected 95% CL lines with the red dotted line at signal strength equals one indicates the observed and expected limit, respectively.

4.3 Dijet Trigger Level Analysis (TLA)

4.3.1 Introduction

While high-mass dijet resonances ($m_{\mathrm{jj}} > 1$ TeV) are usually the focus of ATLAS and previous experiments, the searches for rare resonances at lower dijet invariant masses are limited due to the finite trigger bandwidth. The QCD background for the dijet invariant mass distribution is a rapidly falling smooth distribution as can be seen in the schematic illustration 4.24. NP particles can be detected as localised excesses on top of this smooth distribution depending on the invariant mass of particle. A possible excess in the lower region of the dijet invariant mass will require enough statistics for it to be detected. The high rate of low p_{T} dijets events, forces the application of a prescale, p, on these triggers. Thus, the sensitivity of searches for low-mass resonances is generally limited by the limited data statistics available, and better limits are being set for higher values of resonance mass with smaller values of coupling constants. An example for such limits on vector coupling to quarks, g_B, of a Z' in a simple benchmark model with no other Standard Model interactions, obtained by various searches is shown in figure 4.25 [26]. The latest results in this figure are from ATLAS and CMS 8 TeV searches, in solid red and blue lines respectively.

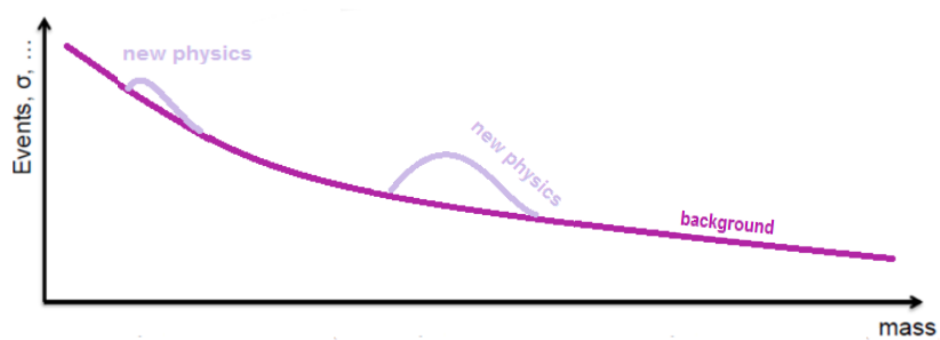

Figure 4.24: A simplistic illustration of the dijet invariant mass background and possible signals distributions.

The 20.3 fb^{-1} ATLAS dijet search at 8 TeV (solid red line in figure 4.25) [7] made use of fully-unprescaled delayed stream triggers and was added to the original plot. The 13 TeV standard searches are aimed to set limits for higher $m_{Z'}$, leaving a gap in the coverage of the lower coupling range at masses that had already been accessible in earlier experiments. The standard dijet resonance searches at both ATLAS and CMS are now statistically limited below approximately 1 TeV by the bandwidth allocated to inclusive single-jet triggers.

Two different approaches were suggested in order to overcome this limitation. The first, a 3-jet final state analysis, aiming for dijet+ISR signature, which, along with the jet pair,

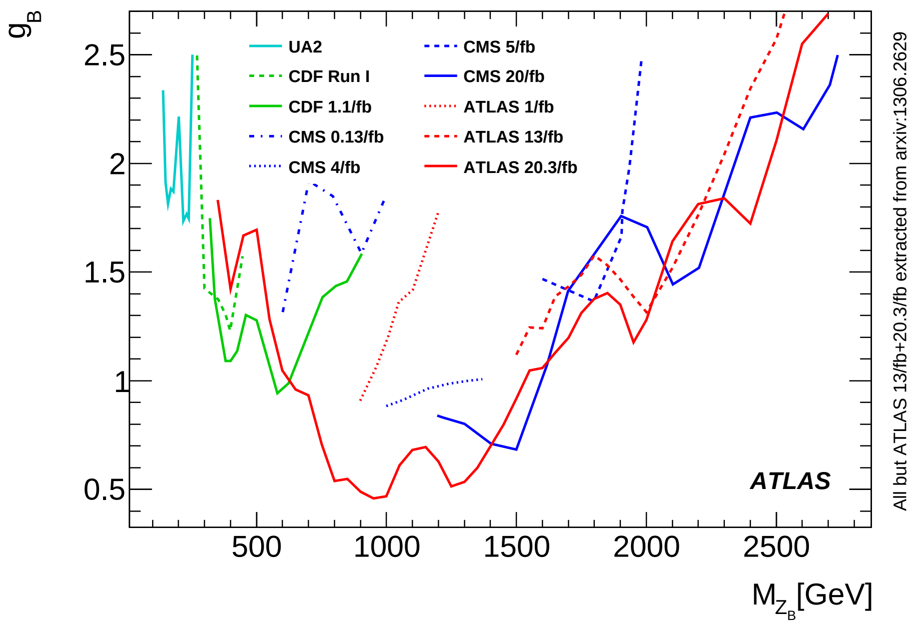

Figure 4.25: A comparison of limits on leptophobic Z' resonances circa 2014 [26], with additional input of ATLAS $\sqrt{s} = 8$ TeV results taken from [7].

requires a high-p_{T} third object that will fire a trigger with low or no prescale, and the search for resonance is done on the invariant mass of the other two jets. The second is a *DataScouting* (DS) strategy, initially explored by the CMS experiment [90], where one avoids the trigger bandwidth limitation and provides much higher event rates for all-jet searches by using the data at the trigger level, and recording only a small subset of information that is needed for the analysis.

The DS approach was adopted also by ATLAS for run-2. It is named Trigger Level Analysis (TLA), and since August 2015, partial `HLT` events were recorded. In the following, the term DS from Ref. [90] will be used for the data stream used for this analysis, while the term TLA is used to describe the analysis of these events. Since this is a precedent type of analysis in ATLAS, the work being done was also a proof of concept and a prototype of the TLA technique, which can be used also for other analyses on the trigger level data of 2016.

In principle, the TLA approach can be used for any analysis in need for more statistics, in case it satisfy the necessary conditions:

- The performance of the trigger level reconstruction of the objects used in the analysis needs to be comparable to that of the offline reconstruction
- The analysis needs only a limited number of objects.

The dijet resonance search fulfils both conditions, needing only a single collection of jets having a similar performance for trigger and offline jet objects, hence, it is a good candidate for a proof-of-principle and future developments of the TLA concept. The advantage of a TLA for dijet resonance searches is twofold:

- The analysis can be performed automatically during online data taking as a monitoring stream (DS mode), allowing early pinpointing of regions where discrepancies are growing with the chance to steer the trigger menu to study them offline.
- When analysed offline (shortly after data taking), all the data passing the chosen L1 trigger is recorded, allowing an increase in the statistics of many order of magnitude with respect to prescaled triggers in the normal stream.

First the datasets used are detailed in section 4.3.2. The choice of the `L1` trigger and the expected rates of data that needs to be written to disk are described in section 4.3.3 and the selection and search strategy is outlined in section 4.3.4, detailing the changes with respect to the standard dijet analysis [10]. A proof-of-principle sensitivity study is described in section 4.3.5, both for the search phase and limit setting procedure comparing the TLA option to results obtained with the standard analysis using prescaled triggers. Detailed descriptions of the necessary cleaning and calibration procedures for trigger jets and their validation are given in sections 4.3.6 and 4.3.7 respectively. Section 4.3.8 then shows the reconstruction efficiency of the trigger jets, and the analysis method is described in 4.3.9. Finally, the analysis results are shown in section 4.3.10.

4.3.2 Datasets, MC samples and signal simulation

The analysis uses two different data streams:

- *DataScouting* stream: this stream only contains reconstructed trigger jets, in events triggered by the a specific `L1` trigger which will be described in section 4.3.3. This is the main dataset used for this search.
- *PhysicsMain* stream: this is a normal stream as defined in section 4.1.3. It is in use by all ATLAS analyses, and contains the full events reconstructed offline selected by triggers in the physics menu. This sample contains trigger jets reconstructed online (called trigger jets) and jets reconstructed offline (called offline jets) within the same event. The subset of these events selected by a single jet trigger are used to cross-check the performance of trigger jets against that of offline jets, ensuring that the quality of jet reconstruction, cleaning and calibration of trigger jets are equivalent to those of offline jets and therefore sufficient for a physics search.

The process of recording an event for the TLA consists of retrieving a jet collection from a chosen trigger chain, applying a selection on the minimum p_{T} of the trigger jets that are saved offline, and saving a skimmed jet collection. The reconstruction is reduced to only the trigger jets, as described in section 4.1.3. Each trigger jet is saved in four different versions, defined as jet containers; Two of which are at the EM scale with and without pileup suppression, and the other two are calibrated (automatically as offline jets) again with and without pileup suppression.

The 2015 DataScouting stream recorded 3.4 fb^{-1} of data during LHC operation at 25 ns bunch spacing. A very small amount of data has been lost in reprocessing failures (order of 0.1%) well below the luminosity uncertainty, this loss of data is neglected in the final luminosity computation.

The analysis was established while blinded, using only approximately one percent of the full data statistics to reconstruct the m_{jj} distribution. Other distributions, such as the jet p_{T}, were examined on a run-by-run basis. This strategy intends to give priority to gaining confidence in the jet reconstruction, jet calibration and background estimation techniques before the analysis is performed using the full statistics. Data recorded with 50 ns bunch spacing, is also used for checks of jet performance under different conditions. This data was not included in the final search.

The Monte Carlo samples used for the studies in this note are QCD dijets generated at Leading Order (LO) using `Pythia8.176` [66], with the `A14` tune [67] and the `NNPDF2.3LO` PDF set [91], along with the 50 ns simulation and reconstruction parameters. Truth-level samples include non-perturbative effects beyond the hard scattering but no detector simulation, the average number of interactions per bunch crossing is set as 80, and *truth* jets only include particles with a lifetime longer than 10 ps and exclude muons and neutrinos.

The benchmark signals are Z' axial vector mediator with a spin of 1 and a mass of M_{med}. This kind of extension to the SM is an example for a simplified model such as those discussed in chapter 2. This particle can mediate between the SM known particles to a dark sector containing for example a DM Dirac fermion with a mass, m_{DM}. The coupling of the Z' mediator to quarks and to DM fermion are denoted as g_q and g_χ respectively. The two most relevant parameters of this model in the dijet search are the coupling of the Z' to quarks as it drives the intrinsic width of the resonance, and the Z' mass. These two parameters are scanned to obtain the signal grid used for the limit setting. The Dark Matter mass is fixed at 10 TeV beyond the kinematic limits of the analysis so only decays into quark-antiquark pairs are present. The coupling to the DM fermion is set to 1.5. Modifying the DM mass and coupling has a negligible effect on the width of the resonance. M_{med} was scanned in the range of 450-950 GeV and g_q in the range of 0.1-0.4.

In addition a model-independent signal of Gaussian templates with various means and ratios of width-to-mass (σ_G/m_G) are searched for.

4.3.3 Choice of trigger

A major keypoint for a TLA is the choice of the L1 trigger which provides the events feeding the stream used for the analysis. There are various available L1 triggers potentially suitable for this purpose, all requiring the event to have at least one jet with a threshold E_{T}, named L1_Jx where x is the threshold E_{T}. The chosen trigger should satisfy several requirements. The trigger should be unprescaled, and have the lowest E_{T} as possible, as the cut on the lowest dijet mass that can be used for the search needs to be high enough above this threshold to avoid biases due to trigger inefficiency. Since all events passing this trigger are saved automatically, the number of trigger events failing to pass the event selection for the analysis must be as low as possible. Also, in order to demonstrate that the TLA approach is feasible for a low-mass (400 GeV - 1 TeV) dijet resonance analysis at $\sqrt{s} = 13$ TeV, the expected rate of events passing a chosen first-level trigger threshold must be low enough to accommodate the band width budget which is the maximum allowed data rate. Some of the studies described below have been done as a preparation for the implementation of the DS stream, before the start of the 2015 data taking period, and are based on MC studies and on a simulation program to predict the expected L1 trigger rate.

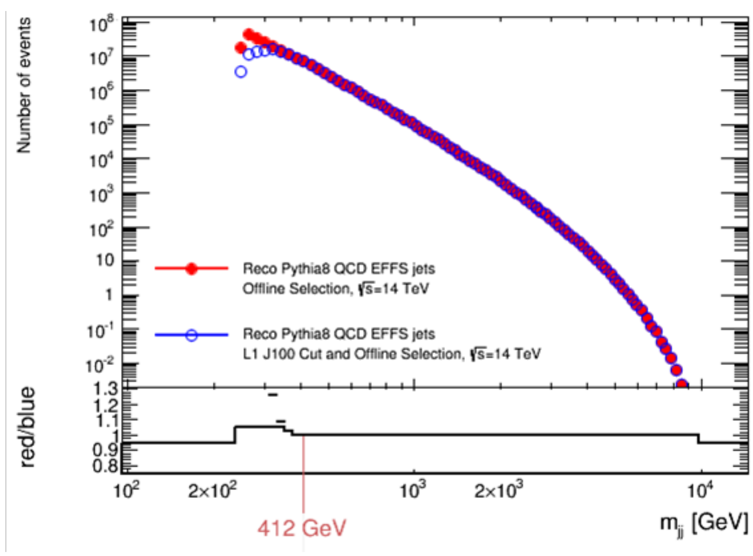

Figure 4.26: m_{jj} spectrum using MC events with and without L1_J100 cut.

QCD simulated events were used emulating the trigger decision using the trigger jets to test several options, including various L1 triggers, L1Topo and L1.5 configurations. For each trigger configuration, the minimal unbiased m_{jj} and the rate of passing events were examined. For example, figure 4.26 shows the m_{jj} spectrum for events passing the offline cuts (full dots) and events passing the L1_J100 trigger and the offline cuts (empty dots). The offline dijet mass spectrum is unbiased by the trigger cut starting from $m_{\rm jj} > 412$ GeV. Using the dedicated L1 rate prediction tool, the rate of events passing the L1_J100 trigger was expected to be 5.6 $\pm$1.1 kHz.

A simplistic study has been conducted using a representative raw data file from the 2012 data-taking period, to estimate the required storage space for the TLA. The raw file was processed to calculate the average number of jets per event and the relative share of the total event size used to save one jet collection, was found to be 42%. The storage space used for saving an average event at the raw data file level was calculated as the size of the raw files times the relative share to save one jet collection divided by the number of events in the file, and was found to be approximately 6.5 kB. This size can be reduced further by keeping fewer jets per event if necessary. Based on the estimated rate of events passing the L1_J100 trigger and the required storage space, the expected data rate requiremed to be written to disk for the TLA was estimated to be approximately 36.1 MB/s, and could have been reduced to approximately 14.4 MB/s if only jets with $p_{\rm T} > 0.3 p_{\rm T}^{\rm sublead}$ were to be saved.

Based on these approximations the TLA along with the DS stream was precedentialy approved. Following the approval, the trigger chain seeding the DS stream during the whole 2015 run was chosen to be L1_J75, as the instantaneous LHC luminosity has been sufficiently low to maintain this threshold throughout the whole 2015 run. Since this is a trigger that is already part of the menu, none of this is a unique rate for the TLA alone, hence there is no overhead on the L1 system from the TLA. The 2015 average event size, only containing the jets and minimal event information, was 30 kB/event including additional information needed for cleaning and calibration of the jets. It can be reduced to 10 kB/event when placing a $p_{\rm T}$ cut of 20 GeV on the trigger jets that are saved to storage, as planned for 2016, where the mean instantaneous luminosity is expected to be higher.

The 2015 data taking period has started with different beam properties than first commissioned. The rate of the chosen chain for one of the high-luminosity 2015 runs is shown in figure 4.27, and are found to be lower than the expected rate for an higher threshold trigger such as the L1_J100. This plot shows the large increase in the statistics of events with jets considered for the dijet search obtained by this data taking strategy. The plot shows the rate of the DS trigger along with the combined rate of all the other available single jet triggers, which is lower by more than an order of magnitude due to the prescale factors applied to remain within the overall bandwidth budget if recording the full event.

Following the choice of the seeding L1 trigger, and in order to set the kinematic cuts for an unbiased event selection, the efficiency of the L1_J75 trigger was measured from the data using a sample of events selected by a trigger with a lower threshold, L1_J15, that is fully efficient in the turn-on region of L1_J75. Figure 4.28 shows the efficiency turn-on fitted with an error function for the L1_J75 trigger. The L1_J75 trigger is at least 99.5% efficient

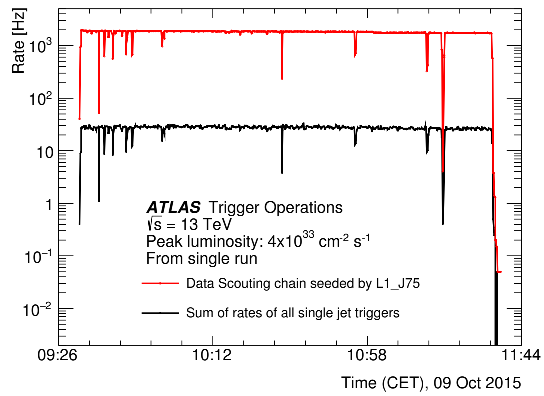

Figure 4.27: Trigger rate for the DS chain seeded by the `L1_J75` compared to the sum of the rates of all prescaled and unprescaled central single jet triggers, during a time range of a single run.

starting from an offline p_{T} of 182.461 GeV.

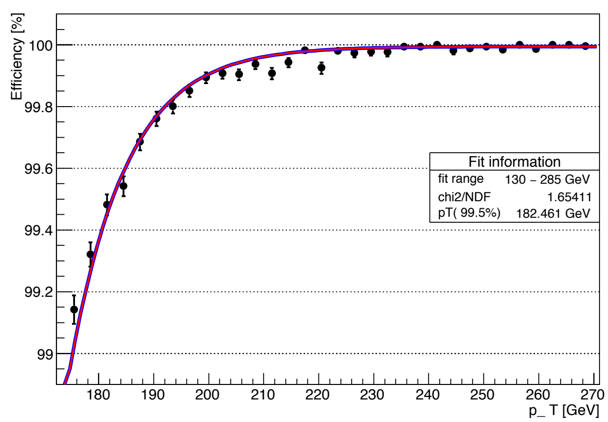

Figure 4.28: The efficiency of the `L1_J75` trigger used for this analysis as function of the reconstructed leading jet p_{T}. This curve is also known as the turn-on curve. The reference trigger was chosen to be `L1_J15`.

4.3.4 Event selection

In addition to the preselection, which was described in 4.1.6, the events selected for the dijet mass spectrum used for the search are required to pass the following selection on trigger jets:

1. Both leading and subleading jets in the events are within $|y| < 2.8$.
2. The first three jets with the largest p_{T} must pass the cleaning requirements listed in section 4.3.6.
3. The leading jet $p_{\mathrm{T},1}$ has to be larger than 185 GeV, corresponding to the plateau of the `L1` trigger efficiency curve (figure 4.28).
4. The subleading jet $p_{\mathrm{T},2}$ has to be larger than 85 GeV. This cut is not aimed to have any impact on dijet events, in which the two leading jets are usually balanced in the transverse plane. It is aimed to remove fake jets due to pileup contributions etc.
5. The variable $|y^*| = \frac{1}{2}|y_1 - y_2|$ needs to be smaller than 0.6. Here y_1 and y_2 are the rapidities of the leading and subleading jets respectively. This cut was found to increase the sensitivity of new resonances produced in the s-channel. Subset of this signal region with the requirement $|y^*| < 0.3$ is also used to search for new phenomena at masses below 600 GeV.

The cut on $p_{\mathrm{T},1}$ makes a bias on the dijet mass distribution. This bias vanish for masses above 455 (410) GeV for the case of $|y^*| < 0.6(0.3)$.

4.3.5 Sensitivity studies

All `HLT` triggers in the 2015 trigger menu for jets with $p_{\mathrm{T}} < 400$ GeV are prescaled, as can be seen in table 4.3. In previous dijet mass resonance searches [7], in order to account for event with low p_{T} jets, and to avoid loss of statistics due to the chance that an event is triggered by its subleading jet, the inclusive method which was described in section 4.1.3 was used to assign each event with a proper weight.

Increase in statistical power

For a preliminary visual estimate of the statistical power obtained with the TLA with respect to the previous analyses, a simple MC study was performed; A Gaussian resonance as mentioned in section 4.3.2 was injected on top of the background. Both signal and background

HLT	L1 seed	p_{T} threshold	Prescale p
j15	RNDM	15	120000000
j30	RNDM	30	100000000
j45	RNDM	45	10000000
j60	J20	60	260000
j80	J30	80	70000
j110	J50	110	16000
j150	J75	150	4000
j200	J100	200	880
j260	J100	260	220
j330	J100	330	52
j400	J100	400	1

Table 4.3: The L1 seeding trigger, prescales and thresholds for HLT jet triggers, from an early iteration of the jet trigger menu, dating November 2013.

were normalised to the same luminosity. The background-only hypothesis was compared to the background+signal in the following two scenarios:

- no trigger prescales (TLA scenario)
- an emulation of the trigger prescales (*prescaled triggers* scenario). The emulation consists of filling the background dijet mass distribution with events with a prescale weight taken from table 4.3 according to their leading jet p_{T}.

Figures 4.29 show the difference between the two scenarios, in terms of effective number of events. The effective number of events is defined as the number of unweighted events that would have the same statistical significance as the weighted events considered, and it is calculated bin by bin as $(\sum_i w_i)^2/\sum_i w_i^2$, where the sums are over all the events on that bin. The bin-to-bin Poisson significance [39] in the bottom panels are also calculated using the effective number of events in each bin. The emergence of the Gaussian bump is evident already from low masses in the TLA scenario, thanks to the removal of the prescale, while a discernible effect on the significance can only be seen at higher masses in the prescaled trigger scenario.

Limit setting

Expected Bayesian limits are set in the two scenarios above using a Gaussian signal of $\sigma_G/m_G = 0.07$ and QCD background, for simulated 14 TeV data corresponding to a lumi-

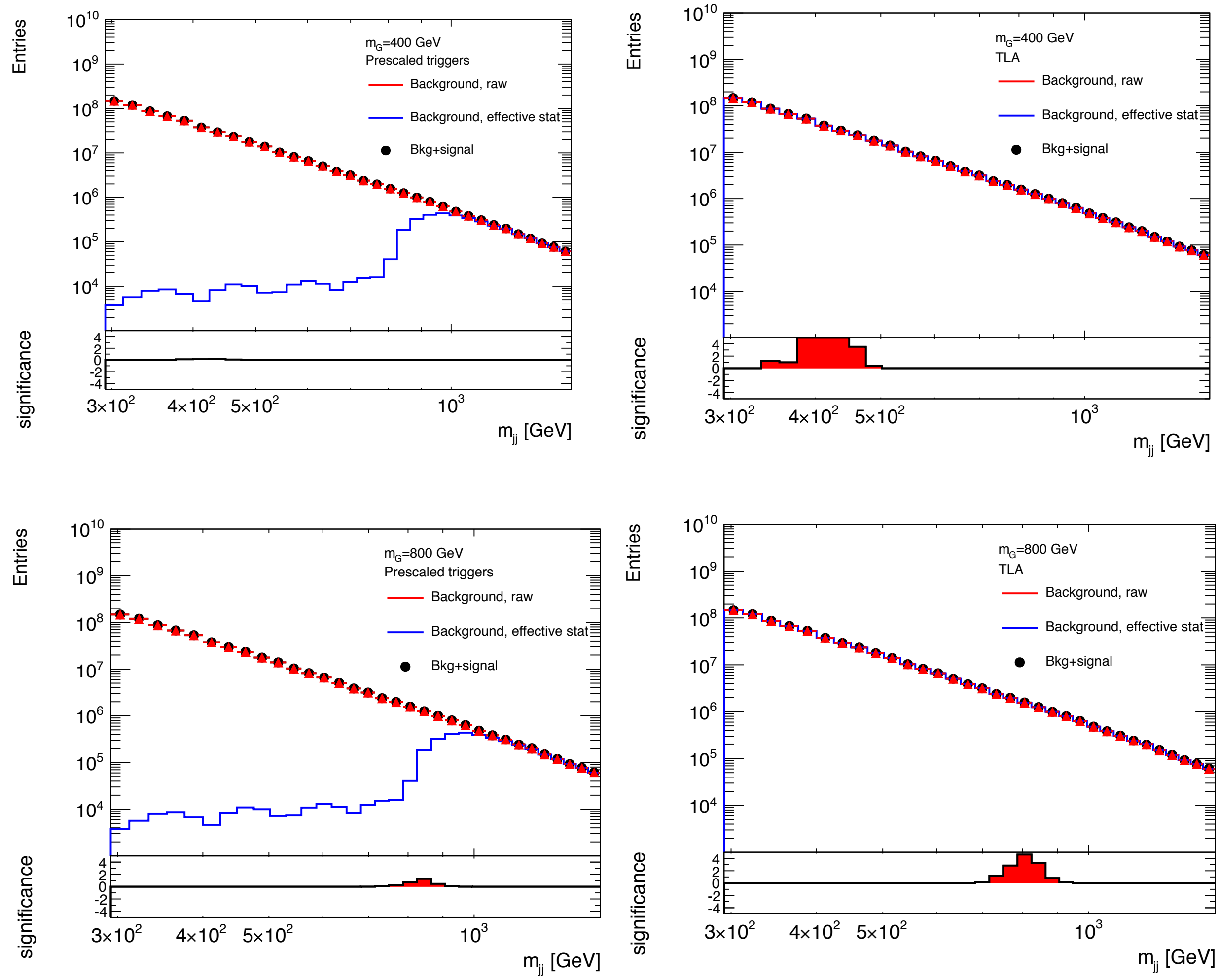

Figure 4.29: The top (bottom) plot shows dijets invariant mass comparison between QCD background and QCD background with a Gaussian bump injected, simulating a resonance with mass of 400 (800) GeV. The left (right) plots shows the comparison using prescaled (unprescaled) triggers. The bottom panel in each plots shows the bin-to-bin significances differences [39] between the background with and without the injected Gaussian bump, calculated from the Poisson probability, considering the statistical errors.

nosity of 1 fb^{-1}. Figure 4.30 shows that in the TLA scenario the limit is expected to improve by roughly two orders of magnitude with respect to the analysis using prescaled triggers.

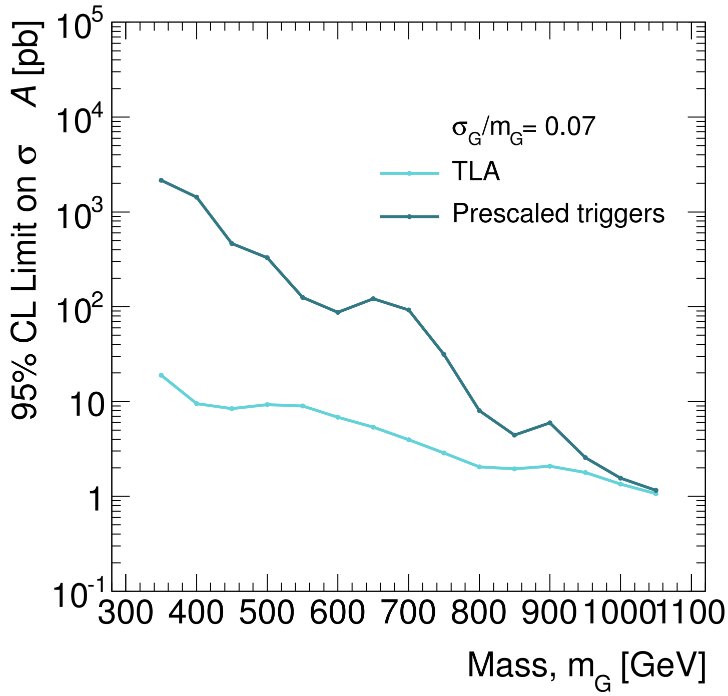

Figure 4.30: The 95% CL upper limits on $\sigma \times \mathcal{A}$ as a function of the mass of the injected Gaussian signal, for 1 fb^{-1} data at 14 TeV. The dark (light) blue dots represent the limit obtained by prescaled (unprescaled) triggers.

4.3.6 Trigger jet cleaning

A cleaning procedure such as the one described in section 4.1.4 is needed also for the trigger jets used in the TLA. When concerning trigger jets, their corresponding cleaning moments are derived in the same manner as for the offline jets, only using the topoclusters reconstructed by the `HLT` and not by the offline software. The track based variable, f_{ch}, used for the offline jet cleaning procedure, cannot be used for trigger jets as it was not saved for the 2015 data.

The optimisation of the original cleaning procedure for offline jets, described in section 4.1.4, was done using a MC based study by comparing the reconstructed clean jets to their correlated truth jets. The jet timing is not used for the cleaning procedure, and so it can be used to validate it. The same study and optimisation can be performed for the trigger jets using a data driven method, comparing the clean trigger jets to their matched offline jets. This potentially allows the use of the timing as part of the cleaning procedure.

In order to validate the jet identification selection for trigger jets, a combination of all prescaled triggers is used to select events containing trigger and offline jets. A comparison between all the cleaning moments as obtained for trigger and for offline jets was conducted for 2015 data. The comparison was using `HLT` trigger jets after pileup suppression and calibration and offline calibrated jets. Cuts of leading jet $p_{\mathrm{T}} > 100$ GeV subleading jet $p_{\mathrm{T}} > 50$ GeV, were made for the offline jets. Trigger jets and offline jets within the same event are matched within a ΔR of 0.3. The study based on data from period c4 of 50 nsec data taken in summer 2015, showed a major differences mostly in the timing and E_{neg}. These differences have not being observed in the 25 nsec data in the following period, and will be summarised hereby.

Most cleaning variables obtained from the 50 nsec data, have shown good agreement between offline jets and trigger jets, as can be seen in figure 4.31. In the data taken with bunch spacing of 50 nsec, The E_{neg} distribution in figure 4.31 does not show the same agreement. While the offline jet distribution of E_{neg} is very narrow around zero, the trigger jet distribution has larger tails. Further investigation shows that the E_{neg} differences are shown mostly for jets with low p_{T} and $|\eta| > 2.8$, which are removed via the TLA event selection. Also the timing distributions in figure 4.31 show differences. The Trigger jets passing the TLA analysis cut, have timing with larger absolute values, resulting in a wider distribution. No correlation was found between the timing disagreement and the run number, luminosity block, NPV, or pileup characterisation, $\langle\mu\rangle$.

The trigger jet timing dependency on the kinematic variables of the jet: p_{T}, η and ϕ are shown in figure 4.32. Most trigger jets with bad timing (absolute value above 5 nsec) have low p_{T} (< 200 GeV) and are in the central region of the calorimeter $|\eta| < 1.7$. One can also spot specific values for η and ϕ, in which the jets have worse timing such as $\eta \approx -1.9$ for trigger jets. A similar analysis for the offline jets which is not shown here shows events with worse timing at $\phi \approx 1.6$. Looking at the timing with respect to η or ϕ for the unmatched triggers only, one can notice timing values far away from zero for very specific values of η and ϕ as can be seen in figure 4.33. Figure 4.34 shows the index of the sampling layer in the calorimeter in which the maximum fraction of energy was deposited for these unmatched jets. One can spot many entries in the sampling layer number 12 which stands for the TileBar0, in the same regions of η and ϕ, for which the jets with timing values larger than expected were measured. Also, when looking at the number of cells in which 90% of the energy was deposited, in these specific region, it is just 1. This suggests that the bad timing for trigger jets are due to a problem in the tile calorimeter and could be caused by unmasked dead or noisy tile cells for trigger jets.

As noted, these observation have changed for the data taken in the following periods with bunch separation of 25 nsec. Figure 4.35 show the same comparison as in figure 4.31 as obtained from data taking period with 25 nsec bunch separation. Again, most of the cleaning variables show good agreement between offline and matched trigger jets. The E_{neg} and timing distributions are in better agreement than they were for the 50 nsec data.

There are differences in the timing reconstruction of offline and trigger jets. The response of the timing, which is the difference between the timing of a trigger jet and the timing of its matched offline jet was examined in various bins of η or p_{T} as can be seen for example in figure 4.36. One can see that the difference is still there also for jet with high p_{T} where the offline timing is good. Following all that was shown above, it was decided that the timing variable shell not be used for the cleaning procedure nor for its validation.

After offline and trigger jet cleaning, only a fraction of trigger jets smaller than 0.01% does not match any offline jet, a fraction that is smaller than the statistical uncertainties. This gives confidence in the use of cleaning moments as obtained by the trigger jets for the cleaning procedure. It also proves that the charged fraction cut, applied to offline jets but not to trigger jets, is not necessary.

Figure 4.37 shows the timing and leading jet transverse momentum spectrum after the TLA selection for all jets in DS stream passing the cleaning cuts and matched to a jet in the PhysicsMain stream, for unmatched jets from the DS stream, and unmatched jets from the DS stream passing also the cleaning procedure. In this plot one can see the negligible number of unmatched jets left in the analysis which pass both TLA event selection and cleaning criteria.

Cross-checks of charged fraction cut Since the charged fraction cut is the only jet cleaning variable not available for trigger jets, an additional check is performed to verify that its absence will not damage the cleaning procedure. The charged fraction variable is used in combination with an EM fraction cut to remove beam induced background and cosmic rays.

In the data taken during 2011, events with beam induced background were characterised with particles in the horizontal direction ($\phi = 0, \pi$). This is considered to be an artefact of two main effects; The first is the energetic particles escaping the last collimator before the interaction point, the Tertiary Collimators (TCT), located at the sides of the beam. The second is inelastic interaction between the beam and gas particles in the beam pipe. Those of which originating in the bended part of the pipe will continue moving tangentially, pass via several bending dipoles and will spread at the horizontal plane [92]. In case energy depositions from the beam induced background will be reconstructed and identified as one of the two leading jets, we should expect small excesses in the dijet ϕ distribution at $\phi = 0, \pi$. This is not expected in any case, given the dijet selection and the dijet invariant mass cut. Inverting the EM fraction cut used in combination with the charged fraction cut can provide an indication of the percentage of fake jets. The ϕ distribution of the events passing the TLA analysis cuts is checked for the characteristic pattern peaking at 0 and π in different intervals of the EM fraction. The interval $0< f_{\mathrm{EM}} <0.04$ is expected to contain more events from cosmic ray and beam background. This percentage is non-zero in offline jets as well. The comparison of the distributions in the different EM fraction interval for trigger jets in figure 4.38 shows that in a dijet topology there are no significant differences in the fraction of jets at 0 and π also when not applying the cut on f_{EM}.

Robustness of dijet invariant mass distribution against fake jets Since the dijet topology is already eliminating many of the events which are suspected to have uncleaned jets, the effect of the cleaning procedure on the m_{jj} distribution is expected to be very small. Figure 4.39 shows the m_{jj} distribution used for the search, in both offline and trigger jets in a single run. The cleaning cuts remove in fact a negligible number of events, expected to be within statistical uncertainties in all m_{jj} bins. This is also the case in the high-mass dijet analysis [10].

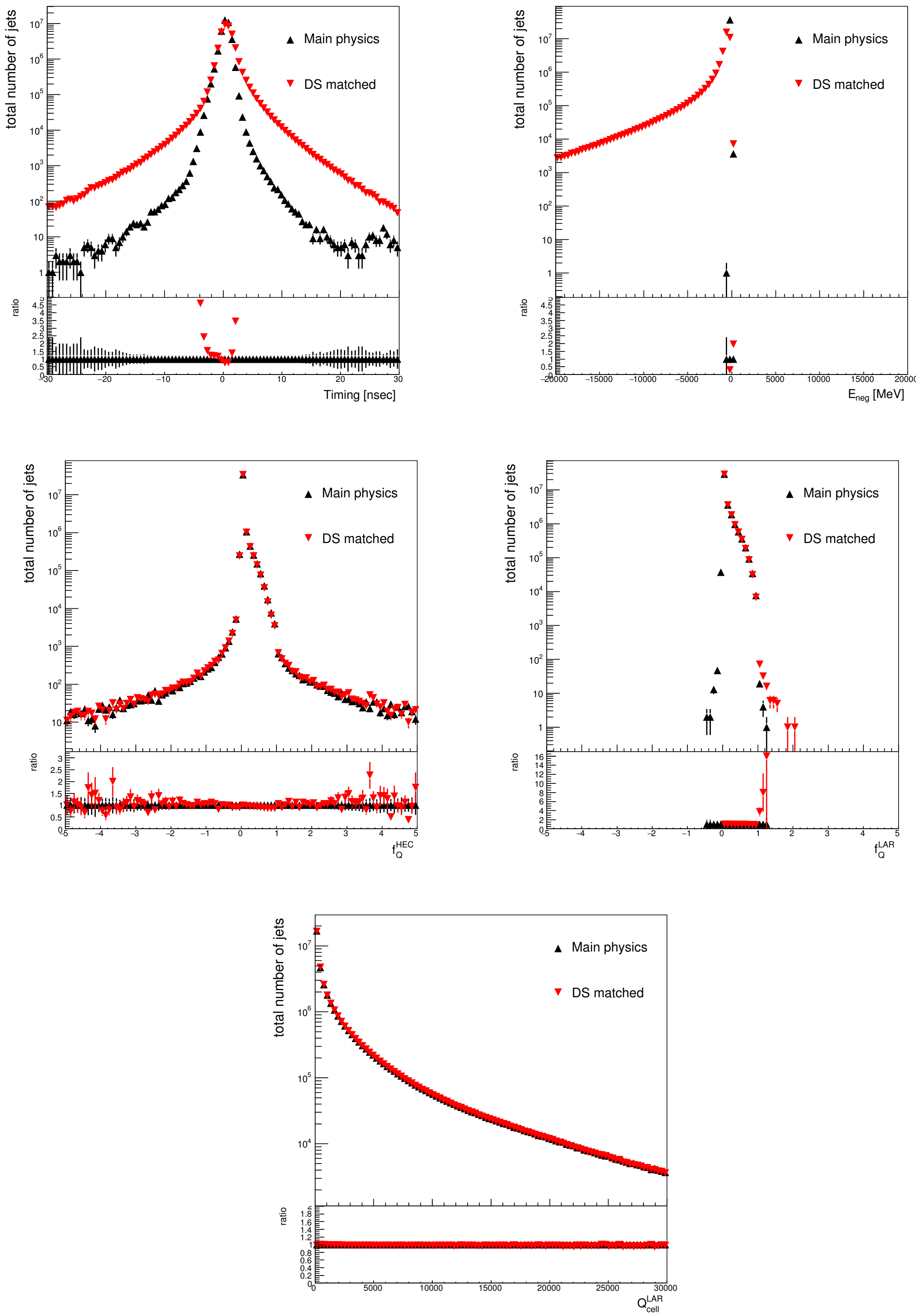

Figure 4.31: Comparison between representative cleaning moments as obtained from data with bunch separation of 50 nsec. The black dots stands for offline jets and the red for trigger jets for which there is a matched offline jet within $\Delta R < 0.3$.

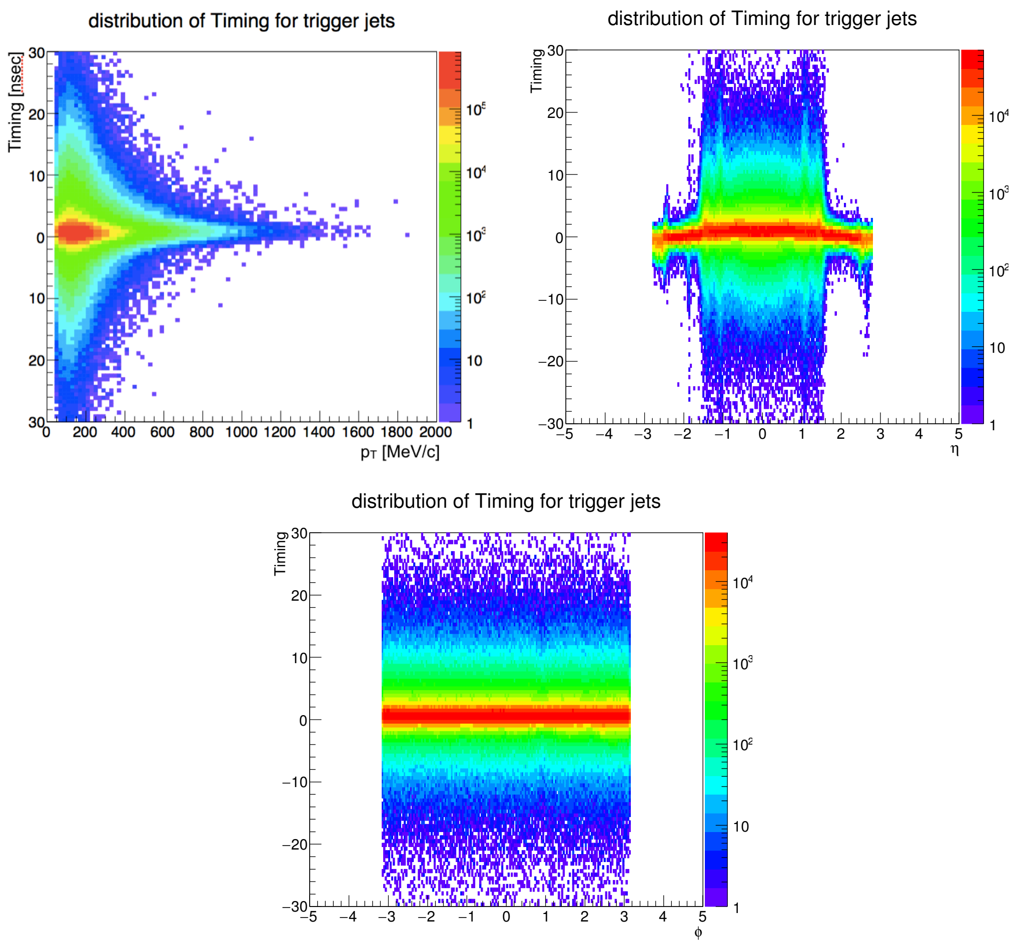

Figure 4.32: Timing of trigger jets vs. one of each jet kinematic variables (either p_{T}, η or ϕ) as obtained from data of period c4 with bunch separation of 50 nsec.

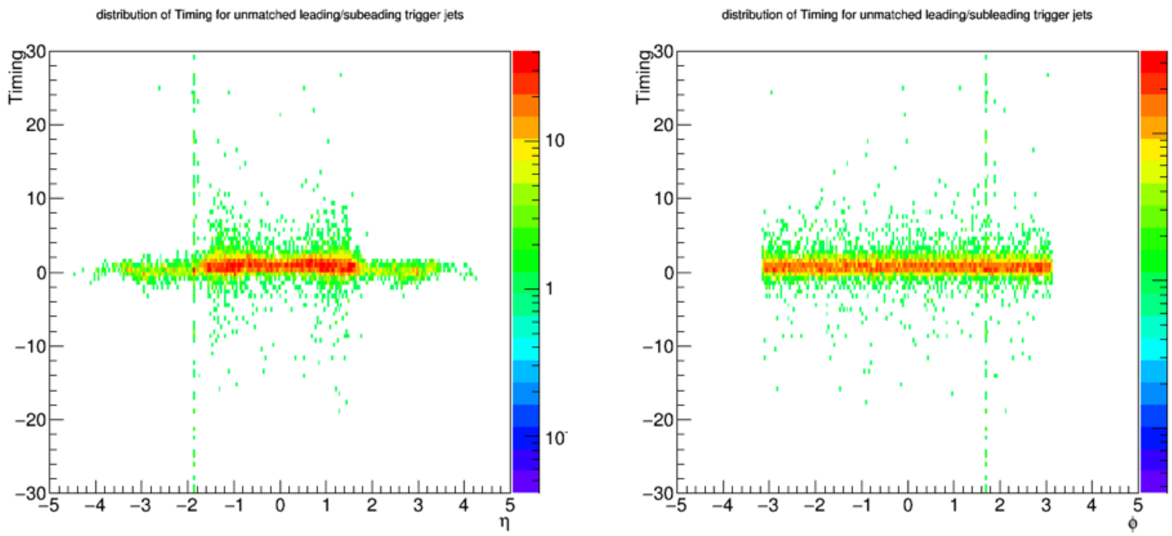

Figure 4.33: Unmatched trigger jet timing with respect to their η (left) or ϕ (right) as obtained from data with bunch separation of 50 nsec.

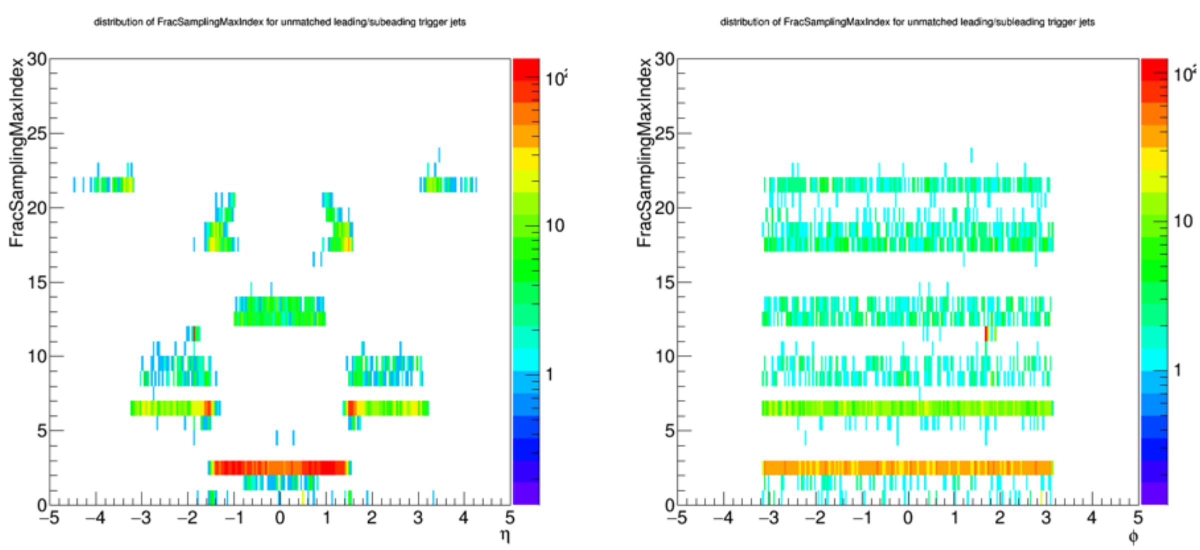

Figure 4.34: The index of sampling layer in the calorimeter in which the maximum fraction of a jet energy was deposited with respect to the jet η (left) or ϕ (right) as obtained from data with bunch separation of 50 nsec for trigger jets not matched to any offline jet.

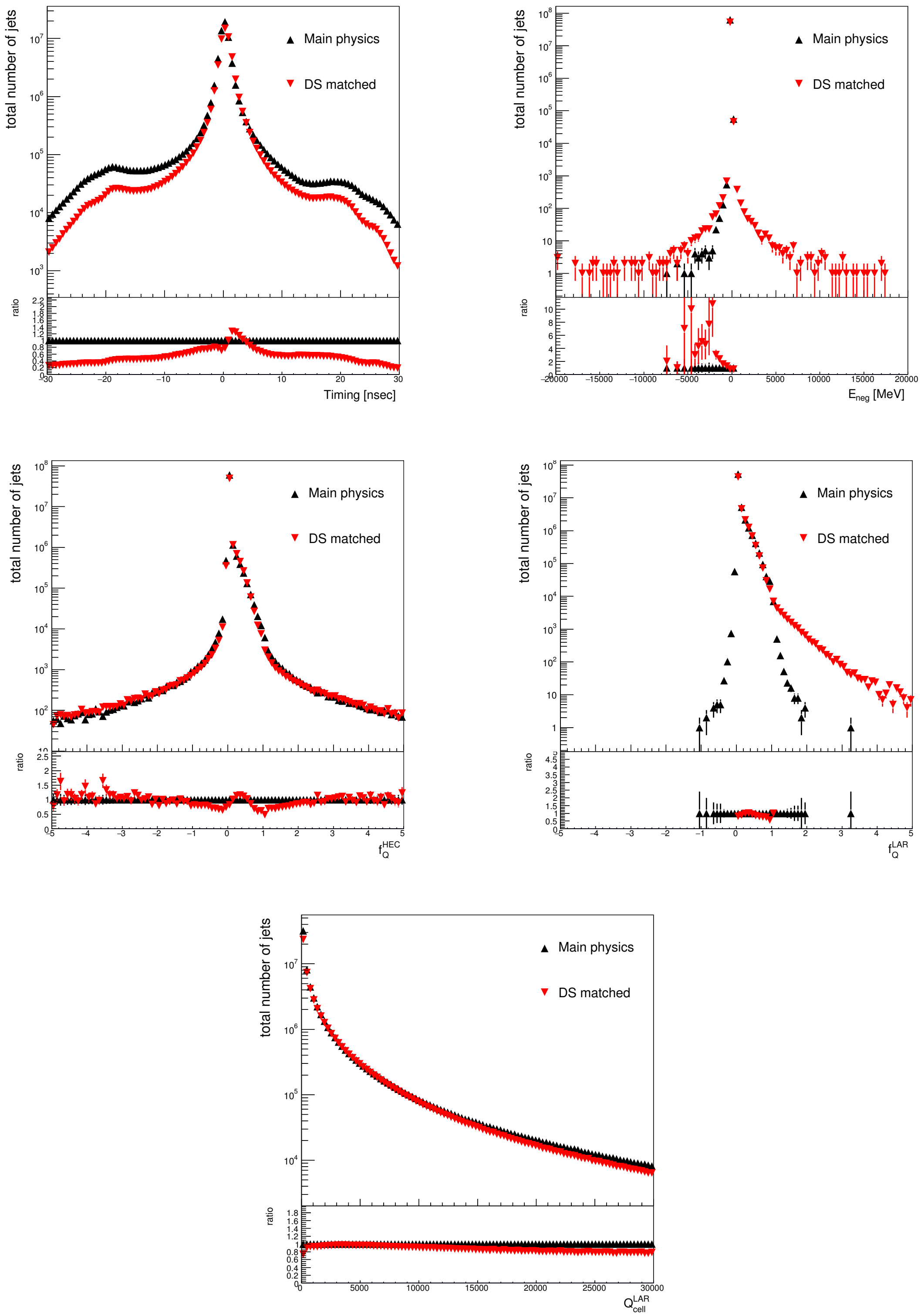

Figure 4.35: Various cleaning moments spectra after the TLA selection for jets in Physics-Main stream (black) and jets in the DataScouting (red), for jets in both streams matched to each other as obtained from all runs with bunch spacing of 25 nsec.

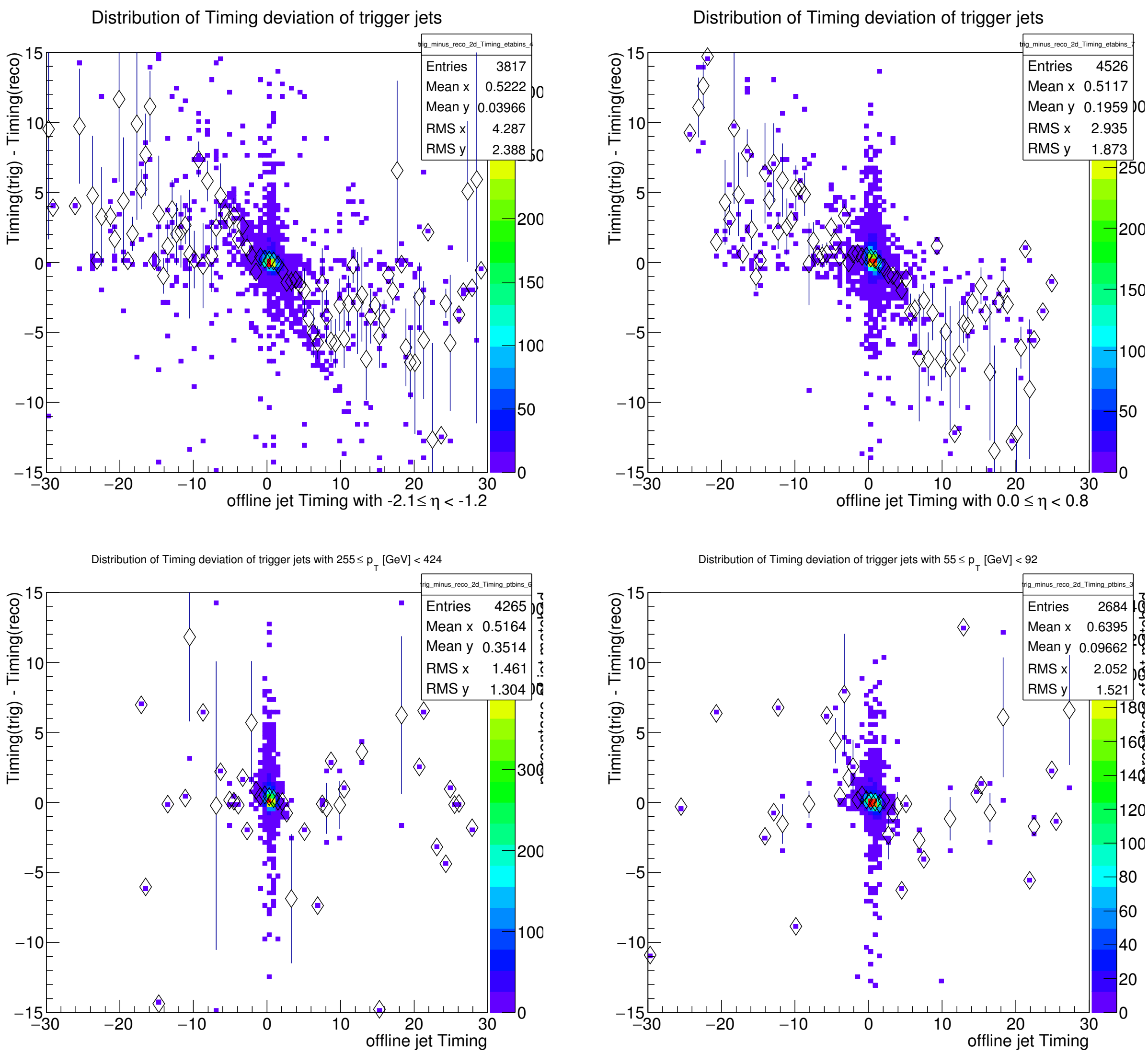

Figure 4.36: Timing response in specific η and $p_{\rm T}$ bins as obtained from data with bunch separation of 25 nsec.

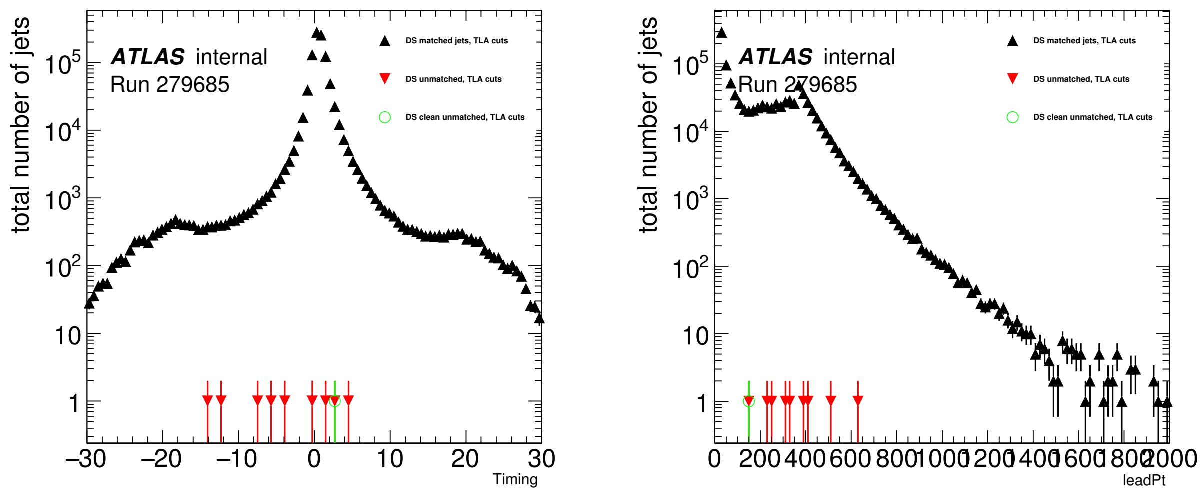

Figure 4.37: The left (right) plot show the timing (leading jet transverse momentum) spectrum after the TLA selection for all jets in DS stream passing the cleaning cuts and matched to a jet in the PhysicsMain stream (black), unmatched jets from the DS stream (red), and unmatched jets from the DS stream passing also the cleaning procedure (green) as obtained from all runs with bunch spacing of 25 nsec.

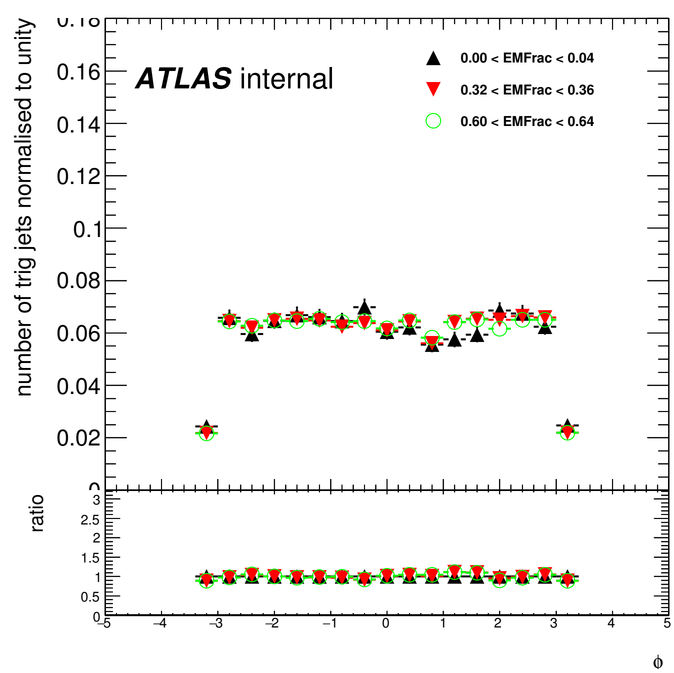

Figure 4.38: Jet ϕ distribution after jet cleaning, for offline and trigger jets, for intervals of EM fraction, in the DS stream for trigger jets.

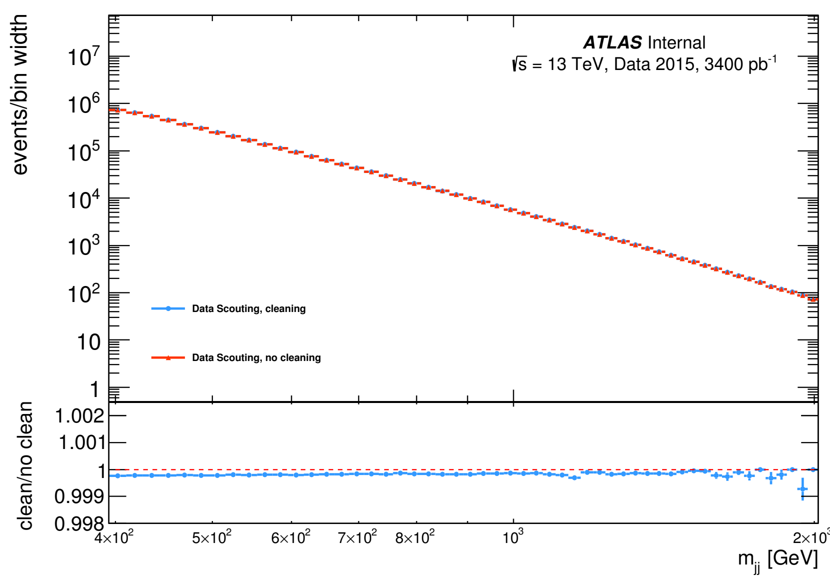

Figure 4.39: Comparison of dijet invariant mass spectrum from the DS stream within a single run (bunch spacing of 25 nsec) with (cleaned) and without (raw) applying jet cleaning selection. The jet cleaning selection consists in discarding events if either leading or subleading jets do not pass the cleaning criteria.

4.3.7 Trigger jet calibration

The overall strategy for trigger jet calibration is aimed to be as close as possible to the offline calibration procedure, described in section 4.1.5. The various steps have been modified specifically for the trigger jets as will be described in the following. Trigger jets are obtained using only the calorimeters, and do not have any track based nor muon spectrometer based information. Thus, some of the stages of the calibration used for the offline jets are not applicable to trigger jets, namely the origin correction, the residual pileup offset correction and the global sequential calibration. In addition, after the η-intercalibration step, a data-driven correction in bins of η and p_{T} is applied to calibrate the trigger jets to the same energy scale of offline jets, prior to the final in-situ correction. Then, once the trigger jets are on the same scale as the offline jets, the final in-situ step of the calibration chain is applied to both kinds of jets, yielding the same associated systematic uncertainties.

Pileup correction: The out of time pileup correction based on the position of the event inside the bunch train is done in the same manner as for the offline jets. Also, the event-by-event pileup subtraction is done as it is done for the offline jets [93]. The last correction based on $\langle \mu \rangle$ and NPV is not applicable to trigger jets as the NPV is not available. This correction is largest for $|\eta| > 2.4$, outside the region of interest for the TLA analysis due to the y^* cut. Also, the jets in the analysis are restricted to have p_{T} larger than 85 GeV, and so this correction is smaller than the other corrections applied to the trigger jets.

Lack of origin correction: The information on the location of the primary vertex is not available in the DS stream. The analysis is not affected by lack of this correction, as the average jet energy scale is not modified by it and the analysis acceptance is not sensitive to small changes in the η resolution, given that there is only one signal region and that jets after the analysis cuts are mostly central. Furthermore, the origin correction is absent in both data and Monte Carlo simulation, so there is no need for additional systematic uncertainties in the limit setting phase.

MC based calibration of trigger jets: The main correction from pileup subtraction scale to hadronic jet energy scale is derived using a numerical inversion technique, comparing reconstructed and truth jet energies in the QCD MC simulation of section 4.3.2. This procedure was repeated using trigger jets, and will be detailed below.

Ideally, the calibration constants should have been derived for the jet container of non calibrated jets at the EM scale with pileup suppression. This way, the MC based calibration would have produced a new calibration ignoring the one used for offfline jets. Unfortunately, the lowest threshold trigger which was used to obtain this jet container was set to 400 GeV, and so the low p_T region is missing. Therefore, the jet container of jets after calibration and pileup suppression was used. As described for the offline jets, in each bin of η and p_T the distribution of the differences in p_T between each trigger jet and its matched truth jet was drawn. Only truth or trigger jets passing the isolation criteria of $\Delta R > 0.4$ were considered in this procedure. The truth matching to trigger jet criteria was using $\Delta R < 0.2$.

Due to the rapidly falling p_T distribution of the most dominant QCD contribution to the dijets events, the MC samples used, which were described in section 4.3.2, were generated in slices of leading jet p_T. This way each region of p_T has the same number of events but corresponds to a differenct value of integrated luminosity, and later on gets a constant weight to normalise it to an integrated luminosity value common to all p_T regions, thus obtaining an overall smooth p_T distribution. In addition, as usually in MC generation, each event has its own weight, referred to as the event weight. The MC datasets used for the calibration were generated before data taking has started, and so the $\langle\mu\rangle$ distribution of the events was chosen to be flat. The Pileup ReWeighing (PRW) tool is assigning a weight to each event so that the NPV distributions in MC will resemble the one from data. This third weight will be referred to as the pileup weight.

In principle, the calibration is derived using all jets in the events, and so should not be dependent on the weights of the events. When deriving the calibration curves with the weighted events using the event and slice weights, a discrepancy has emerged at around $E = 100$ GeV, as can be seen in figure 4.40, which is clearly due to the `HLT j100` trigger used in the event generation. The trigger selection allows only events with leading jet with $p_T > 100$ GeV to take part in the calibration procedure, leaving the $p_T < 100$ GeV to be dominated by only non-leading jets which affects the calibration curve.

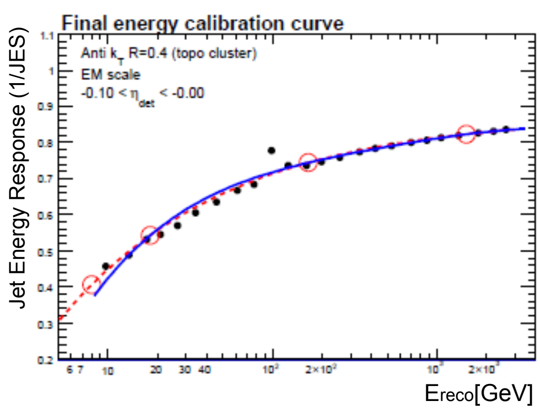

Figure 4.40: An example for calibration curve for jets with $-0.1 < \eta < 0$, obtained by simulated weighted dijets events. The black points are the energy response and the blue line is the calibration curve as described in section 4.1.5. The red line and circles show an additional fit obtained with a wider range, which was not used for the calibration.

When not using any weights at all, the calibration curves obtained are smoother, but jets in each sample are dominated by the highest p_{T} region, representing only a small fraction of the events, potentially biasing the calibration. Therefore, it was decided, as a compromise to derive this calibration using the event weights only. Figure 4.41 shows a two dimensional distribution of the energy response with respect to the energy of the truth jets, when using only the events weights, and figure 4.42 shows the calibration curve obtained and a closure test demonstrating a first validation of this calibration procedure.

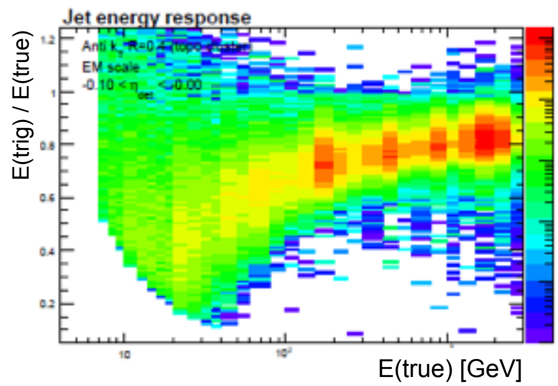

Figure 4.41: Jet energy response with respect to the truth jet energy for jets with $-0.1 < \eta < 0$, obtained by simulated dijets events, weighted only by the event weight.

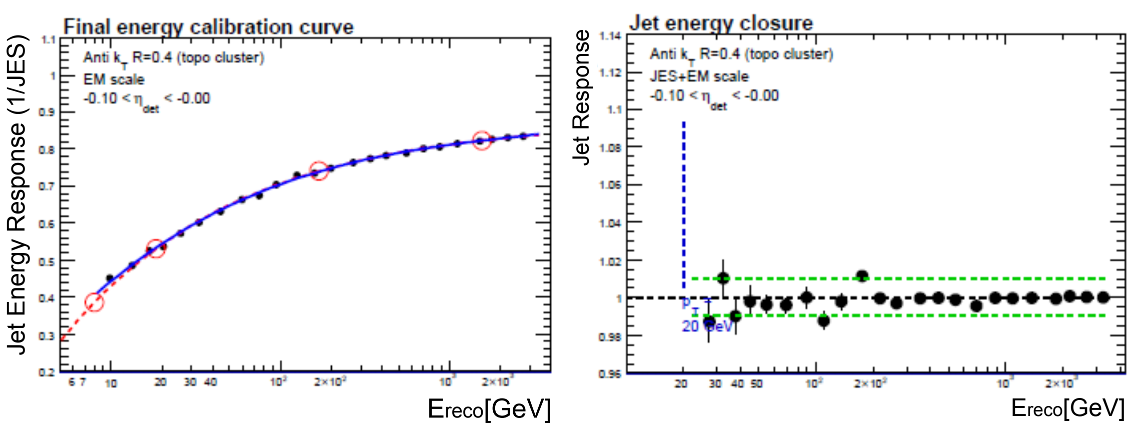

Figure 4.42: Left: calibration curve (as in figure 4.40) for jets with $-0.1 < \eta < 0$, obtained by simulated dijets events weighted using the event weights only. Right: Closure test showing the ratio between energies of the trigger jets used for deriving the MC based calibration after this calibration was applied and the truth jets.

The response of trigger jets, calculated as the ratio between calibrated trigger jets and offline jets was found to be sufficient. Nevertheless, this response was also found to be growing with the number of primary vertices, suggesting the pileup is not treated properly in the calibration process. In order to check how the $\langle\mu\rangle$ distribution in MC affects the calibration, new calibration constants have been derived from the MC datasets after applying a combined weight, which is the product of the event, slice and pileup weights. Due to the big difference in the $\langle \mu \rangle$ distributions in data and MC, the PRW left many events with zero weight, causing several empty bins of p_{T} and η, especially in the highest region of p_{T}.

Figure 4.43 shows a comparison between two calibration curves derived for the same MC events with $0.0 < \eta < 0.1$, with and without applying PRW procedure. The curve are very similar and this similarity holds up to $|\eta|$ values of 1.4. In the higher η bins, differences show up for $p_{\mathrm{T}} > 1$ TeV. We suspect these differences are coming from lack of statistics in these bins for the pileup reweighted MC sample due to the zero weights assigned to many of the events.

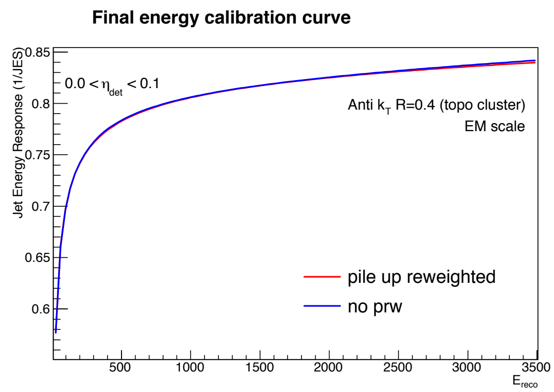

Figure 4.43: Comparison between calibration curves for events with $0.0 < \eta < 0.1$, when derived with and without PRW tool applied to the MC datasets.

All calibration constants for trigger jets for different jet energy values in bins of reconstructed η and the truth jet energy are summarised in figure 4.44.

The calibration was found to be successful as can be seen in the responses of the trigger jets. Figure 4.45 shows the ratio of the trigger and truth jet energies for matched jets (calibration closure). These trigger jets were used after correction for pileup and applying dedicated MC-based jet energy scale correction factors. The calibration is derived for all jets in the detector acceptance. Trigger and offline jets are matched using $\Delta R < 0.4$.

Figures 4.46 and 4.47 show the response of trigger jets with respect to reconstructed jets after pileup correction and the MC-based calibration, in MC simulation and data respectively. Note, that the simulated reconstructed jets and the offline jets from data are calibrated up to the GSC step which is not available for trigger jets. The comparison between trigger and offline or reconstructed jets is good, and this is considered to be the starting point for further calibration steps.

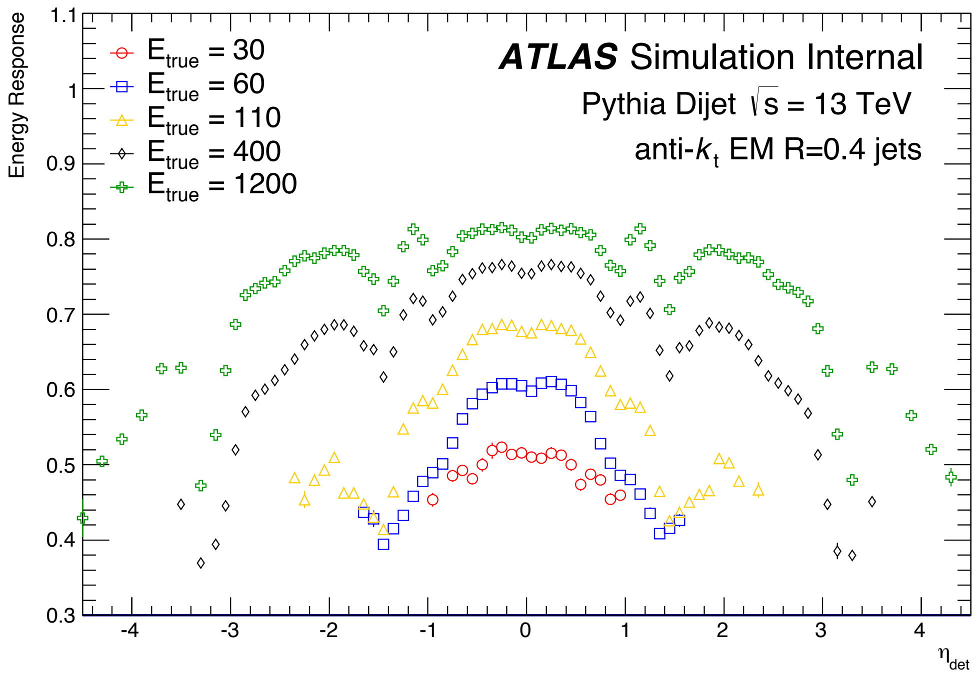

Figure 4.44: Simulated trigger jet energy response, $E_{\mathrm{T}}^{\text{measured}}/E_{\mathrm{T}}^{\text{truth}}$, after pileup subtraction but before the MC-based calibration as a function of the detector pseudorapidity, for various truth energy values. The inverse of the response shown in each bin is equal to the average jet energy scale correction for trigger jets.

Lack of GSC: This calibration step improves the jet resolution and leaves the average jet energy scale unaffected. Thus it is less important to the analysis. The GSC also includes a punch-through correction, but this is negligible correction for the p_{T} range covered by the analysis. Moreover, the uncertainty estimate is currently conservative enough to have a similar size as this correction, independent from the number of muon segments. The recommended flavor uncertainties for offline jets do not apply to trigger jets without the GSC correction, as the flavor response is changed significantly by this correction. Flavour uncertainties applicable to jets without the GSC correction are available and are used for this analysis, as detailed below. We also note that it would be possible to apply only the calorimeter part of the GSC, but as this correction has a small impact on the trigger jet resolution compared with the track correction and it would need further customisation of the calibration tool, we prefer not to apply this correction.

η-intercalibration of trigger jets: The calibration constants are obtained from the dijet balance technique, and those derived from trigger jets are compared to those derived from offline jets. After checking that the relative response in data for trigger and offline jets is

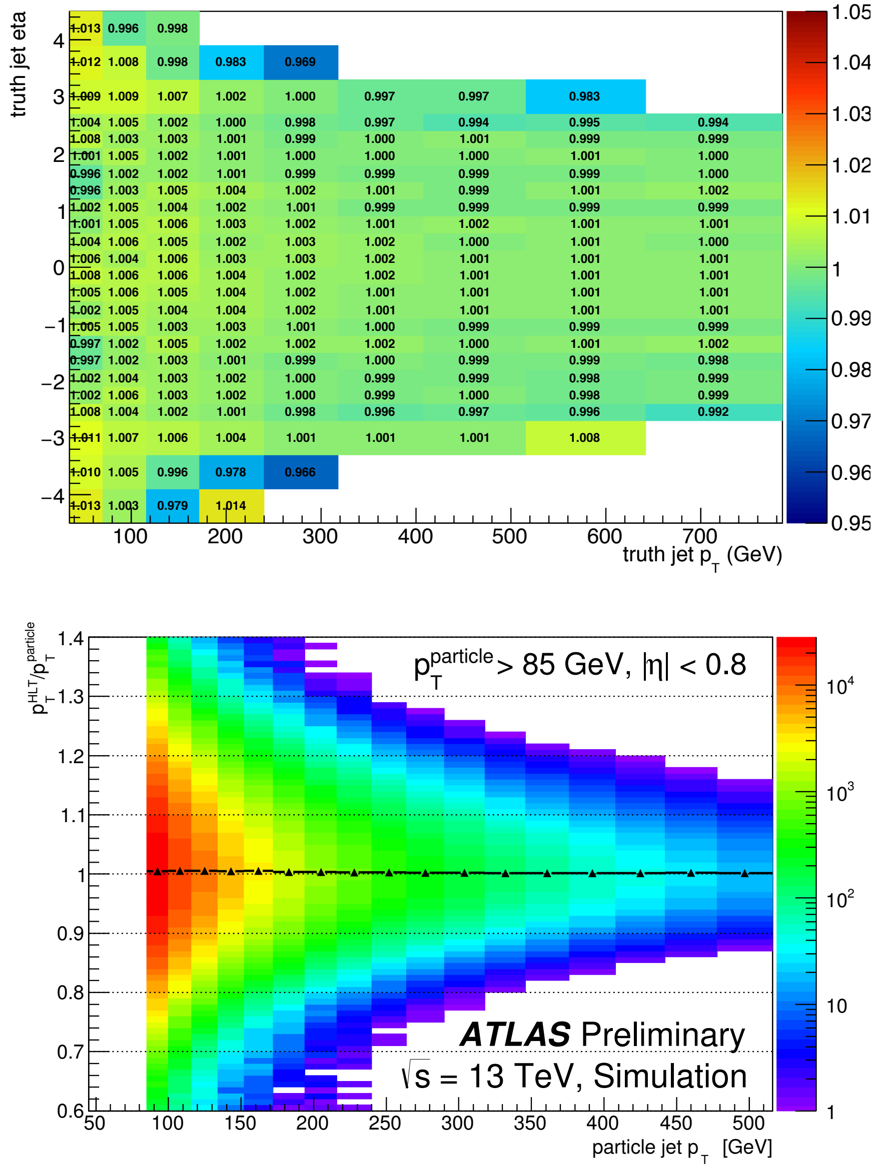

Figure 4.45: Ratio between the transverse momenta of the trigger jets (denoted as HLT) and their corresponding truth particle jets in Monte Carlo simulation, after correcting the trigger jets for pileup and applying the dedicated MC-based jet energy scale correction factors. Events are selected using any of the HLT single jet triggers. Trigger and truth jets are matched using $\Delta R < 0.4$. The z axis in the top plot gives the ratio of matched trigger and truth jet transverse momenta, and the z axis in the bottom plot is the number of jets. Each matched trigger jet in the bottom plot is required to have $p_{\mathrm{T}} > 85$ GeV and $|\eta| < 0.8$.

within 2% of each other for most of the kinematic range of the analysis (shown for example for the p_{T} bin in figure 4.48), and that they are compatible within systematic and statistical

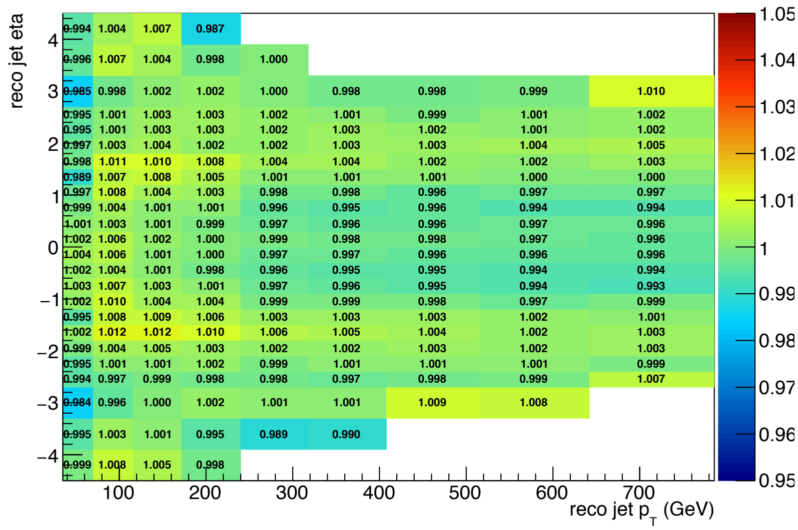

Figure 4.46: Ratio between the transverse momenta of the trigger jets and their corresponding reconstructed offline jets in Monte Carlo simulation, after correcting trigger jets for pileup and applying dedicated MC-based jet energy scale correction factors. Events are selected using any of the HLT single jet triggers. Trigger and offline jets are matched using $\Delta R < 0.4$. The offline reconstructed jets are calibrated up to the GSC step.

uncertainties, the offline jet constants are used to calibrate the trigger jets. This choice is made because the intercalibration for trigger jets does not include the Jet Vertex Tagger cut which rejects pileup jets, nor the residual pileup correction which would bring the jet back to the hard scatter energy. Since the dijet topology required in the eta intercalibration analysis is sensitive to third jet radiation and to increased pileup energy contribution to jets in the forward region, a more stable calibration is obtained when using calibration constants that have been derived from hard scatter jets only. The calibration constants are applied directly to the trigger jets, since the bins used to derive the intercalibration corrections are large compared to the effect of this first calibration. The two exceptions to the 2% compatibility between intercalibration constants of trigger and offline jets are the two crack regions, one at $|\eta| \approx 1.4$ and the other one at $|\eta| \approx 2.4$. These two regions have known issues. At $|\eta| \approx 1.4$, the cell calibration constants are larger to compensate for higher dead material in the crack. This means that the energy scale of out-of-time pileup noise at the start of bunch trains, where there is no compensation from the negative side of the LAr pulse shape, is increased [93]. This effect is corrected offline through the pileup residual correction depending on the place of the event in the bunch train. At $|\eta| \approx 2.4$ there are pulse shape modelling issues which are again corrected by the offline intercalibration and the next step in the calibration chain of trigger jets.

The intercalibration factors from the data/MC difference of the relative calibration are

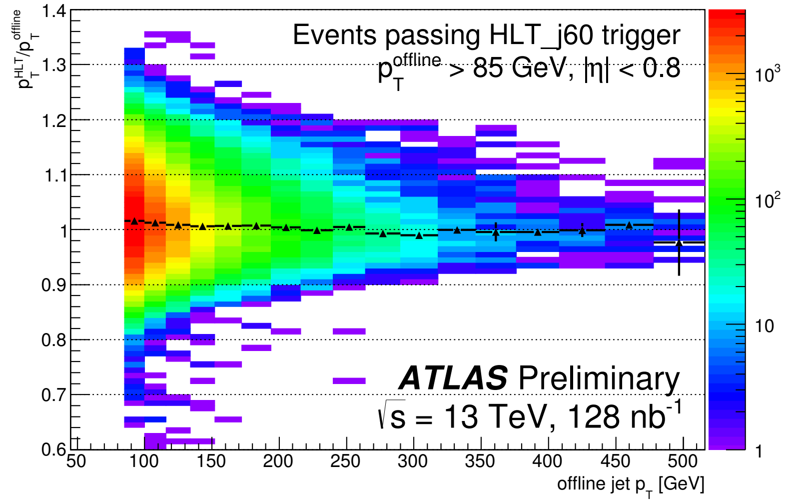

Figure 4.47: Ratio between transverse momenta of trigger (denoted as HLT) and their corresponding offline jets in data, after correcting trigger jets for pileup and applying dedicated MC-based jet energy scale correction factors. Events are selected using any of the HLT single jet triggers. Ofline jets are calibrated up to the GSC step. Trigger and offline jets are matched using $\Delta R < 0.4$. Each matched jet is required to have trigger and offline $|\eta| < 0.8$. The calibration is derived for all jets in the detector acceptance.

found to range from 1% to 5% depending on the pseudorapidity and transverse momentum of the jet, within the TLA kinematic range. An example of the calibration constants, together with the relative responses, is shown in figure 4.49.

The agreement between offline and trigger jets after the intercalibration is shown for the full 2015 dataset in figure 4.50, where trigger jets and offline jets are matched within the same event within $\Delta R < 0.4$.

Data-derived correction for trigger jets: After all calibration steps above have been applied to trigger jets, and the offline jets are calibrated up to the intercalibration stage, a data-derived correction factor for trigger jets is derived from the full 2015 dataset so that offline and trigger jets are brought to the same scale before applying the last in-situ step of the calibration chain. The dataset used to derive this correction is selected using a combination of single jet triggers which guarantees that in each p_{T} bin the selected trigger is fully efficient. No such correction is applied to jets in Monte Carlo simulation, as the agreement between trigger and offline jets is better than 1% as shown in figure 4.46. A similar procedure to the one employed in the MC-based JES calibration is applied. In data, trigger and offline

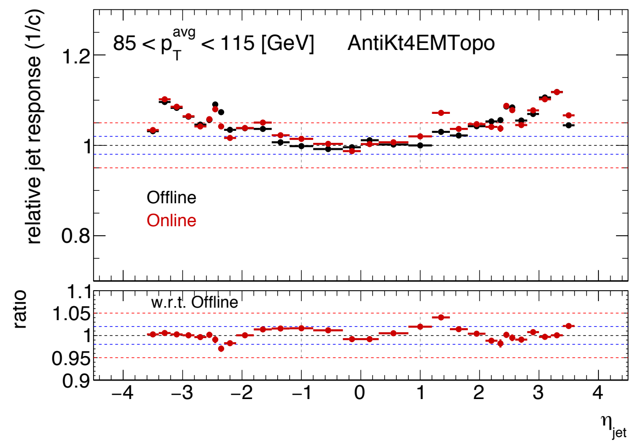

Figure 4.48: The ratio between jets in data and jets in MC. This ratio is shown in red for trigger jets (denoted as online) and in black for offline jets. All jets are calibrated until the η-intercalibration stage and are shown as a function of the probe jet pseudorapidity. Results are presented for jets with $85 \leq p_{T,avg} < 115$ GeV.

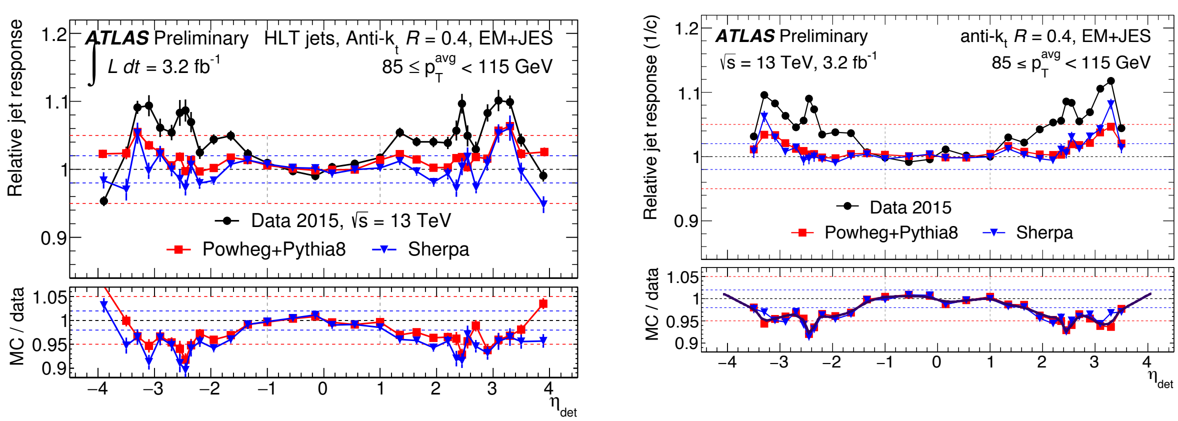

Figure 4.49: Relative jet response (1/c) for trigger jets (left plot) and for offline jets (right plot) with R = 0.4 in data and MC calibrated as a function of the probe jet pseudorapidity. Results are presented in the $85 \leq p_{\mathrm{T}}^{\mathrm{avg}} < 115$ GeV bin. The lower part of the figure shows the ratios between relative response in data and MC. After smoothing, this response ratio of offline jets is used as calibration for data.

jets are matched within the same event using $\Delta R < 0.4$. In bins of the jet with the better resolution, namely offline bins of $p_{\mathrm{T,offline}}$ and η_{offline}, the distribution of the $p_{\mathrm{T,trig}}$ is plotted and fitted to a Gaussian. The ratio between $p_{\mathrm{T,offline}}$ which is the centre of the bin used, and $p_{\mathrm{T,trig}}$ which is the mean of the Gaussian fit is plotted for each η bin as a function of $p_{\mathrm{T,trig}}$.

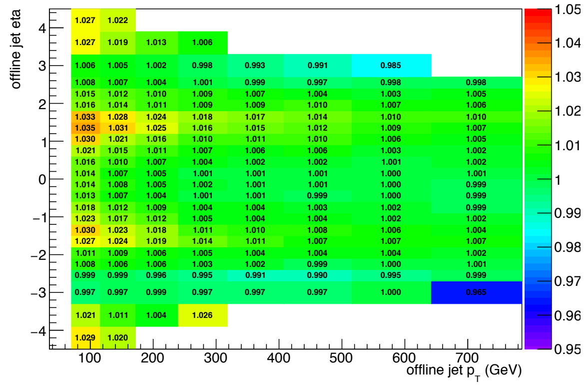

Figure 4.50: Ratio between the transverse momenta of trigger jets and their corresponding reconstructed offline jets in the full 2015 dataset, after correcting offline and trigger jets for pileup, applying dedicated MC-based jet energy scale correction factors, and applying relative intercalibration factors. Offline jets also have the GSC constants applied. Events are selected using any of the `HLT` single jet triggers and combined so that each bin only has a contribution from a trigger that is fully efficient.

In each η_{offline} bin, for each value of $p_{\text{T,trig}}$ the correction factor C is then obtained as:

$$C = p_{\text{T,offline}}/p_{\text{T,trig}}.$$

The η bins are sufficiently large (0.1) and the correction sufficiently small ($< 1.5\%$) that the correction can be directly applied in bins of trigger jet η. This correction is derived for jets with $p_{\text{T}} < 1$ TeV and $|\eta| < 2.8$, within this kinematic range of the TLA. For jets with $p_{\text{T}} > 1$ TeV, the correction is frozen to the value used for $p_{\text{T}} = 1$ TeV, and for jets outside the η range the correction is set to unity. These restrictions are applied to avoid biases on the correction factor arising from limited statistics in the forward region, and to avoid being dependent on the fitting procedure in regions where the correction is expected to be small (> 1 TeV), and in any case they do not affect the jets in the analysis acceptance. The correction factors applied to trigger jets are shown in figure 4.51.

Residual in-situ correction: This step of the calibration is done in the same manner as for the offline jets.

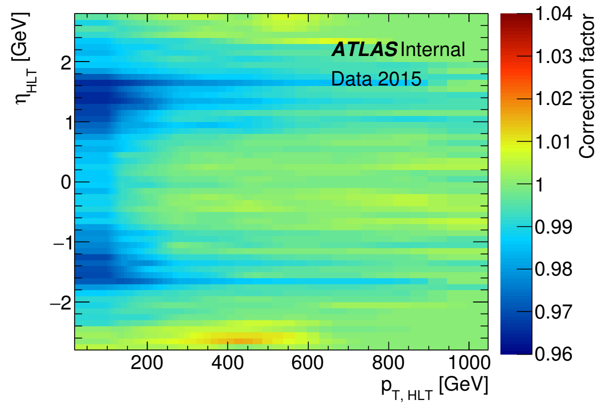

Figure 4.51: Data-derived correction applied to trigger jets, in bins of trigger jet p_T and η.

Trigger jet energy scale uncertainty

After the application of the scale factor derived as above, trigger and offline jets in both data and MC are at the same scale. The offline jet uncertainties are applied to trigger jets, as described in Ref. [94] with the following differences:

1. A conservative uncertainty that is as large as the data-derived correction itself is applied to trigger jets in Monte Carlo, to cover for possible miss-calibrations and differences between data and Monte Carlo.
2. Since GSC correction is not available for trigger jets, the JES uncertainties for jets without the GSC correction are applied to trigger jets.

The total JES uncertainties for trigger jets are shown in figure 4.52. The propagation to the analysis is done via the same nuisance parameters as the high-mass dijet search, with the addition of two separate nuisance parameters, one for the in-situ correction factor and one for the non-closure of the eta intercalibration for offline jets in the region around η=2.4.

Validation of the trigger jet energy scale

The final closure test, binned in offline jet p_T, for the whole calibration chain is shown in figuers. 4.53 and 4.54 where the full calibration chain is applied to trigger and offline jets. The final analysis distributions will be binned in trigger jet kinematic quantities. It is

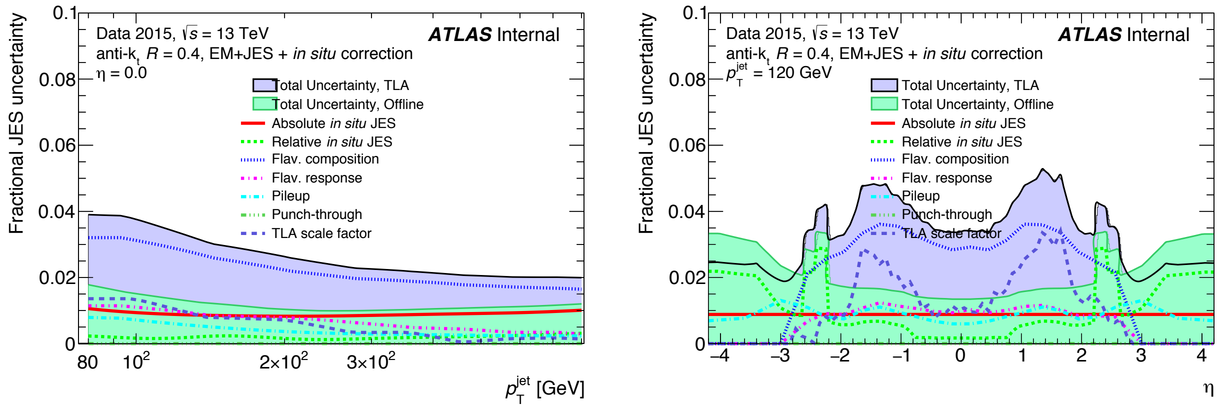

Figure 4.52: Jet energy scale uncertainties for trigger jets as a function of p_{T} in the central region (η=0) on the left and as a function of η for jets with p_{T} = 120 GeV on the right, compared to the offline jet energy scale uncertainties.

therefore worth checking the effect of the potential trigger jet resolution bias when deriving the calibration. The jet p_{T} used for the binning is chosen randomly between trigger and offline jets. The results of this test are shown in figures. 4.55 and 4.56.

By showing that in both closure tests trigger and offline jets agree to better than 1% across the TLA kinematic range, a value well covered by the jet energy scale uncertainties, we are confident that we can use trigger jets for physics analysis with the same jet energy scale and comparable uncertainties as offline jets.

Conclusions

The calibration strategy has been modified for the use of trigger jets to account for the lack of information outside the calorimeters. The calibration strategy applied to trigger jets and relative uncertainties are not yet appropriate for precision measurements, but they are suitable for a search with a data-driven background estimation where only deviations from smoothness are relevant for the search phase, and where the jet energy scale uncertainty does not play an important role.

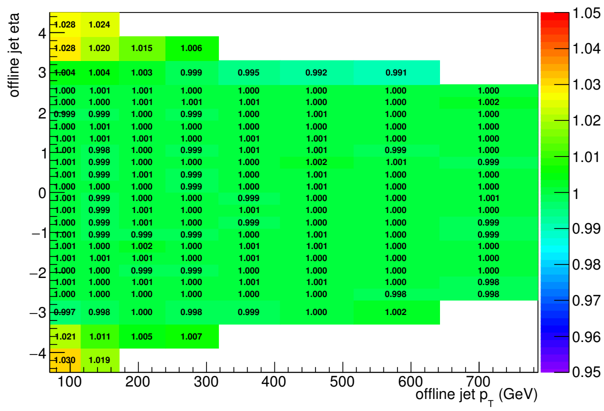

Figure 4.53: Final comparison of trigger jets and jets reconstructed offline in the full 2015 dataset, using the ratio of transverse momenta of jets matched within ΔR <0.4. The respective full calibration chain is applied to both trigger and offline jets. This plot is binned in offline jet p_{T}. Only jets with $|\eta|$ <2.8 are used for analysis.

4.3.8 Trigger jet reconstruction efficiency

The reconstruction efficiency for trigger jets is determined using a tag-probe method with dijet events. Events are required to pass the `HLT` single-jet trigger of [60 GeV, 100 GeV, 200 GeV, 300 GeV, 360 GeV] as well as the basic data-quality criteria as outlined in Section 4.3.4. The kinematic criteria specific to this study require that dijet events are selected if there are at least two offline jets in the event with $|y^*| < 0.6$ and at least one trigger jet. Offline jets in the event must have a $p_{\mathrm{T}} > 50$ GeV and $|\eta| < 2.8$.

The tag jet is defined as the offline jet, which matches within $\Delta R < 0.4$ to the trigger jet that fired the trigger. If there is more than one jet which passes this criteria in the event, then one of these jets is randomly chosen as the tag jet. Randomly choosing the tag jet instead of, for example, always selecting the highest p_{T} jet, reduces biases in determining the reconstruction efficiency from effects such as gluon radiation or detector resolution. The probe jets are defined as any other offline jet in the event passing the selection criteria above.

The reconstruction efficiency is determined as the number of probe jets that are matched within $\Delta R < 0.4$ to a trigger jet divided by the total number of probe jets found. Figure 4.57 shows this efficiency as a function of the offline jet p_{T} for both data and MC corresponding to the `HLT` single-jet trigger threshold of 100 GeV on the right plot and of 360 GeV on the left plot. The `HLT_j100` plot shows an efficiency well above 99.9% while the `HLT_j360` is more than 99.8% efficient, within the larger statistical errors due to the limited statistics.

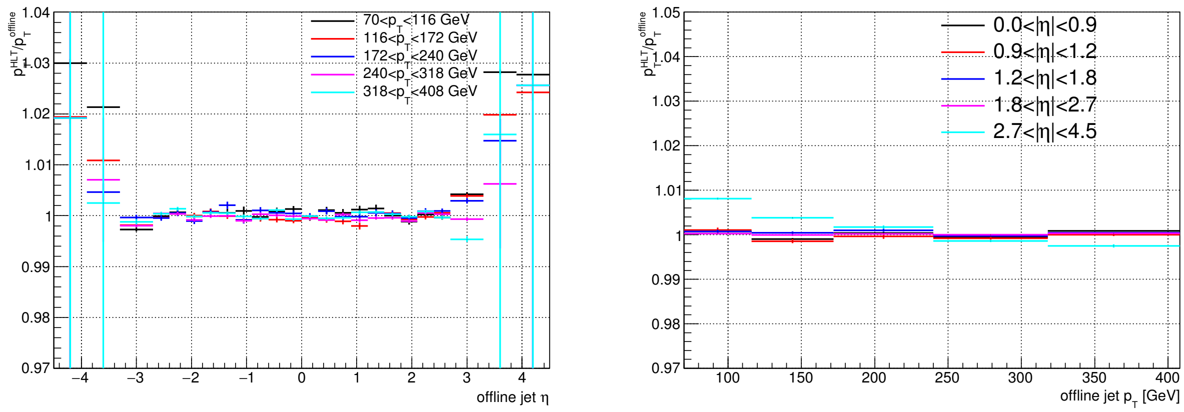

Figure 4.54: Final comparison of trigger jets and jets reconstructed offline in the full 2015 dataset, using the ratio of transverse momenta of jets matched within ΔR <0.4, plotted as a function of jet p_{T} and η. The respective full calibration chain is applied to both trigger and offline jets. This plot is binned in offline jet p_{T}. Only jets with $|\eta|$ <2.8 are used for analysis.

The overall difference between data and MC is less than 0.1%. This conclusion applies for all triggers tested.

4.3.9 Analysis method

The m_{jj} distribution is being searched for local excesses, where the QCD background is represented by a smooth function. The QCD MC is not used for the background estimation since it has large uncertainties. The smooth function is obtained from a fit to the dijet mass distribution using the best fitted function, $f(x)$, out of various options gathered over the years as those most suitable for this kind of searches, where $x \equiv \frac{m_{\mathrm{jj}}}{\sqrt{s}}$. All the options are summarised in table 4.4.

Note, that this kind of fit can accidentally accept as background a smooth deviation from the true background such as those caused by CI, thus it is only useful to find local resonances.

To take into account the possibility of none of these function successfully fitting to the data distribution, a different approach of fitting the data was also considered. The sideband method, documented in [100], is using a window of few bins referred to as signal area, surrounded in both of its sides by a range of few bins referred to as background region. This window is set in the lowest possible range of the distribution and the bins falling in the right and left background regions are fitted ignoring the bins falling in the signal region. The

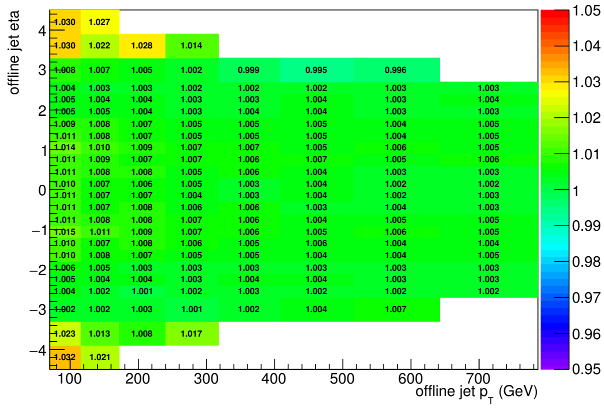

Figure 4.55: Final comparison of trigger jets and jets reconstructed offline in the full 2015 dataset, using the ratio of transverse momenta of jets matched within ΔR <0.4. The respective full calibration chain is applied to both trigger and offline jets. This plot is binned in offline jet p_{T} Only jets with $|\eta|$ <2.8 are used for analysis.

Functional form	Citation	Label
$f(x) = p_1(1-x)^{p_2}x^{p_3}$	[10]	our3param
$f(x) = p_1(1-x)^{p_2}x^{p_3+p_4\ln x}$	[95, 96]	our4param
$f(x) = \frac{p_1}{x^{p_2}}e^{-p_3x-p_4x^2}$	[97]	UA2
$f(x) = p_1(1-x^{1/3})^{p_2}x^{-p_3}$	[98]	Multijet9
$f(x) = (1-x^{1/3})^{p_1}x^{-p_2-p_3\ln(x)}$	[99]	GammaGamma3ParThird
$f(x) = (1-x^{1/3})^{p_1}x^{-p_2-p_3\ln(x)^2}$	[99]	GammaGamma4ParThird

Table 4.4: Functional forms explored for fitting the QCD background, with citation to previous analyses in which they have been used to fit similar distributions and label for reference in the rest of the text.

window is then shifted by one bin at a time and the fitting process is repeated. The value of the background estimation in each bin is then determined by the fit obtained while it was falling in the background region. This method was finally not used as one of the overall fit functions always gave a good outcome.

After the fit is chosen and the background estimation is done, an excess is searched and quantified using the BumpHunter algorithm [38]. The algorithm compares the binned m_{jj} distribution of the data to the fitted background estimation, considering contiguous mass intervals in all possible locations, from a minimal width of two bins to a maximal width of half of the total mass range being explored. For each interval in the scan, it computes the significance of any excess found.

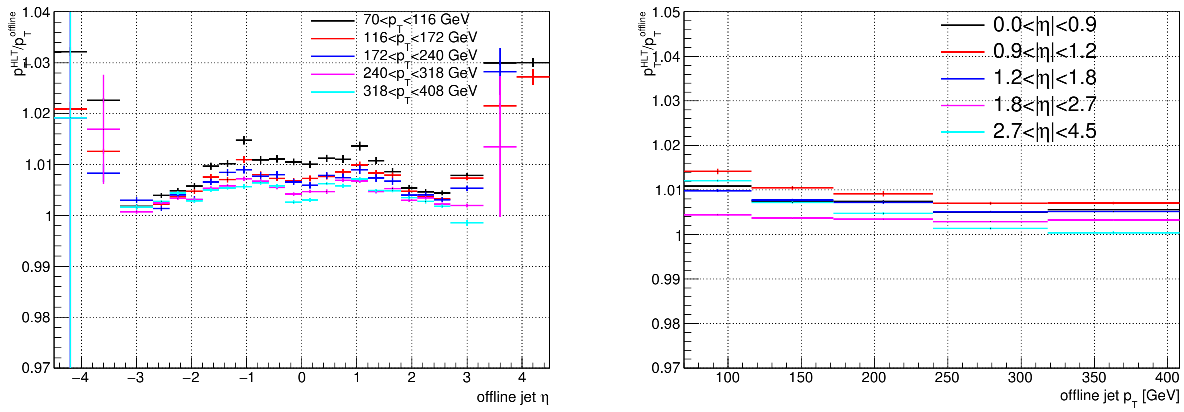

Figure 4.56: Final comparison of trigger jets and jets reconstructed offline in the full 2015 dataset, using the ratio of transverse momenta of jets matched within ΔR <0.4, plotted as a function of jet p_{T} and η. The respective full calibration chain is applied to both trigger and offline jets. This plot is randomly binned in either trigger or offline jet p_{T}. Only jets with $|\eta|$ <2.8 are used for analysis.

Systematic uncertainties on the estimate of the background to the search arise from imperfect knowledge of the shape of the m_{jj} distribution. To account for the statistical uncertainty on the fitted parameters in the `UA2` function, a large number of pseudo-experiments are performed, fitting pseudo-data drawn from Poisson fluctuations around the nominal background model. The uncertainty on the background prediction in each m_{jj} bin is taken to be the root mean square of the function value in that bin for all pseudoexperiments. To account for the choice of the function used in the fit, the alternative parameterization of the `our4param` function, which is the function with the second-largest probability, is compared to the nominal fit. The mean difference between the two results as calculated over a range of pseudoexperiments is taken as the uncertainty. Statistical uncertainties and uncertainties on the jet energy scale of trigger jets are included when setting limits on the signal models considered while the impact of the uncertainty on the jet energy resolution is negligible. The jet energy scale uncertainty is treated using a set of nuisance parameters and accounting for the effect of each on the signal Monte Carlo. The uncertainty on the integrated luminosity is 5%. It is derived from a preliminary calibration of the luminosity scale using a pair of x-y beam-separation scans performed in June 2015.

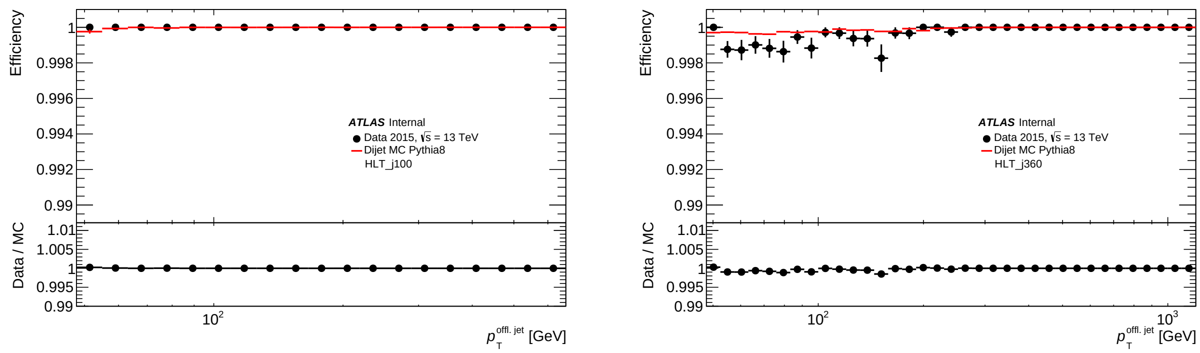

Figure 4.57: The reconstruction efficiency for trigger jets passing the HLT single-jet triggers with thresholds of 100 GeV (left) and 360 GeV (right) as a function of the offline jet energy.

4.3.10 Results

Figure 4.58 reveals the final unblinded reconstructed dijet mass distribution using the full 3.5 fb^{-1} of 2015 data for both the $|y^*| < 0.3$ and $|y^*| < 0.6$ spectra. The bottom panel in each plots shows the bin-to-bin significances differences [39] between the data and the fit, calculated from the Poisson probability, considering only statistical uncertainties. The UA2 function was chosen as the nominal background description. This is in keeping with the results found in Monte Carlo, where 70% of fits to background-only spectra exhibited a preference for this fitting function. The $|y^*| < 0.3$ spectra is fitted from m_{jj}=394 GeV, while the $|y^*| < 0.6$ spectra is fitted starting from m_{jj}=443 GeV. According to the results of the BumpHunter, the probability of observing a background fluctuation at least as significant as that observed in data, anywhere in the distribution, is 0.44 for the mass distribution with $|y^*| < 0.6$ and 0.19 for the mass distribution with $|y^*| < 0.3$, corresponding to 0.15 σ and 0.88 σ, respectively, taking only statistical uncertainties into account. This is in good agreement with the SM and shows no indication of new physics in the form of an anomalous localised contribution in either selection.

With no concrete evidence for new physics, the data can be used to set limits on specific theoretical models. The expected limits are calculated using pseudo-experiments generated from the maximum-likelihood values for parameters of the background-only model in the UA2 fit function and using the full systematic uncertainties described section 4.3.9, in both the signal and background models. A Bayesian method [25] was applied to the m_{jj} distributions obtained using data and simulation of signals at a series of discrete masses to set 95% credibility-level upper limits for the signals which will be described to follow. The method uses a constant prior for signal cross-section and Gaussian priors for nuisance parameters corresponding to systematic uncertainties.

Following the approach described in section 2, a leptophobic Z' simplified model [101] was chosen for this purpose. Consistently with the model studied in [10], the Z' model assumes axial-vector couplings to SM quarks and to a Dirac fermion dark matter candidate. No interference with the SM is simulated for this model. The Z' model considered follows a scenario [102] where its decays to dark matter particles are negligible, hence the dijet production rate and resonance width depend only on the coupling to quarks, g_{q}, and the mass of the resonance $m_{Z'}$. The acceptance $\mathcal{A}$ varies for the different selection cuts, for example: for the analysis selection with $|y^*| < 0.3$, $\mathcal{A}$ =20% for a Z' mass of 550 GeV with $g_{\mathrm{q}} = 0.15$. For the case of $|y^*| < 0.6$, $\mathcal{A}$ =40% for a Z' mass of 650 GeV and $g_{\mathrm{q}} = 0.15$. The model's matrix elements are calculated in `MadGraph` 5 [22] and parton showering is performed in `Pythia` 8.

Limits are also provided for a possible signal that produces a Gaussian contribution to the observed m_{jj} distribution. For sufficiently narrow resonances, these results may be used to set limits on models of new phenomena beyond those considered explicitly in this result. Such limits should be used when parton distribution function and nonperturbative effects can be safely truncated or neglected. These limits are applicable if the m_{jj} distribution for a signal approaches a Gaussian distribution after applying the kinematic selection criteria of the resonance analysis. Models of new resonances with an intrinsic width much smaller than 7% should be compared to the results with a width equal to the experimental resolution. For models with a larger width after detector effects, the limit that best matches their width should be used. For model-independent limits on Gaussian shapes, a flat jet energy scale uncertainty of 3% is applied in accordance with the measured impact of this uncertainty on the Z' samples.

Figure 4.59 shows limits on the coupling to quarks g_{q} as a function of the mass $m_{Z'}$ for the Z' model. Coupling values above the solid curves are excluded. Figure 4.60 show limits on a possible Gaussian contribution to the observed m_{jj} distribution obtained for a mean mass m_{G} and three different widths; a width equal to the detector mass resolution as well as equal to 7% and 10% of m_{G} are chosen. Limits for a given signal region are set for m_{G} values above the starting point of the fit and separated from the endpoints of this range by at least the width of the Gaussian. As the width increases, the expected signal contribution is distributed across more bins. Wider signals are thus less affected by statistical fluctuations of the data in a single bin.

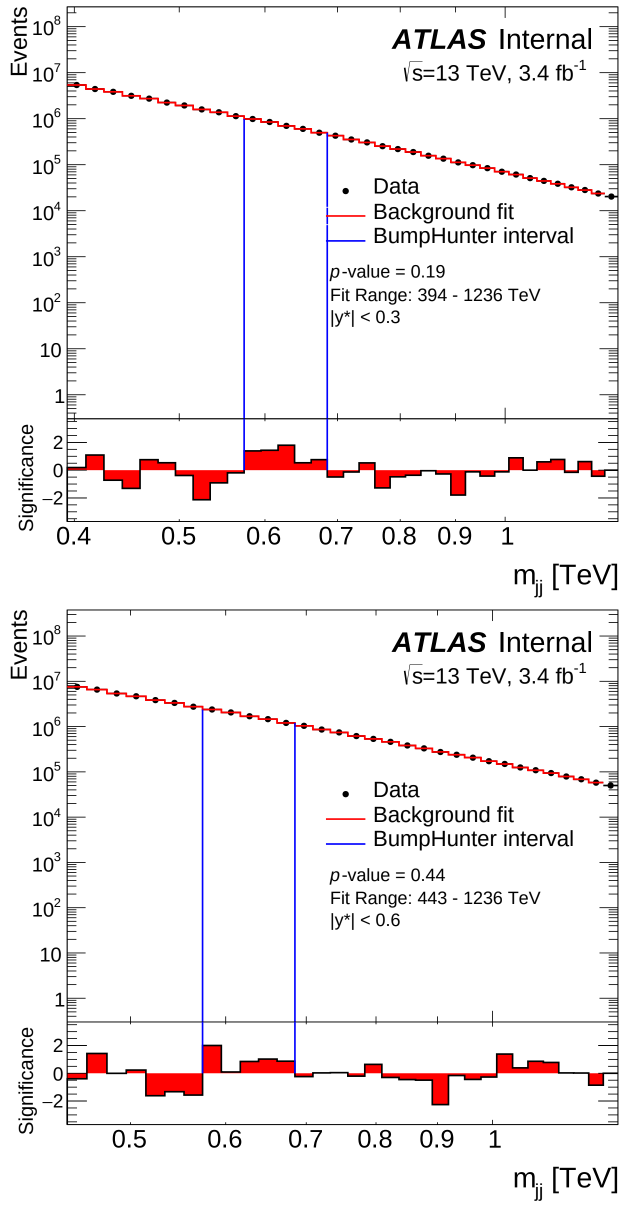

Figure 4.58: The reconstructed dijet mass distribution (black points) in the full 2015 dataset corresponding to 3.5 fb^{-1} of data. The top (bottom) plot show events with $|y^*| < 0.3(0.6)$. The solid line is the fit to the `UA2` function. The vertical lines indicate the most discrepant interval identified by the `BumpHunter` algorithm, for which the p-value is stated in the figure.The bottom panel in each plots shows the bin-to-bin significances differences between the data and the fit,

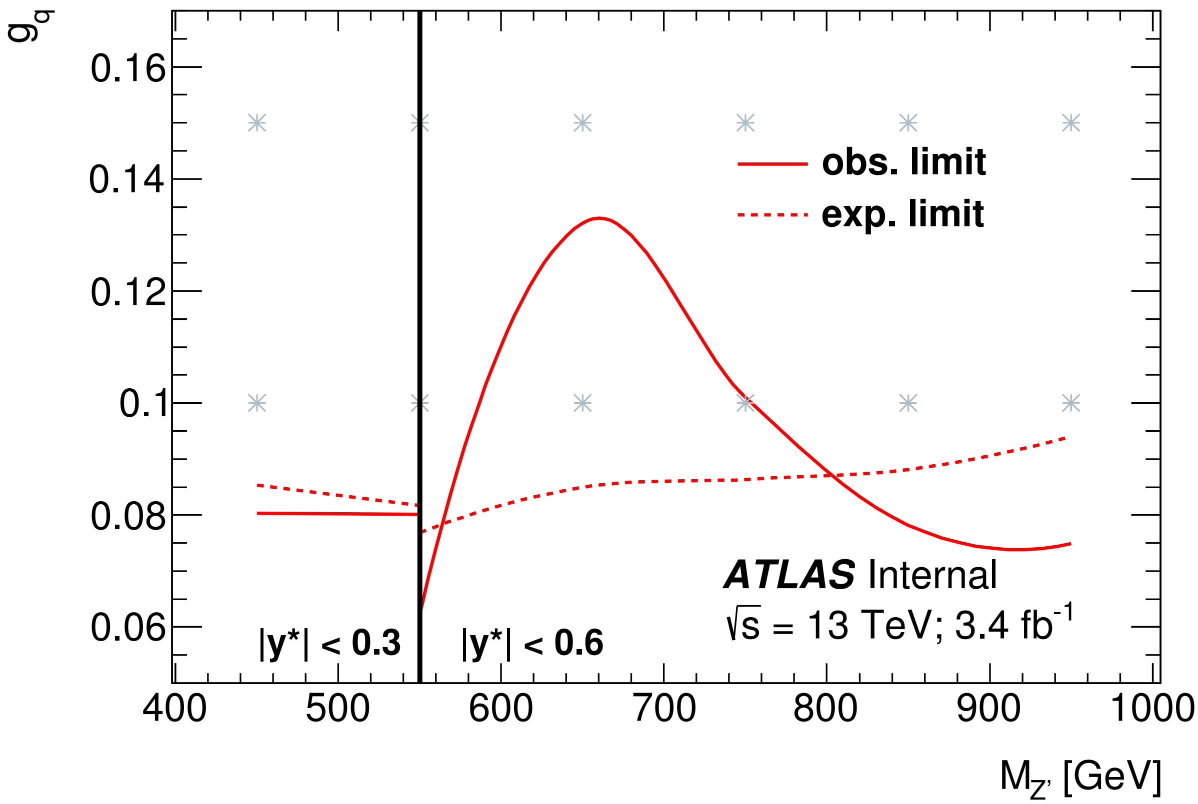

Figure 4.59: The 95% credibility-level upper limits on the coupling to quarks, g_q, of a Z' boson in the model described in the text. The solid (dashed) lines represent the observed (expected) values, and they were obtained by interpolation between the simulated discrete mass and coupling values represented by the star markers. Limits for mass points including and above 500 GeV are obtained from the dijet mass distribution with the cut $|y*| < 0.6$, while for the mass points around 450 GeV, the cut $|y*| < 0.3$ is used. Note that, while the y-axis is shared between the two selections, the acceptance is different, thus the plots in the two mass regions cannot be directly compared.

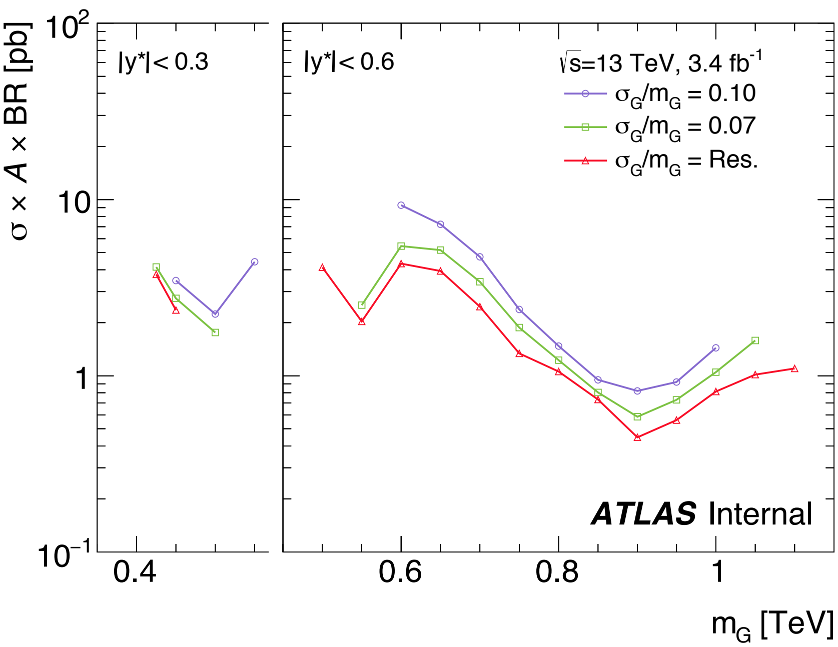

Figure 4.60: The 95% credibility-level observed upper limits for a hypothetical signal with width σ_G that produces a Gaussian contribution to the observed $m_{\rm jj}$ distribution, as a function of the mean mass of the Gaussian distribution, m_G. Limits are obtained for three different widths, from a width equal to the detector mass resolution ("Res."), to a width of 10% of the mean of the Gaussian mass distribution. For all mass points to which the nominal $|y^*| < 0.6$ distribution is sensitive, it is selected to define the limit shown. Lower mass points accessible only to the $|y^*| < 0.3$ spectrum are shown on the left. A range of mass points spanning [425 GeV, 1100 GeV] are thus covered using the combination of the two spectra. While the y axis is shared between the two selections, the signal acceptance varies, thus the plots in the two mass regions cannot be directly compared.

Chapter 5

TGC Quality Tests

Thin Gap Chambers (TGC) are used to provide triggering on muons in the endcaps region of the ATLAS detector muon spectrometer, as was described in section 3.2. The TGC are multi-wire proportional chambers constructed such that there is a 1.8 mm gap between each two wires and a 1.4 mm gap between a wire and a strip [103, 104].

There are approximately 3600 TGC in ATLAS, and two thirds of them were produced at WIS and were tested in a joint effort of TAU and the Technion, before they were first installed in ATLAS. After three years of use, 29 chambers needed to be replaced, so in 2013 new chambers were constructed at WIS. Quality tests for these new chambers were preformed at the TAU laboratory with a hodoscope providing space coordinates of cosmic rays, using precision chambers, which are of a similar kind. A tested TGC unit is placed in the middle of the hodoscope, where the location of a muon passing through can be interpolated from the hits in the precision chambers with a precision of less than four millimetres. The quality test looks for corresponding signal produced by the tested chambers. The chamber is considered to be operational if its efficiency exceeds 95% in at least 95% of its effective area [105, 106].

The hodoscope, shown in figure 5.1 consists of three major components:

1. Trigger system based on plastic scintillators in the uppermost and lowermost layers, which are read out by sixteen Photo-Multiplier Tubes (PMT), eight in each layer. The PMTs are connected to a NIM logic system, requiring logic OR gate between PMT in the same layer, and a logic AND between the two layers.

2. Two Precision Chambers (PC), giving a two dimensional coordinates of a muon passing through. The upper is referred to as PC0, and the lower PC1. The PC have two layers of strips placed lengthwise and crosswise, and in between one layer of wires. The strips

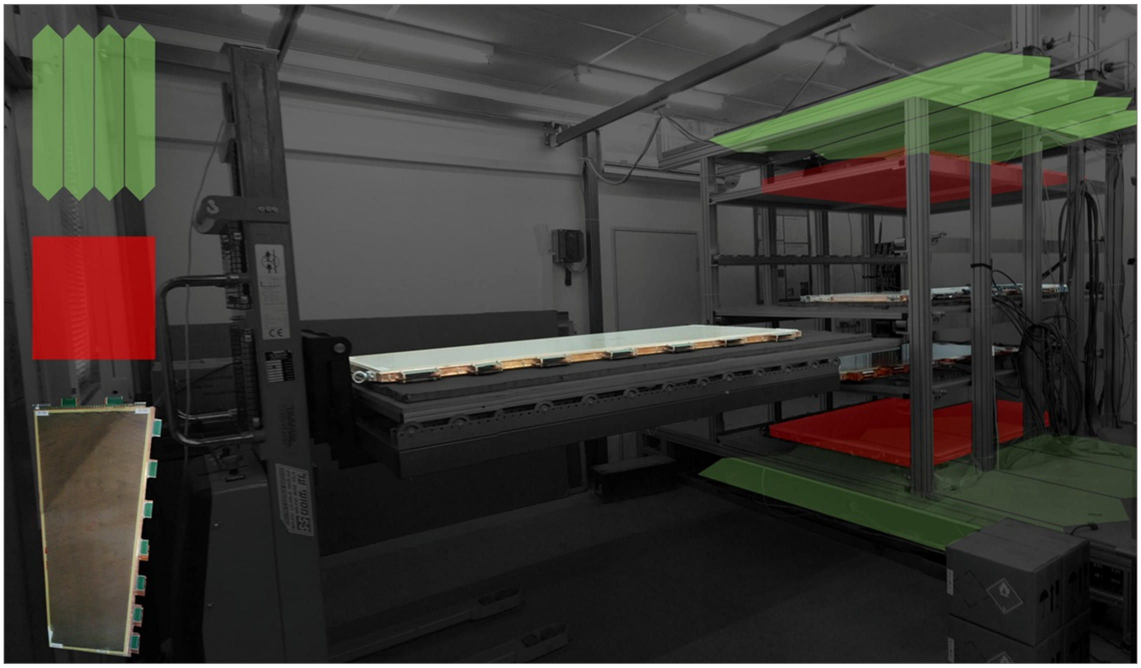

Figure 5.1: TAU testbench. The PMT based trigger system marked in green, the two Precision Chamber marked in red, and the three tested TGC are in white.

in both directions are connected with a Gassiplex chip readout system to an online VME ADC and a sequencer. Thus the current arriving to each strip is translated to a voltage readout in a correlated output channel.

3. TGC - the tested chambers raw signal goes via Amplifier Shaper Discriminator (ASD) chip and read by a VME TDC unit. All Wires in a TGC are divided into four or six groups (depending on the TGC size). In each group the wires are connected with a logic OR to two readout channels. In each chamber there are up to 14 wide strips, each one is connected to a separate readout channel.

The offline analysis is aimed to identify the muon passing through both precision chambers, and to measure its position coordinates in the PCs and in the tested chamber. An event is defined by the trigger. As a first step we wish to minimize the effect of the PC noise. This is done in two ways:

1. An entire test run (500K events) is searched for noisy channels in the PC. These are channels which give signal for more than 60% of the events. The signals from such channels were not considered in the analysis, since their noise level is too high. Figure 5.2 show the channels readout from both the upper and lower PC, in such test run. One can spot two noisy channels in PC0, for which there are a lot more entries than expected. These channels have been removed from the analysis.

2. An offline threshold of a PC signal, such that any strip giving a signal below a certain value is ignored.

After noise cleaning, we look at each precision chamber and search for events in which a muon signal is shown. The signal is distributed in several adjacent channels according to an approximate Gaussian distribution, defined as a cluster. We have constructed several cuts to make sure that such a cluster represents one muon: We look only at events with one peak (to avoid events with more than one muon), with a cluster width larger than three and smaller than 10 channels, and with a maximum signal height of 0.48 V. We perform Gaussian fits to these signal distributions, and set the coordinates of the muon to be the mean of these Gaussians. Next we look only at events with a muon giving such a signal in x and y coordinates in both the top and the bottom precision chambers.

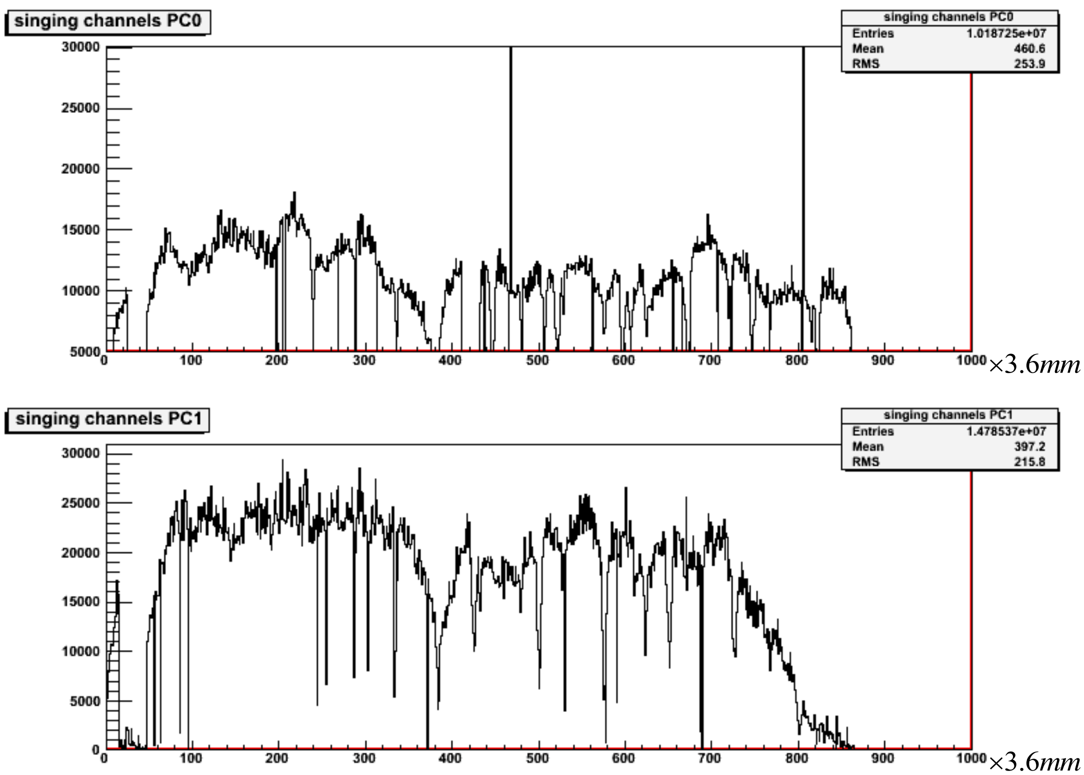

Figure 5.2: The channels readout from the upper and lower PC.

Figure 5.3 shows a summary of the process of obtaining a single coordinate of the hit in a precision chamber from the initial readout of the PC channels. The top plot shows the voltage readout from channels corresponding to the y coordinate in PC0 for a specific event. The middle plot shows the same readout ignoring channels with low value of voltage, considered as noise, and the bottom plot shows the same readout along with a Gaussian fit.

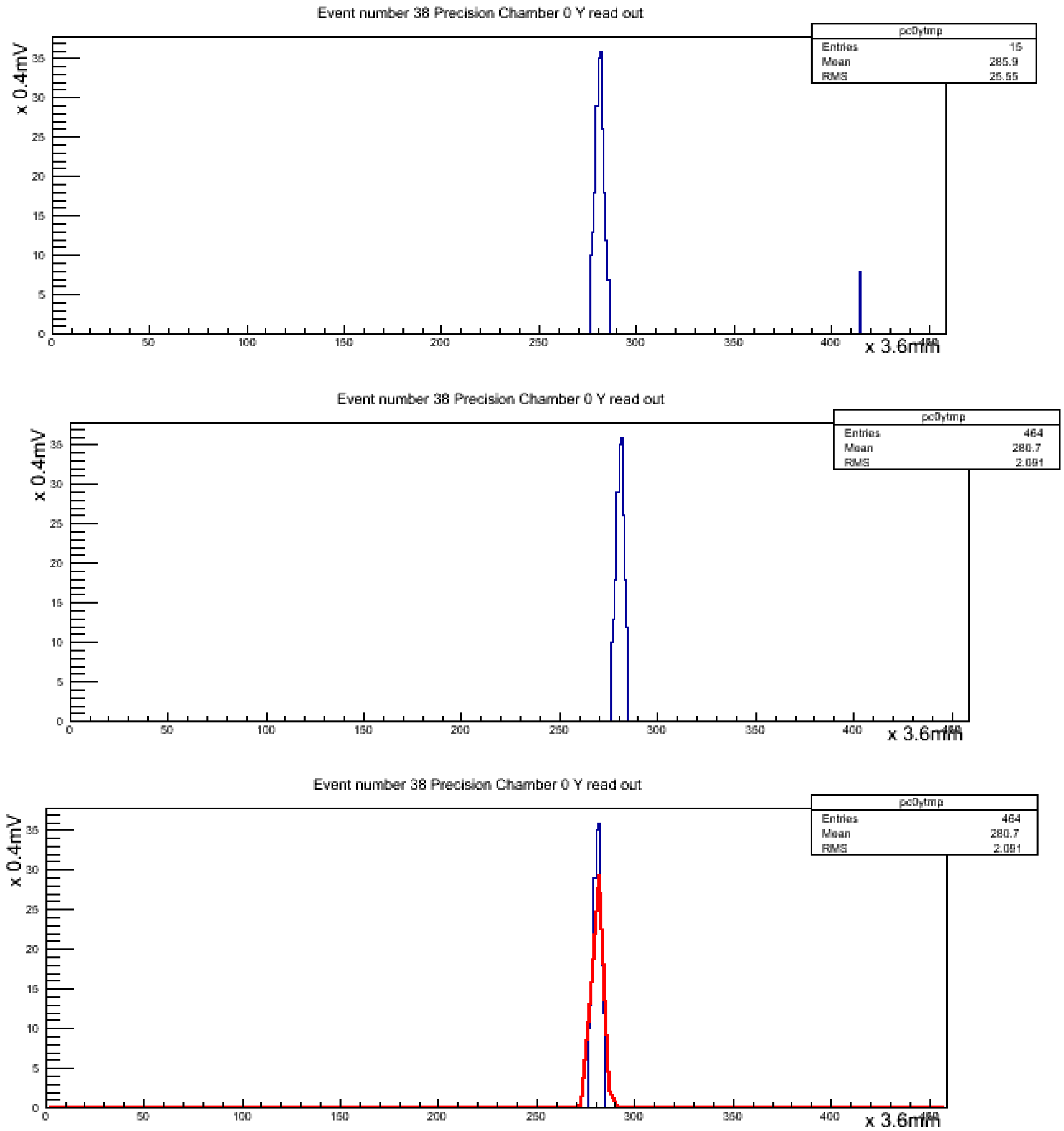

Figure 5.3: An example for the process of identifying a signal in the PC. The top plot shows the voltage readout from channels corresponding to the y coordinate. The middle plot shows the same readout ignoring channels with low value of voltage considered as noise. The bottom plot shows the same readout along with a Gaussian fit.

We then estimate the coordinates of the muon in the tested chamber plane and look for a signal in at least one of the wires or strips of each unit of the tested chamber. Only three quarters of the events identified in both precision chambers show signals in the chambers, mainly because the area of the tested unit is smaller than the area covered by the precision chambers. Figure 5.4 shows the efficiency maps of different areas of the chambers. The efficiency in each unit cell (of 1cm^2) is calculated as the fraction of events which gave a signal in this unit cell out of all events which were calculated to pass through this area unit. These efficiency plots clearly show the shape of the active area of the detector, and the inefficient areas such as the support lines and buttons placed inside the chamber to keep the uniformity of its gap width.

Table 5.1 shows the cutflow of events in percentage. The percentage of events with identified muons in both precision chambers is higher than the value measured seven years ago during the previous TGC test. As a typical run with 500K events passing the PMT trigger takes six hours, we can produce an efficiency map with 1M events passing both PC during a runtime of 24 hours.

Cut PC	PC0	PC1
All events	100%	100%
Events with entries in both x and y	74%	95%
Events with only one peak	65%	84%
Events with clusters with width > 3 ch	61%	79%
Events with clusters with width < 10 ch	59%	77%
Events with max value < 0.48 V	57%	75%
Events passing both PC cuts	45%	
Events with a signal in the TGC	32%	

Table 5.1: Testbench event cutflow

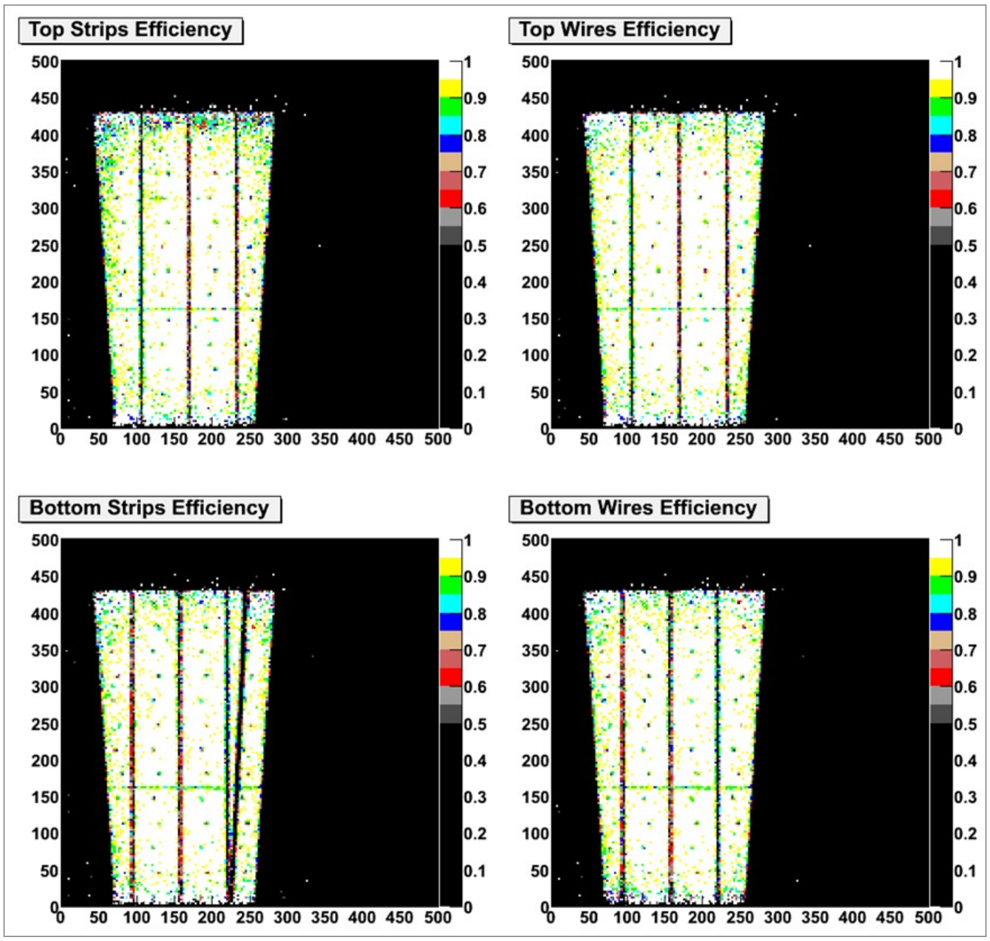

Figure 5.4: An example for a doublet TGC efficiency plot. The two upper plots are for the top unit of the chamber and the lower is for the bottom unit. The two right plots are for the wires and the left two are for the strips. The efficiency is expressed in color code between 0 to 1 following the key on the right. In the bottom unit one can spot a missing strip.

Chapter 6

Epilogue

It is has been a great privilege to work as part of the ATLAS experiment. It is a joint effort of thousands of people coming from different backgrounds conducting a ground breaking experiment which allows a glimpse at the unknown region of the experimental particle physics field. In such great experiment it is hard and sometimes seems impossible to identify one's contribution to the effort, and the work presented in this thesis is the outcome of cooperation with many people.

The TGC validation procedure was accomplished within a few months and allowed an efficient replacement of the damaged chambers by the newly produced chambers which are still working nowadays. The simplified models which we have looked at are already in use as benchmarks models to set limits on. Even though hints for NP were not shown in any of the LHC experiments and specifically the various dijet analyses in ATLAS, there are some great accomplishments the dijet team can be credited for: First, new and improved limits have been set on various models contributing to the understanding of the physics beyond the SM. Since the 8 TeV angular analysis has been finalised approximately two years after the dijet mass resonance search it is now a part of the analysis available toolset, and the 13 TeV mass and angular analyses have been published together, and are aimed to be published together also in the next runs. The TLA was used for the first time in ATLAS and showed a good proof of concept and feasibility. There is a great future potential for this method, also for complementary analyses to the dijet one such as b-tagged dijets, but also considering many other searches.

Though this is the end of my work, it is just the beginning for the LHC and its various experiments, and the search for NP will carry on.

Bibliography

[1] L. Evans and P. Bryant, "LHC Machine," *Journal of Instrumentation*, vol. 3, no. 08, p. S08001, 2008.

[2] ATLAS Collaboration, "Observation of a New Particle in the Search for the Standard Model Higgs Boson with the ATLAS Detector at the LHC," *Phys. Lett.*, vol. B716, pp. 1–29, 2012.

[3] CMS Collaboration, "Observation of a New Boson at a mass of 125 GeV with the CMS Experiment at the LHC," *Phys. Lett.*, vol. B716, pp. 30–61, 2012.

[4] J. Abdallah *et al.*, "Simplified Models for Dark Matter and Missing Energy Searches at the LHC," 2014.

[5] J. Abdallah *et al.*, "Simplified Models for Dark Matter Searches at the LHC," *Phys. Dark Univ.*, vol. 9-10, pp. 8–23, 2015.

[6] ATLAS Collaboration, "Search for New Phenomena in the Dijet Mass Distribution updated using 13.0 fb^{-1} of pp Collisions at $\sqrt{s} = 8$ TeV collected by the ATLAS Detector," Tech. Rep. ATLAS-CONF-2012-148, CERN, Geneva, Nov 2012.

[7] ATLAS Collaboration, "Search for New Phenomena in the Dijet Mass Distribution Using pp Collision Data at $\sqrt{s} = 8$ TeV with the Atlas Detector," *Phys. Rev.*, vol. D91, no. 5, p. 052007, 2015.

[8] ATLAS Collaboration, "Search for New Phenomena in Dijet Angular Distributions in Proton-Proton Collisions at $\sqrt{s} = 8$ TeV Measured with the ATLAS Detector," *Phys. Rev. Lett.*, vol. 114, no. 22, p. 221802, 2015.

[9] ATLAS collaboration, "Search for Light Dijet Resonances with the ATLAS Detector using a Trigger-Level Analysis in LHC pp Collisions at $\sqrt{s} = 13$ TeV," 2016.

[10] ATLAS Collaboration, "Search for New Phenomena in Dijet Mass and Angular Distributions from pp Collisions at $\sqrt{s} = 13$ TeV with the ATLAS Detector," *Phys. Lett.*, vol. B754, pp. 302–322, 2016.

[11] K. A. Olive *et al.*, "Review of Particle Physics," *Chin. Phys.*, vol. C38, p. 090001, 2014.

[12] M. E. Peskin and D. V. Schroeder, *An Introduction to Quantum Field Theory.* Advanced book program, Boulder (Colo.): Westview Press Reading (Mass.), 1995. Autre tirage : 1997.

[13] S. Weinberg, "A Model of Leptons," *Phys. Rev. Lett.*, vol. 19, pp. 1264–1266, 1967.

[14] F. Halzen and A. D. Martin, *Quarks abd Leptons: an Introduction Course in Modern Particle Physics.* 1984.

[15] L. Bergstrom, "Dark Matter Evidence, Particle Physics Candidates and Detection Methods," *Annalen Phys.*, vol. 524, pp. 479–496, 2012.

[16] J. Goodman, M. Ibe, A. Rajaraman, W. Shepherd, T. M. P. Tait, and H.-B. Yu, "Constraints on Dark Matter from Colliders," *Phys. Rev.*, vol. D82, p. 116010, 2010.

[17] G. Busoni, A. De Simone, J. Gramling, E. Morgante, and A. Riotto, "On the Validity of the Effective Field Theory for Dark Matter Searches at the LHC, Part II: Complete Analysis for the s-channel," *JCAP*, vol. 1406, p. 060, 2014.

[18] D. Alves, "Simplified Models for LHC New Physics Searches," *J. Phys.*, vol. G39, p. 105005, 2012.

[19] J. Alwall, P. Schuster, and N. Toro, "Simplified Models for a First Characterization of New Physics at the LHC," *Phys. Rev.*, vol. D79, p. 075020, 2009.

[20] G. Busoni, A. De Simone, E. Morgante, and A. Riotto, "On the Validity of the Effective Field Theory for Dark Matter Searches at the LHC," *Phys. Lett.*, vol. B728, pp. 412–421, 2014.

[21] G. Isidori, Y. Nir, and G. Perez, "Flavor Physics Constraints for Physics Beyond the Standard Model," *Ann. Rev. Nucl. Part. Sci.*, vol. 60, p. 355, 2010.

[22] J. Alwall, M. Herquet, F. Maltoni, O. Mattelaer, and T. Stelzer, "Madgraph 5 : Going Beyond," *JHEP*, vol. 06, p. 128, 2011.

[23] ATLAS Collaboration, "Search for New Physics in the Dijet Mass Distribution Using 1 fb^{-1} of pp Collision Data at $\sqrt{s}$ =7 TeV Collected by the Atlas Detector," *Phys. Lett.*, vol. B708, pp. 37–54, 2012.

[24] S. Chatrchyan *et al.*, "Search for Quark Compositeness in Dijet Angular Distributions from pp Collisions at $\sqrt{s} = 7$ TeV," *JHEP*, vol. 05, p. 055, 2012.

[25] ATLAS Collaboration, "Search for New Physics in Dijet Mass and Angular Distributions in pp Collisions at $\sqrt{s} = 7$ TeV Measured with the Atlas Detector," *New J. Phys.*, vol. 13, p. 053044, 2011.

[26] B. A. Dobrescu and F. Yu, "Coupling-Mass Mapping of Dijet Peak Searches," *Phys. Rev.*, vol. D88, no. 3, p. 035021, 2013. [Erratum: Phys. Rev.D90,no.7,079901(2014)].

[27] ATLAS Collaboration, "Search for New Phenomena in Monojet Plus Missing Transverse Momentum Final States Using 10 fb^{-1} of pp Collisions at $\sqrt{S}$ =8 TeV with the Atlas Detector at the LHC," 2012.

[28] A. D. Martin, W. J. Stirling, R. S. Thorne, and G. Watt, "Parton Distributions for the LHC," *Eur. Phys. J.*, vol. C63, pp. 189–285, 2009.

[29] T. Sjostrand, S. Mrenna, and P. Z. Skands, "Pythia 6.4 Physics and Manual," *JHEP*, vol. 05, p. 026, 2006.

[30] M. Selvaggi, "Delphes 3: a Modular Framework for Fast-Simulation of Generic Collider Experiments," *J. Phys. Conf. Ser.*, vol. 523, p. 012033, 2014.

[31] R. Brun, F. Rademakers, and S. Panacek, "Root, an Object Oriented Data Analysis Framework," *Conf. Proc.*, vol. C000917, pp. 11–42, 2000.

[32] A. Hamilton, "The ATLAS Trigger System Commissioning and Performance," in *Hadron collider physics. Proceedings, 22nd Conference, HCP 2010, Toronto, Canada, August 23-27, 2010*, 2010.

[33] P. Czodrowski, "The ATLAS Trigger System: Ready for Run 2," *PoS*, vol. EPS-HEP2015, p. 273, 2015.

[34] E. Simioni, "The Topological Processor for the Future ATLAS Level-1 Trigger: from Design to Commissioning," 2014.

[35] F. Pastore, "The ATLAS Trigger System: Past, Present and Future," *Nucl. Part. Phys. Proc.*, vol. 273-275, pp. 1065–1071, 2016.

[36] M. Asai, "Geant4-a simulation toolkit," *Trans. Amer. Nucl. Soc.*, vol. 95, p. 757, 2006.

[37] R. M. Harris and K. Kousouris, "Searches for Dijet Resonances at Hadron Colliders," *Int. J. Mod. Phys.*, vol. A26, pp. 5005–5055, 2011.

[38] G. Choudalakis, "On Hypothesis Testing, Trials Factor, Hypertests and the BumpHunter," in *Proceedings, PHYSTAT 2011 Workshop on Statistical Issues Related to Discovery Claims in Search Experiments and Unfolding, CERN,Geneva, Switzerland 17-20 January 2011*, 2011.

[39] G. Choudalakis and D. Casadei, "Plotting the Differences Between Data and Expectation," *Eur. Phys.*, vol. D91, 2012.

[40] ATLAS Collaboration, "ATLAS search for new phenomena in dijet mass and angular distributions using pp collisions at $\sqrt{s} = 7$ TeV," *JHEP*, vol. 01, p. 029, 2013.

[41] V. Khachatryan *et al.*, "Search for Dijet Resonances in 7 TeV pp Collisions at CMS," *Phys. Rev. Lett.*, vol. 105, p. 211801, 2010.

[42] ATLAS Collaboration, "Search for quark contact interactions in dijet angular distributions in pp collisions at $\sqrt{s} = 7$ TeV measured with the ATLAS detector," *Phys. Lett.*, vol. B694, pp. 327–345, 2011.

[43] E. Eichten, I. Hinchliffe, K. D. Lane, and C. Quigg, "Supercollider Physics," *Rev. Mod. Phys.*, vol. 56, p. 579, 1984.

[44] E. Eichten, I. Hinchliffe, K. D. Lane, and C. Quigg, "Erratum: Supercollider Physics," *Rev. Mod. Phys.*, vol. 58, p. 1065, 1986.

[45] P. Chiappetta and M. Perrottet, "Possible bounds on compositeness from inclusive one jet production in large hadron colliders," *Phys. Lett.*, vol. B253, p. 489, 1991.

[46] G. P. Salam, "Towards Jetography," *Eur. Phys. J.*, vol. C67, pp. 637–686, 2010.

[47] M. Cacciari, G. P. Salam, and G. Soyez, "The Anti-k(t) Jet Clustering Algorithm," *JHEP*, vol. 04, p. 063, 2008.

[48] ATLAS Collaboration, "ATLAS first level trigger: Technical Design Report," 1998.

[49] W. Lampl, S. Laplace, D. Lelas, P. Loch, H. Ma, S. Menke, S. Rajagopalan, D. Rousseau, S. Snyder, and G. Unal, "Calorimeter Clustering Algorithms: Description and Performance," 2008.

[50] M. Paterno, "Calculating Efficiencies and their Uncertainties," 2004.

[51] V. Lendermann, J. Haller, M. Herbst, K. Kruger, H.-C. Schultz-Coulon, and R. Stamen, "Combining Triggers in HEP Data Analysis," *Nucl. Instrum. Meth.*, vol. A604, pp. 707–718, 2009.

[52] ATLAS Collaboration, "Selection of Jets Produced in 13TeV Proton-Proton Collisions with the ATLAS Detector," Tech. Rep. ATLAS-COM-CONF-2015-024, CERN, Geneva, May 2015.

[53] ATLAS Collaboration, "Jet Energy Measurement with the ATLAS Detector in Proton-Proton Collisions at $\sqrt{s} = 7$ TeV," *Eur. Phys. J.*, vol. C73, no. 3, p. 2304, 2013.

[54] ATLAS Collaboration, "Jet Calibration and Systematic Uncertainties for Jets Reconstructed in the ATLAS Detector at $\sqrt{s} = 13$ TeV," Tech. Rep. ATL-PHYS-PUB-2015-015, CERN, Geneva, Jul 2015.

[55] ATLAS Collaboration, "Pile-up Subtraction and Suppression for Jets in ATLAS," no. ATLAS-CONF-2013-083, 2013.

[56] ATLAS Collaboration, "Pile-up Corrections for Jets from Proton-Proton Collisions at $\sqrt{s} = 7$ TeV in ATLAS in 2011," no. ATLAS-CONF-2012-064, 2012.

[57] ATLAS Collaboration, "Jet Global Sequential Corrections with the ATLAS Detector in Proton-Proton Collisions at $\sqrt{s} = 8$ TeV," Tech. Rep. ATLAS-CONF-2015-002, CERN, Geneva, Mar 2015.

[58] M. Queitsch-maitland, J. Lacey, A. Pilkington, F. Balli, V. Christodoulou, I. A. Cioara, and J. H. Rawling, "In-Situ Determination of the ATLAS Forward Jet Energy Scale and Uncertainty using Dijet Events at $\sqrt{s} = 13$ TeV," Tech. Rep. ATLAS-COM-CONF-2015-023, CERN, Geneva, May 2015.

[59] ATLAS Collaboration, "Data-Driven Determination of the Energy Scale and Resolution of Jets Reconstructed in the ATLAS Calorimeters Using Dijet and Multijet Events at $\sqrt{s} = 8$ TeV," Tech. Rep. ATLAS-CONF-2015-017, CERN, Geneva, Apr 2015.

[60] ATLAS Collaboration, "Jet Energy Scale and its Systematic Uncertainty in Proton-Proton Collisions at $\sqrt{s} = 7$ TeV with ATLAS 2011 Data," no. ATLAS-CONF-2013-004, 2013.

[61] U. Baur, I. HinCHLiffe, and D. Zeppenfeld, "Excited Quark Production at Hadron Colliders," *Int. J. Mod. Phys.*, vol. A2, no. FERMILAB-CONF-87-102-T, p. 1285, 1987.

[62] U. Baur, M. Spira, and P. M. Zerwas, "Excited Quark and Lepton Production at Hadron Colliders," *Phys. Rev.*, vol. D42, pp. 815–824, 1990.

[63] P. H. Frampton and S. L. Glashow, "Chiral Color: an Alternative to the Standard Model," *Phys. Lett.*, vol. B190, p. 157, 1987.

[64] T. Han, I. Lewis, and Z. Liu, "Colored Resonant Signals at the Lhc: Largest Rate and Simplest Topology," *JHEP*, vol. 12, p. 085, 2010.

[65] V. Khachatryan *et al.*, "Search for Quark Contact Interactions and Extra Spatial Dimensions using Dijet Angular Distributions in Proton-Proton Collisions at $\sqrt{s} = 8$ TeV," 2014.

[66] T. Sjostrand, S. Mrenna, and P. Z. Skands, "A Brief Introduction to Pythia 8.1," *Comput. Phys. Commun.*, vol. 178, pp. 852–867, 2008.

[67] "ATLAS Run 1 Pythia8 Tunes," Tech. Rep. ATL-PHYS-PUB-2014-021, CERN, Geneva, Nov 2014.

[68] H.-L. Lai, M. Guzzi, J. Huston, Z. Li, P. M. Nadolsky, J. Pumplin, and C. P. Yuan, "New Parton Distributions for Collider Physics," *Phys. Rev.*, vol. D82, p. 074024, 2010.

[69] Z. Nagy, "Three Jet Cross-Sections in Hadron Hadron Collisions at Next-to-Leading Order," *Phys. Rev. Lett.*, vol. 88, p. 122003, 2002.

[70] S. Catani and M. H. Seymour, "A General Algorithm for Calculating Jet Cross-Sections in NLO QCD," *Nucl. Phys.*, vol. B485, pp. 291–419, 1997. [Erratum: Nucl. Phys.B510,503(1998)].

[71] S. Dittmaier, A. Huss, and C. Speckner, "Weak Radiative Corrections to Dijet Production at Hadron Colliders," *JHEP*, vol. 1211, p. 095, 2012.

[72] S. Alioli, P. Nason, C. Oleari, and E. Re, "A General Framework for Implementing NLO Calculations in Shower Monte Carlo Programs: the Powheg Box," *JHEP*, vol. 06, p. 043, 2010.

[73] S. Alioli, K. Hamilton, P. Nason, C. Oleari, and E. Re, "Jet Pair Production in Powheg," *JHEP*, vol. 04, p. 081, 2011.

[74] J. M. Butterworth, J. R. Forshaw, and M. H. Seymour, "Multiparton Interactions in Photoproduction at HERA," *Z. Phys. C*, vol. 72, pp. 637–646, 1996.

[75] G. Corcella *et al.*, "HERWIG 6.5 release note," 2002.

[76] G. Marchesini *et al.*, "A Monte Carlo Event Generator for Simulating Hadron Emission Reactions with Interfering Gluons," *Comput. Phys. Commun.*, vol. 67, pp. 465–508, 1991.

[77] G. Marchesini *et al.*, "Monte Carlo Simulation of General Hard Processes with Coherent QCD Radiation," *Nucl. Phys.*, vol. B 310, p. 461, 1988.

[78] B. R. Webber, "A QCD Model for Jet Fragmentation Including Soft Gluon Interference," *Nucl. Phys.*, vol. B 238, p. 492, 1984.

[79] N. Boelaert and T. Akesson, *Dijet Angular Distributions in Proton-Proton Collisions at $\sqrt{s} = 7$ TeV and $\sqrt{s} = 14$ TeV*. PhD thesis, Lund U., 2012. Presented on 21 Sep 2010.

[80] ATLAS Collaboration, "Measurement of inclusive jet and dijet cross sections in proton-proton collisions at 7 TeV centre-of-mass energy with the ATLAS detector," *Eur. Phys. J.*, vol. C71, p. 1512, 2011.

[81] ATLAS Collaboration, "Search for New Phenomena in the Dijet Mass Distribution using 5.8 fb^{-1} of pp Collisions at $\sqrt{s} = 8$ TeV collected by the ATLAS Detector," Tech. Rep. ATLAS-CONF-2012-088, CERN, Geneva, Jul 2012.

[82] "Further ATLAS tunes of PYTHIA6 and Pythia 8," Tech. Rep. ATL-PHYS-PUB-2011-014, CERN, Geneva, Nov 2011.

[83] A. Buckley, J. Butterworth, L. Lonnblad, D. Grellscheid, H. Hoeth, J. Monk, H. Schulz, and F. Siegert, "Rivet user manual," *Comput. Phys. Commun.*, vol. 184, pp. 2803–2819, 2013.

[84] Y. Bai, A. Katz, and B. Tweedie, "Pulling Out All the Stops: Searching for RPV SUSY with Stop-Jets," *JHEP*, vol. 01, p. 040, 2014.

[85] M. Lichtnecker, "Determination of alpha_s via the differential 2-jet-rate with atlas at lhc." June 2011.

[86] J. H. Friedman, "Data Analysis Techniques for High Energy Particle Physics," p. 96 p, Oct 1974.

[87] J. Gao, "CIJET: a program for computation of jet cross sections induced by quark contact interactions at hadron colliders,"

[88] T. Carli, D. Clements, A. Cooper-Sarkar, C. Gwenlan, G. P. Salam, *et al.*, "A posteriori inclusion of parton density functions in NLO QCD final-state calculations at hadron colliders: The APPLGRID Project," *Eur.Phys.J.*, vol. C66, pp. 503–524, 2010.

[89] M. Botje, J. Butterworth, A. Cooper-Sarkar, A. de Roeck, J. Feltesse, *et al.*, "The PDF4LHC Working Group Interim Recommendations," 2011.

[90] CMS Collaboration, "Search for Resonances Decaying to Dijet Final States at $\sqrt{s} = 8$ TeV with Scouting Data," 2015.

[91] S. Carrazza, S. Forte, and J. Rojo, "Parton Distributions and Event Generators," in *Proceedings, 43Rd International Symposium on Multiparticle Dynamics (Ismd 13)*, pp. 89–96, 2013.

[92] ATLAS Collaboration, "Characterisation and Mitigation of Beam-Induced Backgrounds Observed in the ATLAS Detector during the 2011 Proton-Proton Run," *JINST*, vol. 8, p. P07004, 2013.

[93] N. Anjos, R. J. Morais Silva Goncalo, G. C. Grossi, D. Miller, A. Pilkington, S. Prince, L. Sawyer, P. Sherwood, A. Ashkenazi, D. Bakshi Gupta, R. Cantrill, V. Christodoulou, A. J. Chuinard, P. Conde Muino, A. Dattagupta, M. Davies, A. Tavares Delgado, J. Gramling, W. J. Fawcett, T. McCarthy, D. Jana, M. Wobisch, E. Varnes, R. Nayyar, D. Freeborn, M. Campanelli, M. Sutton, L. Lopes, R. Piegaia, G. Otero y Garzon, M. R. Devesa, and H. Reisin, "The ATLAS Jet Trigger for Initial LHC Run II," Tech. Rep. ATL-COM-DAQ-2015-164, CERN, Geneva, Sep 2015.

[94] ATLAS Collaboration, "Jet Calibration and Systematic Uncertainties for Jets Reconstructed in the ATLAS Detector at $\sqrt{s} = 13$ TeV." ATL-PHYS-PUB-2015-015, 2015.

[95] ATLAS Collaboration, "Search for New Particles in Two-Jet Final States in 7 TeV pp Collisions with the Atlas Detector at the LHC," *Phys. Rev. Lett.*, vol. 105, p. 161801, 2010.

[96] T. Aaltonen *et al.*, "Search for New Particles Decaying into Dijets in Proton-Antiproton Collisions at $\sqrt{s} = 1.96$ Tev," *Phys. Rev.*, vol. D79, p. 112002, 2009.

[97] J. Alitti *et al.*, "A Measurement of Two Jet Decays of the W and Z Bosons at the CERN $\bar{p}p$ Collider," *Z.Phys.*, vol. C49, pp. 17–28, 1991.

[98] ATLAS Collaboration, "Search for Strong Gravity in Multijet Final States Produced in pp Collisions at $\sqrt{s} = 13$ TeV using the ATLAS Detector at the LHC," 2015.

[99] ATLAS Collaboration, "Search for Resonances Decaying to Photon Pairs in 3.2 fb^{-1} of *pp* Collisions at $\sqrt{s} = 13$ TeV with the ATLAS Detector," Tech. Rep. ATLAS-CONF-2015-081, CERN, Geneva, Dec 2015.

[100] G. Koren, "Search for Dijet Mass Resonance Using Trigger-Level-Analysis in Proton Proton Collision at center of mass energy of 13 TeV with the ATLAS Detector," 2016.

[101] D. Abercrombie *et al.*, "Dark Matter Benchmark Models for Early LHC Run-2 Searches: Report of the ATLAS/CMS Dark Matter Forum," 2015.

[102] M. Chala, F. Kahlhoefer, M. McCullough, G. Nardini, and K. Schmidt-Hoberg, "Constraining Dark Sectors with Monojets and Dijets," *JHEP*, vol. 07, p. 089, 2015.

[103] G. Mikenberg, "Thin Gap Gas Chambers for Hadronic Calorimetry," *Nucl. Instrum. Meth.*, vol. A265, pp. 223–227, 1988.

[104] S. Majewski, G. Charpak, A. Breskin, and G. Mikenberg, "A Thin Multiwire Chamber Operating in the High Multiplication Mode," *Nucl. Instrum. Meth.*, vol. 217, pp. 265–271, 1983.

[105] N. Amram *et al.*, "Position Resolution and Efficiency Measurements with Large Scale Thin Gap Chambers for the Super LHC," *Nucl. Instrum. Meth.*, vol. A628, pp. 177–181, 2011.

[106] E. Etzion *et al.*, "The Cosmic Ray Hodoscopes for Testing Thin Gap Chambers at the Technion and Tel Aviv University," *IEEE Trans. Nucl. Sci.*, vol. 51, pp. 2091–2096, 2004.

תקציר

חיבור זה מציג חיפוש אחר פיסיקה חדשה בהתנגשויות בין פרוטונים במאיץ ההדרונים הגדול ה-LHC באמצעות מאורעות בהם נצפים לפחות שני סילונים בעלי תנע רוחבי גדול בגלאי ATLAS. במאורעות אלו נמדדו המסה האינווריאנטית וההתפלגות הזויתית של שני הסילונים בעלי התנע הרוחבי הגדול ביותר.

כל התוצאות קונסיסטנטיות עם תחזיות המודל הסטנדרטי. החיפוש באמצעות ההתפלגות הזויתית התבצע במאורעות בהן אנרגית מרכז המסה היתה 8 TeV והארה של 17.3 1/fb, ותוצאותיו גררו הצבת גבולות חדשים עבור מודל אפקטיבי של אינטראקציה בין ארבעה פרמיונים. מודל כזה נשלל עבור compositensess scale של 8.1 TeV בהתאבכות הורסת ו- 12 TeV בהתאבכות בונה במידת ודאות של 95%. החיפוש אחר רזוננס בהתפלגות המסה האינווריאנטית בוצע לראשונה בתולדות הגלאי ATLAS תוך שימוש באנליזת סילונים שנלקחו ברמת ה-trigger באנרגית מרכז מסה של 13 TeV והארה של 3.4 1/fb. גבולות תחתונים הוצבו עבור סיגנאלים כלליים בצורת גאוסיינים במגוון מסות ורוחבים, ובמודל מופשט של בוזון אקסיאל וקטורי שאינו מבצע אינטראקציה עם לפטונים ומהווה מקשר בין חלקיקי המודל הסטנדרטי המוכרים לבין הסקטור האפל, נקבעו גבולות תחתונים למסה ולקבוע הצימוד של בוזון זה עם המודל הסטנדרטי.

בנוסף, חיבור זה מסכם מאמץ משותף של נסיונאים ותיאורטיקנים לעודד שימוש במודלים מופשטים של חומר אפל בחיפוש אחר פיסיקה חדשה, וביצוע של בדיקת איכות לגלאים מסוג TGC לקראת השמשתם בניסוי ATLAS.

TEL AVIV UNIVERSITY
אוניברסיטת תל-אביב
RAYMOND AND BEVERLY SACKLER
FACULTY OF EXACT SCIENCES
SCHOOL OF PHYSICS & ASTRONOMY
הפקולטה למדעים מדוייקים
ע"ש ריימונד ובברלי סאקלר
בית הספר לפיסיקה ואסטרונומיה

חיבור לשם קבלת התואר "דוקטור לפילוסופיה"

חיפוש אחר פיסיקה חדשה מעבר למודל הסטנדרטי במאורעות עם שני סילונים במאיץ ההדרונים הגדול

מוגש לסנאט של אוניברסיטת תל אביב על ידי
עדי אשכנזי

המחקר נערך בהנחייתם של
דר' **גדעון בלע** ופרופ' **ארז עציון**

אפריל 2017
adi.ashkenazi@cern.ch